TISSUE-LEVEL MECHANISMS DRIVING CARDIAC PROGENITOR AND EXTRACELLULAR MATRIX MOVEMENTS DURING EARLY VERTEBRATE HEART DEVELOPMENT

BY

Anastasiia Aleksandrova

B.S., Biology, National Taras Shevchenko University of Kiev, Kiev, Ukraine, 2006

Submitted to the graduate degree program in Anatomy and Cell Biology and the Graduate Faculty of the University of Kansas in partial fulfillment of the requirements for the degree of Doctor of Philosophy.

Graduate committee:

_____
Brenda J. Rongish, Ph.D., Chair

_____
Andras Czirok, Ph.D.

_____
Joseph D. Fontes, Ph.D.

_____
Matthew C. Gibson, Ph.D.

_____
Paul M. Kulesa, Ph.D.

_____
Douglas E. Wright, Ph.D.

Date defended: November 27th, 2012

The Dissertation Committee for Anastasiia Aleksandrova
certifies that this is the approved version of the following dissertation:

TISSUE-LEVEL MECHANISMS
DRIVING CARDIAC PROGENITOR AND EXTRACELLULAR MATRIX MOVEMENTS
DURING EARLY VERTEBRATE HEART DEVELOPMENT

_____
Brenda J. Rongish, Ph.D., Chair

Date Approved: December 12th, 2012

ABSTRACT

Early vertebrate cardiogenesis involves the movement of heart progenitor cells from their initial lateral positions to the embryonic midline, where they assemble into a primitive (tubular) heart. The early heart consists of the myocardium on the outside, a medial extracellular matrix layer (cardiac jelly), and the endocardium comprising the inner surface of the tube. Cardiac morphogenesis in avians and mammals is inseparable from the development of the foregut, an embryonic predecessor of the upper gastrointestinal system, liver, and pancreas. The foregut provides molecular cues to regulate endocardial and myocardial differentiation from mesodermal progenitors. Also, concomitantly with the initiation of midline-directed cardiac progenitor movements, foregut endoderm undergoes dramatic folding and elongation. Upon initial assembly the heart and foregut remain connected through a mesentery until later stages. Research yielded many insights as to molecular factors involved in guiding cardiac progenitors to the midline, yet cellular and tissue mechanisms coordinating these movements remain poorly understood.

This work investigates motion of all three early heart constituents – the endocardial and myocardial progenitors, and surrounding ECM - in live quail embryos using a combination of time-lapse microscopy, chemical and mechanical perturbations, computational analysis and modeling. By visualizing the tissue environment for cell displacements, we distinguish the active (tissue-independent) movements from those cells undergo in a manner coordinated with the surrounding tissues. In the first part, we analyzed the movements of fluorescently-labeled ECM (fibronectin, fibrillin-2) and those

of endocardial progenitors. We found that the bulk of observed midline-directed movement of pre-endocardial cells occurs in a coordinated fashion with their surrounding ECM. Further, that ECM from extracardiac sources is transferred to and incorporated into the growing heart. By assessing the contributions of active cell motility to the observed endocardial displacements we found its role to be secondary to that of convective tissue movement within the anterior embryo, for the arrival of endocardial progenitors at the midline.

Second, we assessed the myocardial progenitor movements relative to the fibronectin ECM and the endoderm. We found that an observed antero-medial direction of myocardial displacements towards the midline is driven by a combination of: 1) medial movement, coordinated with surrounding tissue, and 2) anterior-directed movement, accomplished via a coordinated deformation of myocardial progenitors, organized into a continuous epithelial sheet.

Finally, we investigated the effects of VEGF overexposure on progenitor movements during early cardiogenesis. We found that a dramatic VEGF-induced increase in the size of the cardiac inflow region can affect coordinated movements/deformations displayed by myocardial progenitors, and result in defects in heart tube elongation.

ACKNOWLEDGEMENTS

I am very deeply thankful to a number of amazing people that helped, guided, inspired and judged the progress of my graduate studies. To all of you – I am truly blessed to have you in my life, as our interactions helped me grow to become a better professional and a different person.

First of all, I take my hat off to my mentor, Dr. Brenda Rongish. You are a shining example of impeccable professionalism combined with genuine care for those around you. You provided me with freedom I could only dream of to explore the realm of experimental embryology while designing and conducting experiments in your laboratory, yet always were there when support and/or advice was needed oh so urgently. I hope to have learnt at least something from what you were trying to teach me, and surely appreciate all of the lessons.

Second, I would like to thank Dr. Andras Czirok, but I am at a loss for words to convey the full depth of my gratitude. Your incredible scientific talent contributed tremendously to the development of my project. Through your expert guidance, I developed a feel and a deep interest for fields of cell motility and biophysical mechanisms of morphogenesis, which were completely new to me. Also, you have that proverbial “glass-half-full” attitude towards experimental results that always helped me maintain excitement and motivation through the dark times of failure. Thank you for all of the encouragement, enlightening conversations and awesome bar charts!

I am very grateful to Dr. Charlie Little for inspiring discussions of various aspects of my research and science in general. Thank you for providing your unique perspective

as someone who has been a leader in the field and a wet bench experimental embryologist for a number of successful and prolific years of your science career. Things I learnt from you were seminal for my progress, and I hope to use them throughout my research endeavors. Also, I hope to some day develop some of your courage to challenge textbook dogmas!

A very heartfelt thank you is addressed to Dr. Joseph Fontes. Time spent as a technician in your laboratory prepared me for the demands of graduate school like no other experience could. Thank you for investing the time and effort in teaching your students (and technicians) to think critically and read voraciously. I am deeply grateful to you for supporting me in the decision to pursue my passion for developmental biology during graduate studies, even though it meant leaving your laboratory (perhaps that was the plan all along!). I will always look up to you as among the most important mentor figures in my life and career.

I would like to gratefully acknowledge the contributions of the remaining members of my graduate dissertation committee, Drs. Matthew Gibson, Paul Kulesa and Douglas Wright, and Dr. Juan Bruses, who served on my comprehensive examination committee. Thank you for your comments and suggestions that always motivated me, and allowed viewing my project from a different perspective. I valued each of your inputs, and incorporating them into my project benefitted it immensely.

Very importantly, I owe many thanks to members of the Little-Rongish laboratory, Michael Filla**,** Tracey Cheuvront and Alan Petersen, and Edina Kosa and Dr. Paul Rupp of Dr. Czirok's laboratory. You are, all of you, some of the most intelligent, dedicated,

generous, and caring people I've ever met. Thank you for teaching me so patiently when I joined the lab with no prior embryology experience, and for always being ready to help in case of any of the frequently-occurring late-night/weekend equipment or computer emergencies. With your tireless efforts and kind, caring personalities you create such a unique environment in the laboratory that it would feel wrong not to be productive.

Also, I would like to thank Barbara Fegley, Patricia St John, Rosetta Barkley and Karen Grantham, who contributed to my project with their enormous expertise in the fields of histology, electron and confocal microscopy. I would also like to thank Phil Shafer for his help in poster and illustration design. Each one of you is a true wizard of your field of expertise, and learning from you as well as watching you work was a very enriching experience for me. Thank you!

I would like to recognize members of the Anatomy and Cell Biology office staff – Helen Allensworth, Katie Bishop, Kelly-Ann Buszek, Sharon Olson, and Steven Wiggins, and thank them for the much needed administrative help and support they kindly provided to me throughout my time in the department.

From the very depth of my being I am eternally grateful to my family – my Mom, Dr. Ekateryna Aleksandrova, my Grandfather, Vyacheslav Kochergin, and to my late Grandmother, Raisa Kochergina. From the earliest years of childhood you challenged me to learn, be curious about the world around, and to always observe. I am proud that in our family not being curious and willing to learn something (sometimes completely random) was always perceived as a vice. Thank you for all of your unconditional (and

sometimes undeserved) love and for the support you lend to my every decision. I love you and hope to be someone you can be proud of.

On a concluding note, I owe a lifetime of gratitude to one incredible gentleman – my best friend, my most avid supporter and harshest critic, my wonderful husband, Dr. Oleksandr Galkin. Listing all the things I am indebted to you for would take volumes. What you did for me during the trying times of graduate school have magnified that enormous respect I have for you, both professionally and personally. Thank you for always believing in my potential, and encouraging me to carry on. You are amazing and I love you!

TABLE OF CONTENTS

LIST OF FIGURES

CHAPTER ONE:

Introduction

An overview of events of early heart formation in avian embryos

Heart morphogenesis in all vertebrates, including fish, avians, and humans involves a similar sequence of events (reviewed in Fishman and Chien, 1997). After gastrulation endocardial and myocardial progenitor cells are located in bilateral “heart fields” on either side of the midline. An assembly of the organ begins as endocardial and myocardial cells from heart fields fuse at the ventral midline. The resultant tubular heart consists of three layers: myocardium on the outside of the organ, acellular ECM layer of cardiac jelly in the middle, and endocardium on the inside of the tube. The onset of contractile function of the myocardium follows the fusion event shortly. The tubular heart maintains a close association with the foregut endoderm via a mesentery called the dorsal mesocardium (Fig. 1.1). At later stages, the dorsal mesocardium gets degraded, and the cardiac tube undergoes looping to the right side. After this initial looping event the heart tube folds several more times during chamber specification. At this stage the differences between 2-, 3-, and 4-chambered hearts of different groups of vertebrates become very evident. Concluding steps of cardiac morphogenesis include the establishment of coronary circulation, development of the conductive system and innervation etc. Close resemblance of early heart development in avians and mammals was taken into consideration by many generations of researchers that used chick and quail embryos as models for studies of heart and vascular development. Their work provided insight into the intricate details of early heart development in avians.

During gastrulation in birds epiblast cells ingress through the primitive streak and give rise to all three germ layers of the embryo. Cardiac progenitor cells were shown to

be one of the first cell populations to undergo ingression (Garcia-Martinez and Schoenwolf, 1993), which in turn is followed by their rapid anterior and lateral movement. Then cardiac progenitor cells assume their residency within a specific area of the lateral plate mesoderm, referred to as the “heart field”.

The definition of the margins of the heart field and development of the position-fate maps for cardiac progenitor cells has been a goal of several generations of investigators, beginning with Rawles (1943). They used a wide array of techniques ranging from physical labeling of the cells and observing their position at advancing developmental stages (Stalsberg and DeHaan, 1969; Rosenquist, 1970; Hochgreb et al., 2003; Abu-Issa and Kirby, 2008) to localization of molecular markers associated with myocardial differentiation, such as the transcription factor Nkx2.5 and the TGFβ family member Bmp-2 (Schultheiss et al., 1995; Yutzey and Kirby, 1999). Results from the most recent position-fate mapping studies (Abu-Issa and Kirby, 2008) place the anterior border of the heart field near the forming buccopharyngeal membrane at early somitic stages in avian embryo. Posteriorly the area extends to the level of the 3rd-4th somite, and mediolaterally it lies between the paraxial mesoderm and the border of the area pellucida (Fig. 1.2). Surprisingly, when position fates determined by cell labeling were compared with molecular marker expression profiles, the two areas did not fully overlap until later stages (HH6 for Bmp-2 and HH10 for Nkx2.5) (Redkar et al., 2001). Although these fate mapping studies have contributed significantly to the field, certain technical limitations complicated the interpretation of the results. For example, in the experiments of DeHaan, Rosenquist and Stalsberg with grafting of radioactively labeled

fragments of an embryo, mesodermal cells could not be labeled exclusively. Multiple investigators (Ehrman and Yutzey, 1999; Redkar et al., 2001; Abu-Issa and Kirby, 2008) utilized targeted injection of lipophilic dyes to label mesoderm. However, this strategy did not exclude the possibility of labeling the endoderm along with mesoderm at the site of injection. Endodermal derivatives, in turn, could potentially have obscured the resultant fate maps.

Some of these concerns were addressed in a recent study by Cui et al. (2009), where a subset of ingressing epiblastic cells was electroporated with a plasmid encoding a fluorescent marker. A portion of labeled cells then contributed to the precardiac mesoderm, and subsequently to the myocardial layer of the heart proper. Movements and fate of this cell population were followed by time lapse imaging and cell tracking analysis. This study revealed many previously undescribed aspects of the origin and morphogenetic movements of the myocardial progenitor cell population. These cells were shown to reside in a precardiac field that is contiguous and circular in shape. The much debated question of cranial-caudal patterning of the heart tube has also been addressed. In addition, the role of global tissue movements ("rolling-up") of the endoderm in determination of positional fate of myocardial progenitors has been demonstrated. The outcomes of the study by Cui et al. illustrate that dynamic, time lapse imaging-based fate maps of precardiac mesoderm need to be developed as they will help integrate multiple (and often conflicting) results obtained by many research groups over the course of more than 60 years.

Figure 1.1: Morphogenetic events during early heart development (illustration from Mikawa, 1999).

Top panel – precardiac mesoderm cells (red) ingress through the primitive streak at HH 4. Second panel – endocardial precursors (green) segregate from the layer of presumptive myocardium (red) at HH 7-8. Bottom panel – the tubular heart is formed as a result of the fusion of bilateral cardiac primordia *(illustration from Mikawa T. (1999). Cardiac Lineages. In: Harvey RP, Rosenthal N, editors. Heart development. New York: Academic Press. p 20).*

Figure 1.1

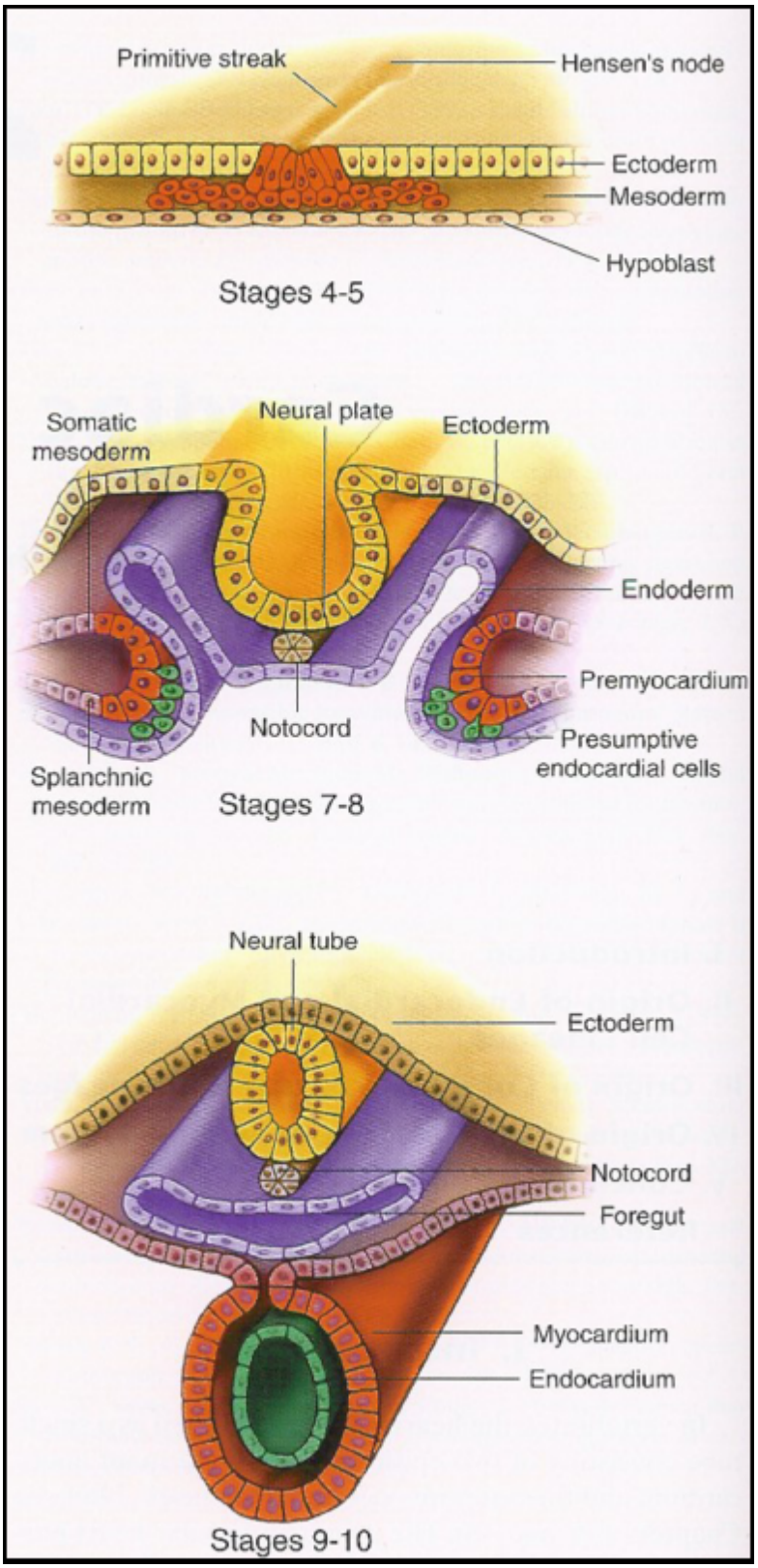
Primitive streak
Hensen's node
Ectoderm
Mesoderm
Hypoblast
Stages 4-5
Somatic mesoderm
Neural plate
Ectoderm
Endoderm
Premyocardium
Notocord
Presumptive endocardial cells
Splanchnic mesoderm
Stages 7-8
Neural tube
Ectoderm
Notocord
Foregut
Myocardium
Endocardium
Stages 9-10

Figure 1.2: Location of cardiogenic fields in the avian embryo at HH5 according to different investigators (A) and a schematic representation of Nkx 2.5 and Bmp-2 expression patterns at the same stage of development (illustration from *Kirby ML. (2007). Cardiac Development. Oxford University Press, Oxford, UK, p. 24*).

Figure 1.2


Rawles, 1943;
Redkar et al, 2001
Rosenquist & DeHaan, 1966
Stalsberg & DeHann, 1969
Ehrman & Yutzey, 1999
Colas et al, 2000
A
B
Nkx2.5
BMP

Origin and specification of endocardial and myocardial cell lineages

Endocardial cells represent a specialized subset of endothelium. They form the interior surface of the heart that is contiguous with the endothelial lining of the inflow and outflow regions. Myocardial cells form the contractile tissue of the heart. Endocardiocytes are important for multiple aspects of cardiac development and function, such as heart valve formation (Armstrong, Bischoff, 2004). They functionally interact with myocardium, participating in regulation of proliferation and contractility of adult myocardium (Brutsaert, Andries, 1992), maintenance of a smooth surface for laminar blood flow and others. In addition, recent work by Holtzman et al. (2007) demonstrated the importance of the endocardium for cardiomyocyte migration and establishment of proper interactions between the layers of the developing heart in zebrafish embryos. Stalsberg and DeHaan (1969) had shown that endocardial cells originate from the same regions of the embryo as cardiomyocyte progenitors. Since this discovery it has been debated whether a common precursor exists for the myocardial and endocardial lineages of the heart.

To address this issue several approaches have been taken. By retroviral cell labeling (Cohen-Gould and Mikawa, 1996; Wei and Mikawa, 2000) it was demonstrated that descendants of progenitor cells labeled at the primitive streak at HH3 or within precardiac mesoderm at HH4 became either exclusively myocardial or endocardial, but the mix of the two was never observed in a clonal population. Another group (Eisenberg and Baden, 1995) created a cell line (QCE-6) derived from anterior mesoderm of the quail embryo at HH4. QCE-6 cells proved capable of expressing either myocardial or

endocardial cell markers in response to different cell culture conditions. Unfortunately, at present there are no reliable lineage-specific markers that would allow distinguishing between myo- and endocardial lineages at gastrulation and early postgastrulation stages. However, the results of in vivo cell lineage tracing strongly suggest that endocardial cells and cardiomyocytes arise from distinct progenitor populations.

It was also shown that commitment of endocardial cells is independent from gastrulation, and possibly occurs before this step of development (Christ et al., 1991). Von Kirschhofer et al. (1994) utilized cytochalasin B to block gastrulation movements in quail embryos. By elegant quail-chick grafting experiments, they demonstrated that unlike the endocardium, myogenic cells did not undergo commitment without having gastrulated.

Although apparently the determination of endocardial progenitors occurs prior to gastrulation, their differentiation depends on inducing signals from the endoderm (Sugi, Markwald, 1996). Among those signals TGFβ ligands TGFβ2, -3, and -4 were shown to induce endocardial differentiation in mesodermal explants in vitro (Sugi and Markwald, 2003). Differentiating endocardial cells in vivo acquire the characteristics of mesenchymal cells and sort from the splanchnic layer of mesoderm in small groups (Sugi and Markwald, 1996). At the same time myocardial progenitors remain organized in large clusters with epithelial properties. Differential expression of N-cadherin has been implicated in cell sorting of the myo- and endocardial progenitor populations (Linask and Lash, 1993). Commitment to the myocardial fate, and further myocardial differentiation most likely requires integration of Bmp, Fgf, Nodal, and Hedgehog signals

(reviewed in Evans et al., 2010).

FGF-2 and VEGF signaling from the endoderm regulate differentiation of endocardial cells (reviewed in Lough and Sugi, 2000). Like vascular endothelial cells, differentiated endocardial cells express a number of genes, examples of which include receptors for VEGF (Flt-1, Flk-1) and angiopoietins 1-4 (Tie1, Tie2), cell adhesion molecule vascular endothelial (VE) cadherin, connexin 37, endothelial-specific transcription factor Epas1 and others (reviewed in Kirby, 2007). Both endocardial and endothelial cells in quail embryos possess the recognition site for QH1 antibody (Pardanaud et al., 1987). Although the identity of the QH1 epitope was not identified, this antibody has been an invaluable asset in vascular developmental biology. Reliable markers of such quality for distinguishing between vascular endothelial and endocardial cells are not available at present.

Nevertheless, multiple lines of evidence suggest that these two populations are biochemically distinct. Zebrafish mutants cloche and faust lack endocardial cells, but retain the blood vessel endothelium (Stainier et al., 1995; Reiter et al., 1999). In mice, it was shown that angiopoietin signaling through receptor kinase Tie2 is critical for endocardial, but not endothelial development (Puri et al., 1999). Expression of transcription factors GATA5 (disrupted in faust mutants) and NFATc are restricted to the endocardium, and are turned on sequentially during endocardial differentiation of mesodermal cells in vitro (Nemer and Nemer, 2002). It remains unknown what drives the movement of the endocardial cells towards the midline during fusion. As to the myocardial cells, it was shown that in zebrafish embryos fibronectin is important for

maintenance of epithelial organization by myocardial progenitors during their midline-directed motion (Trihn and Stainier, 2004). Early work by Linask and Lash (1986) described an increasing amount of fibronectin fibrils at the mesoderm-endoderm interface as a mechanism that triggers the haptotaxis of precardiac cells towards the midline. However, other groups did not confirm an existence of such a concentration gradient in similar studies. In zebrafish, the sphingosine-1-phosphate receptor is implicated in the migration of heart primordia (Kupperman et al., 2000). Of note, most of the above mentioned studies were concerned with the movement of the myocardial progenitor cells, the organization and behavior of which during early cardiogenic stages was shown (Sabin, 1920) to differ from that of the endocardial cell population.

Composition and functional significance of extracellular matrix (cardiac jelly) in the developing heart

Cardiac jelly is an extensive layer of extracellular matrix that separates endocardial and myocardial layers of the developing heart (Davies, 1924). Morphologically CJ consists of two unequally sized apposing basement membranes. The larger BM is adjacent to the myocardium and comprises the bulk of the cardiac jelly. BM associated with endocardium is much thinner and consists only of lamina densa (Kitten et al., 1987). Although the assembly of cardiac jelly begins at HH8, it performs its main functions later in development, namely during the looping process, that begins at HH10 (Nakamura and Manasek, 1978; Nakamura and Manasek, 1981; Manner, 2000), and cardiac cushion formation (HH16-17; Martinsen, 2005).

Extracellular matrix of the developing heart and CJ layer includes a variety of components, such as glycosaminoglycans (hyaluronic acid, chondroitin sulfate), collagens (types I, III, IV, XVIII), glycoproteins (fibronectin, laminin, vitronectin, cytotactin, fibrillins -1 and -2, thrombospondin), and proteoglycans (Little et al., 1989; Gallagher et al., 1993; Spence et al., 1992; reviewed in Little and Rongish, 1995). Most of the literature sources attribute the formation of the cardiac jelly to the synthetic activity of myocardial cells that are believed to produce the bulk of the CJ components shortly before and immediately after they assume their final positions in the tubular heart (Manasek, 1977; Eisenberg and Markwald, 1995; Kirby, 2007). However, the process of CJ assembly and the origins of its individual components have not been fully resolved. In Chapter 2 of this dissertation we demonstrate, that a fraction of CJ constituents is

transferred from extracardiac locations in association with individual cells and cell aggregates that undergo displacements during tubular heart formation.

In our work we focused on the CJ constituents that are known to play important roles in multiple steps of heart development in several species. For instance, fibronectin is found in the precardiac mesoderm as early as HH5 in chicken embryos, and its abundance is increased during the period of cell migration (Icardo and Manasek, 1983; Linask and Lash, 1986). In zebrafish fibronectin allows cardiomyocytes to preserve their epithelial organization during migration, the condition necessary for successful cardiac tube fusion (Trihn and Stainier, 2004). The phenotype analysis of fibronectin null mice provides the evidence for the important role of fibronectin in mesodermal migration, proliferation and differentiation (George et al., 1993).

Fibrillins-1 and -2 are integral components of extracellular microfibrils found in elastic and nonelastic tissues (reviewed in Hubmacher et al., 2006). During early heart development cell repositioning occurs in the environment abundant in such microfibrils that reach a diameter of 10-12 nm (Sakai et al., 1986). At more advanced stages of cardiogenesis, fibrillins associate with the endocardium and cardiac jelly (Hurle et al., 1994; Wunsch et al., 1994). Fibrillins play a regulatory role in the elastic fiber assembly and possess physical properties that allow them to provide dynamic connective tissues (such as CJ or ECM of the precardiac mesoderm) with long-range elasticity (Kielty et al., 2002). In addition to their mechanical role, fibrillins are involved in the extracellular control of TGFβ and BMP signaling (reviewed in Charbonneau et. al, 2004).

Other constituents of the cardiac ECM are also capable of modulating growth

factor signaling by sequestration of secreted morphogens and thus limiting their bioavailability. For instance, defined oligosaccharide sequences within heparan sulfate proteoglycan were shown to specifically inhibit FGF-2 signaling (Ashikari-Hada et al., 2009), and perlecan was demonstrated to modulate the VEGF-VEGFR2 signaling axis (Zoeller et al., 2009).

Mechanisms that regulate and guide cardiac progenitor movements during early heart formation

A lot of evidence on important regulators of cardiac cell movements came from studies in zebrafish. A wide array of mutations causes defects in midline-directed migration, causing formation of two separated “half-hearts”, a condition known as cardia bifida. Out of these mutations, some affect morphogenesis of the endoderm in the vicinity of the developing heart, for instance *casanova*, *bonnie and clyde*, *faust*, *miles apart* (Alexander et al., 1999; Kikuchi et al., 2001; Kupperman et al., 2000; Reiter et al., 1999). Another category of mutations (*natter*, *hands off*) causes disruption in the organization of the fibronectin ECM that surrounds the cardiomyocytes (e.g., (Garavito-Aguilar et al., 2010; Trinh and Stainier, 2004). Results of the above studies in zebrafish highlight the importance of myocardium–endoderm and myocardium–ECM interactions during heart tube formation.

In avians, Wnt3a was shown to regulate cardiac progenitor motion via a chemorepulsion mechanism, dependent on RhoA function (Yue et al., 2008). In mice, GATA4 knockout causes cardia bifida (Molkentin et al., 1997), which can be rescued by transplantation of GATA4-positive endoderm (Narita et al., 1997). Mutations in transcription factors HIF1alpha and Foxp4 also lead to cardia bifida (Compernolle et al., 2003; Li et al., 2004).

Most of the above studies are concerned predominantly with the myocardial progenitor cell movements. Recently, however, a study by Fish et al. (2011) shed some light on molecular mechanisms driving endocardial progenitor movements towards the

midline in zebrafish embryos, demonstrating that Slit/miR-218/Robo/VEGF signaling axis is involved in the control of endocardial migration.

For avian and mammalian models evidence regarding specific signaling and cellular mechanisms involved in motion of endocardial progenitors is very scarce. At the same time, vascular endothelial precursor cell migration has been studied extensively in various systems (reviewed in Lamalice et al., 2007, Schmidt et al., 2007). Directed motility of endothelial precursors can be regulated by a concentration gradient of soluble ligands (chemotaxis), insoluble ligands immobilized in surrounding tissue (haptotaxis), or mechanical forces (mechanotaxis). VEGF, bFGF, and angiopoietins are recognized as the main positive regulators of endothelial chemotaxis (Kazemi et al, 2002, Hiratsuka et al, 2005), and semaphorin 3A1 has a repulsive effect on vascular migration (reviewed in Schmidt et al., 2007).

At the cellular level endothelial migration is based on remodeling of the actin cytoskeleton with the formation of filopodia, lamellopodia and stress fibers (reviewed in Shuster and Herman, 1998). Myosin IIA and B interact with the actin cytoskeleton and participate in protrusive activity and force generation in migrating endothelial cells (Kolega, 2006). RhoA was shown to be important in vascular progenitor and mature endothelial cell migration through participation in VEGF receptor-2 and phosphatidyl-inositol 3-kinase activation (Gingras et al, 2000, Qi et al., 2001). Interestingly, RhoA is highly expressed in the anterior lateral plate, developing heart, and anterior intestinal portal at HH 6-9 in avian embryos. SiRNA-mediated downregulation of RhoA at these stages results in failure of cardiac progenitor field fusion, or cardia bifida (Kaarbo et al,

2003). However, it is still unknown whether endocardial and vascular endothelial cells share a common progenitor in avian embryos. Results of Bussmann et al. in zebrafish (2007) suggest that endocardial cells are derived from the hematopoietic and vascular lineage, and then migrate to the site of cardiogenesis. In contrast, Misfeldt and colleagues (2009) state in their recent publication that in mice the endocardium shares a common multipotent mesodermal progenitor with the myocardium, and is independent from other vascular lineages. Therefore, it is unclear if all of the above information on vascular progenitor migration is applicable to the migration of pre-endocardial cells in early avian development.

Additional information relevant to endocardial cell migration comes from studies of cardiac cushion (primordial valve) formation. At HH14 the cardiac jelly at the atrio-ventricular junction expands and by HH17 becomes the site of invasion of a specific JB3+ subset (Wunsch et al, 1994) of endocardial cells. These endocardial cells are induced to undergo epithelial-to-mesenchymal transformation (EMT) by a multicomponent signaling from the myocardium (reviewed in Eisenberg and Markwald, 1995, Kirby, 2007). Cushion explant studies by Zhao and Rivkees (2004) and Sakabe et al. (2006) elucidated a prominent role for Rho-dependent kinases ROCK-1 and -2, and myosin light chain kinase in the regulation of the endocardial cell motility.

VEGF signaling in development

Vascular endothelial growth factor A (VEGF A), a member of VEGF subfamily of growth factors, is an endothelial-specific mitogen that plays key roles in the processes of angiogenesis and vasculogenesis. VEGF-A is a principal regulator of the development of the embryonic vasculature and heart, and plays important roles in organogenesis of liver, kidney, lung, muscle and bone tissue, skin and nervous system (reviewed in Haigh, 2008). Secreted VEGF-A binds to VEGF receptors, which are highly expressed by the cells of the endothelial lineage, and stimulates endothelial proliferation, migration and survival, leading to the outgrowth of new blood vessels (reviewed in Ferrara, 2001).

VEGF-A is a glycoprotein that forms homodimers of 34 – 46 kDa in size. In human, six different mRNA isoforms are produced from a single VEGF gene, containing 8 exons, by means of alternative splicing (Tischer et al, 1991). VEGF isoforms differ in their ability to be secreted or cell- or ECM-bound, depending on the presence in of heparan sulfate proteoglycan (HSPG)-binding motives and cell surface consensus retention sequence (CRS). Predominant VEGF isoforms are VEGF121, VEGF165 and VEGF189; they are produced in most cells that express VEGF. Less abundant VEGF145 and VEGF 206 are mostly expressed in placental cells, whereas VEGF183 is expressed more ubiquitously (Haigh, 2008). Major VEGF isoforms expressed by mouse (VEGF120, 164, 188; reviewed in Ferrara, 2001) and quail (VEGF 122, 146, 166, and 190; Finkelstein and Poole, 2003) slightly differ in size from human counterparts, but have similar functions.

Properties of VEGF isoforms are different. VEGF121 does not contain an HSPG-binding domain and is freely diffusible in the extracellular space. VEGF165, VEGF189 and VEGF206 all interact with HSPG and mostly associate with cell surface and ECM. Cell- and ECM-bound VEGF could be released as soluble forms by heparinase or via plasmin-dependent cleavage of longer isoforms (Houck et al, 1992).

VEGF-A expression is positively regulated by a number of morphogenetic factors, e.g. Fgf2 and 7, PDGF, EGF (Pages and Pouyssegur, 2005). VEGF expression is strongly upregulated in cells by hypoxic conditions. Promoter of the VEGF gene contains a hypoxia responsive element (HRE) carrying a binding site for hypoxia-inducible factor 1 (HIF1) that binds and activates the promoter (Forsythe et al, 1996). VEGF pre-mRNA contains an internal ribosome entry site that is being activated under the severe hypoxia and allows VEGF production when cap-dependent translation is impaired (Dibbens et al, 1999). Also, VEGF mRNA half-life is regulated by hypoxia-induced factor HuR, which binds to untranslated regions of the mRNA molecules and stabilizes them. VEGF promoter is additionally positively regulated by a number of transcriptional factors such as AP-1, AP-2 and Sp1 (Tischer et al, 1991), and some other (reviewed in Xie et al., 2004; Pages and Pouyssegur, 2005).

VEGF-A ligand binds to tyrosine kinase receptors VEGFR-1 (FLT1) and VEGFR-2 (FLK1, KDR), with neuropilins 1 and 2 acting as co-receptors (NRP1 and 2; Gluzman-Poltorak et al., 2001). Both VEGF-R1 and –R2 are critically important in embryonic development, as deficiency in any of the two receptors leads to prenatal lethality (Ferrara, 2001).

VEGFR-1 (FLT1) has higher affinity for VEGF ligand (in particular for the VEGF165 isoform) compared to VEGF-R2 (de Vries et al., 1992; Terman et al., 1992). Since the deletion of kinase domain of FLT1 in mice did not adversely affect cardiovascular development, it was suggested that the main function of VEGFR-1 was to inhibit VEGF activity by concurrent binding of VEGF-A molecules and sequestering them in non-signaling inactive complexes ("decoy receptor"; Hiratsuka et al., 2005). Additionally, FLT1 was shown to be important in recruiting VEGF molecules to the membranes of FLT1/FLK1-coexpressing cells (reviewed in Haigh, 2008).

VEGFR-2, or KDR undergoes strong tyrosine phosphorylation after VEGF ligand binding. VEGF signaling through KDR is responsible for the majority of VEGF-A-induced effects on endothelial cells, such as stimulation of proliferation, migration, survival, and permeability (reviewed in Ferrara, 2001; Rohrberg, 2003). Neuropilins are involved in modulating VEGF-R2 signaling as co-receptors (Gluzman-Poltorak et al., 2001; Takashima et al., 2002).

Results of multiple gain- and loss-of-function studies in rodent and avian models (Miquerol et al., 2000; Dor et al., 2001; Stalmans et al., 2003; Drake et al., 2006) indicate the importance of well-balanced contribution of VEGF signaling to various aspects of heart morphogenesis, e.g. heart tube bending, valve formation, cardiac septation and outflow tract development. However, little is known about the effects of VEGF overexposure on cardiac progenitor cell motility/migration during early steps of heart development.

Significance of the study

Given the high temporal and spatial complexity of the cascade of events needed for proper heart formation, it is not surprising that many steps of this process are error-prone. High incidence of such errors makes cardiac congenital malformations the most common form of birth defect (affecting 1 out of 100 newborns), as well as the number one cause for prenatal lethality and death from birth defects during the first year of life (Hoffman and Kaplan, 2002). According to the American Heart Association webpage, "nearly twice as many children die from congenital heart disease in the United States each year as die from all forms of childhood cancers combined" (www.heart.org). However, the causes for multiple congenital heart defects are unknown (Gruber and Epstein, 2004).

The work included in this dissertation investigates the processes underlying assembly of three principal components of the early heart – the endocardial, myocardial and ECM layers. The overall goal of this work is to increase our current understanding of a connection between individual cell behaviors and more global tissue displacements/deformations during early vertebrate cardiogenesis. Early heart formation in quail provides an excellent framework for attacking the stated problem, as it involves an interplay between cells of mesenchymal (endocardial) and epithelial (myocardial, endodermal) morphologies, linked via interactions with the ECM into a coherent tissue, that progressively undergoes multiple types of deformations and displacements.

Our study helps elucidate how cardiac progenitor field movement is performed and regulated in amniote embryos; hence in combination with studies on roles of

individual genes in the process, our results may help identify factors with potential teratogenic effects on early cardiogenesis. In turn, this information may be useful for providing recommendations for genetic counseling or dietary/life style suggestions at early stages of pregnancy. Further, the results obtained in our study will broaden our understanding of principles of cardiac progenitor interactions and mechanical interplay with their ECM microenvironment. Such information is potentially useful for cardiac tissue engineering approaches, where ECM-like biomaterial-based scaffolds for heart progenitors are created in order to generate effective cardiac tissue substitutes (Fleischer and Dvir, 2012).

A demand for imaging-based studies of dynamic morphogenetic processes and the clear advantages they offer over “classic” fixed tissue-based approaches have been clearly stated in a number of recent publications (Bussmann et al., 2007; Roeder et al., 2012; Gregg and Butcher, 2012). Our study is unique, as it not only provides minute-by-minute accounts of endocardial and myocardial precursors and ECM fibril movements towards the midline, but also quantifies the observed behaviors in normal and perturbed embryos by means of rigorous computational analysis.

It is known that a significant percentage of congenital heart defects arise due to abnormal development of the cardiac valves (Eisenberg and Markwald, 1995). Although many genetic defects that lead to valve malformations have been identified, in 25% of the cases this morphogenetic event fails separate from any described genetic cause (Armstrong and Bischoff, 2004). This underscores the need for further understanding of the process of assembly and interactions of major participants in early cardiac valve

(endocardial cushion) formation, namely that of endocardial cells and the cardiac jelly ECM. In Chapter 2 we investigate the movements of endocardial progenitors towards the embryonic midline in comparison to their ECM (fibronectin and fibrillin-2) microenvironment. Using several computational analysis approaches we quantify the contributions of active (ECM-independent) and convective (coordinated with the surrounding tissue) movements to the observed endocardial displacements. Our results present the first published evidence that pre-assembled ECM can be transferred to a developing organ, proving both feasibility and importance of such “ECM fate mapping” studies.

It is widely accepted that foregut endoderm and fibronectin are critical for the arrival of cardiac progenitors at the midline, yet most assume their functions to be limited to creating a passive environment for active pre-cardiac cell movements. In our study of myocardial displacements relative to both suggested movement substrata presented in Chapter 3, we uncover coordinated deformations that occur within the developing myocardial primordia. We demonstrate that these deformations may play an important role during heart tube assembly. The computational model developed based on the experimental results obtained herein represents both the anatomy of the myocardium and the surrounding mesoderm, as well as the mechanical activity (bending and spatially restricted contraction) we observe for the myocardium. Model simulations allow us to explore the tissue scale consequences of the assumed myocardial behavior. Thus, our mechanical model allows establishing connection between the tissue and cell-level behaviors.

In Chapter 4, we use exogenous VEGF to induce expansion of the endothelial/endocardial lineage and assess the effects of the perturbation on myocardial movements and endoderm deformations. Our results provide a framework for understanding how mechanical imbalance in the developing tissue can lead to phenotypic defects, such as, in our experiments, delayed cardiac elongation.

Finally, in Chapter 5 we discuss some of the implications of our results as they relate to other studies in the field of cardiac and endoderm morphogenesis, and propose several areas of inquiry that could serve as a logical continuation of the presented work.

CHAPTER TWO:

Convective tissue movements play a major role in avian endocardial morphogenesis

Abstract

Endocardial cells play a critical role in cardiac development and function, forming the innermost layer of the early (tubular) heart, separated from the myocardium by extracellular matrix (ECM). However, knowledge is limited regarding the interactions of cardiac progenitors and surrounding ECM during dramatic tissue rearrangements and concomitant cellular repositioning events that underlie endocardial morphogenesis. By analyzing the movements of immunolabeled ECM components (fibronectin, fibrillin-2) and TIE1 positive endocardial progenitors in time-lapse recordings of quail embryonic development, we demonstrate that the transformation of the primary heart field within the anterior lateral plate mesoderm (LPM) into a tubular heart involves the precise co-movement of primordial endocardial cells with the surrounding ECM. Thus, the ECM of the tubular heart contains filaments that were associated with the anterior LPM at earlier developmental stages. Moreover, endocardial cells exhibit surprisingly little directed active motility, that is, sustained directed movements relative to the surrounding ECM microenvironment. These findings point to the importance of large-scale tissue movements that convect cells to the appropriate positions during cardiac organogenesis.

Introduction

Vertebrate heart morphogenesis, the assembly of a midline tubular heart from bilateral precursor fields, results from an elaborate interplay of events that occur at molecular, cellular and tissue levels of organization. The resulting heart tube is comprised of an inner layer of endocardium separated from the outer myocardium by a layer of extracellular matrix (ECM) termed the cardiac jelly. The interactions between cardiac progenitors and the surrounding ECM during morphogenetic movements are a critical aspect of the development process: the cardiac ECM is involved in the proliferation, differentiation, survival, communication and migration of cardiac cells - by providing an adhesion substrate and sequestering growth factors (Bowers and Baudino, 2010).

Tubular heart assembly takes place in the swiftly moving environment of the forming foregut. The heart splanchnic mesoderm is physically coupled to the underlying endoderm that will form the ventral floor of the foregut. Both structures remain transiently connected via a mesentery until heart looping commences. In addition to tissue movements underlying the elongation of the foregut, the formation of the heart tube also involves substantial rearrangements of myocardial and endocardial precursors (reviewed in Linask, 2003).

Little is known regarding the origin and movements of the endocardial precursors as they form the inner layer of the heart, continuous with the endothelial lining of blood vessels. It is widely believed that endocardial cells share a common precursor with the myocardial cells, but diverge to form a distinct lineage with some shared characteristics

of endothelial cells (Linask, 2003; Harris and Black, 2010). The exact time and place of this divergence is unknown, but studies in avian embryos indicate the two cell lineages segregate prior to or at early gastrulation; i.e. before these cells populate the primary heart field at HH Stage 4 (Reviewed in Ishii et al., 2009). The endocardial precursors differentiate and move into an ECM-rich microenvironment located between the splanchnic mesoderm and endoderm. However, the relationship of mesodermal and endodermal tissue level movements to movements of the endocardial precursor population is largely unknown.

In this study, we establish the morphogenetic movements of both the endocardial precursor cells and ECM fibrils in their microenvironment. We show that the endocardial tube in an amniote (avian) embryo forms and elongates as a consequence of large-scale tissue movements, which carry both endocardial progenitors and their local ECM environment into the forming heart. As a consequence, ECM filaments, originally associated with the anterior LPM are transferred medially where the fibrils incorporate into the cardiac jelly. We also find that the transport of endocardial progenitors is mostly a passive process; their autonomous migration relative to the ECM microenvironment is limited and can be characterized as a slightly biased random walk.

Experimental Procedures

Quail embryo preparation

Fertile wild type (*Coturnix coturnix japonica*) or Tie1::H2B-YFP (Sato et al. 2010) quail eggs (Ozark Egg Co., Stover, MO) were incubated for varying periods of time (from 20 to 36 h) at 37°C to reach stages HH6 to HH11 (Hamburger and Hamilton, 1951). Embryos were then isolated and cultured as in Cui et al., 2009 (modified EC culture; Chapman et al., 2001).

Immunofluorescent labeling of ECM and endothelial/endocardial cells, in vivo

Monoclonal antibodies directed against fibrillin-2 and fibronectin ECM proteins (JB3, B3D6; DSHB, Iowa City, IA) or a quail endothelial cell surface marker (QH1; Pardanaud et al., 1987; DSHB) were directly conjugated to AlexaFluor 488, 555 or 647 (Molecular Probes) according to the manufacturer's instructions. The direct conjugates were injected into the lateral plate mesoderm as 5-40 nl boluses using a PLI-100 (Harvard Instruments) microinjector as described in Little and Drake, 2000. Microinjections were performed 30-60 minutes prior to the beginning of the image acquisition to allow for antibody diffusion and antigen binding.

Wide-field time-lapse imaging

Automated microscopy of immunolabeled quail embryos was performed as described elsewhere (Czirok et al., 2002; Zamir et al., 2008). To enhance contrast, selected epifluorescence image stacks were deconvolved by a commercial, blind adaptive deconvolution software (Autoquant X, MediaCybernetics). Manual tracing of image details, notably the ECM filaments, was performed using custom software (see, e.g., Czirok et al., 2004). As Fig. 3 of Czirok et al., 2004 and Supplemental Fig. 2.1 demonstrate, despite overall changes in ECM organization, the details used to track ECM filaments (such as filament branch points or shapes) are clearly recognizable from frame to frame. The spatial extent of the recognizable features (up to 10 mm) is much smaller than the traced displacements (200 mm to 1 mm). The size of the tracked features thus limits the spatial resolution of the trajectories, but only to an extent comparable to the line width used in the images to represent them.

Post-fixation immunofluorescence labeling

Embryos were fixed and prepared for immunolabeling according to Little and Drake, 2000. Monoclonal antibodies against avian epitopes (JB3, B3D6, QH1), directly conjugated to AlexaFluor 488, 555 or 647, were added at 1:1000 dilutions in 3% BSA for overnight incubation. Nuclei were counterstained with 4′,6-diamidino-2-phenylindole (DAPI) at 300 nM in PBS.

Frozen sections were incubated in 0.5 M $(NH_4)_2SO_4$ for 30 min to remove paraformaldehyde-induced autofluorescence and rinsed with PBS. Subsequently non-specific epitopes were blocked by incubation in 3% BSA solution in PBS for 1h. Monoclonal antibodies against ECM epitopes were added at 1:1000 dilutions in 3% BSA for 2h of incubation. For confocal and epifluorescent imaging whole embryo specimens and sections were mounted on slides with ProLong Gold antifade reagent (Molecular Probes).

Confocal imaging

Confocal imaging of whole-mount embryo specimens was performed using a Nikon 90i upright microscope with a Nikon C1 confocal scan head and Nikon Plan Apochromat 10x and 20x objectives.

Preparation of transverse cryosections

Embryos were fixed in 3% paraformaldehyde for 30 min. Then tissue was rinsed in PBS and subjected to a sucrose gradient (5%, 15%, 30% in PBS), embedded in OCT (Sakura Finetek USA, Inc, Torrance, CA) and stored at - 80°C. Subsequently 10 μm transverse sections were prepared from frozen blocks using a Leica CM3050 cryostat.

Particle Image Velocimetry (PIV) analysis

We used the two step algorithm of Zamir et al., 2005; implemented in MatLab (Mathworks, Inc.) and further detailed in Supplemental Fig. 2.2D, E. Briefly, images were divided into overlapping tiles, each 75 μm wide. The displacements of the tiles were determined by cross-correlation analysis; for each tile we searched the next image for the location that exhibited the most similar intensity pattern. The resulting displacement vectors were then interpolated and denoised by a thin-plate spline fit, yielding our coarse displacement map. This map was used to construct a second, higher resolution one. The cross-correlation procedure was repeated with tiles that were only 30 μm wide. To reduce ambiguities associated with smaller tiles (patterns within smaller tiles are less unique), the subsequent image was scanned only in the vicinity of positions predicted by the coarse map. In this study we did not apply a final smoothing (spline fitting) step, but kept the results of the second cross-correlation analysis.

Within the whole embryo, the ECM label was highly non-uniform, as some areas were exposed to more antibody than others. Image tiles corresponding to areas where the immunofluorescence was weak are very noisy; hence the cross correlation analysis was more error-prone. To reflect this, for each PIV-derived displacement vector we assigned a weight, the local standard deviation of fluorescence intensity. Thus, displacement vectors characterizing a detail-rich region carry more weight in the subsequent analyses than those obtained in a weakly labeled area (see Supplemental Fig. 2.2E).

Automated cell tracking

To track fluorescent nuclei in 3D within a series of image stacks, a novel algorithm, referred to as the CIPA tracker, was developed (Hossain et al; MS in press). Briefly, the algorithm automatically detects a set of prominent cells in the image stack as bright objects, using a multi-stage segmentation approach (see Supplemental Fig. 2.2H). To identify the same cell within a consecutive pair of images, objects that are located within a certain distance are compared by several measures, such as size, brightness or texture similarity. In addition to in-plane searches, the program also probes the two immediately adjacent optical planes to deal with object motion along the z-axis.

Motion analysis

To characterize ECM and cell rearrangements at various stages of heart development, pairs of deconvolved image stacks were selected. The images within the stacks were taken 20 minutes apart. A given pair, *P*, was analyzed through the following procedure. By manual masking (see Supplemental Fig. 2.2C), two additional image stack pairs were derived: one containing the forming heart, the other the somites or the pre-somitic mesoderm (to be used as a reference). The corresponding optical sections and fluorescence channels were compared by PIV analysis as described above. For automated (CIPA) tracking we used all available recorded image stacks within the *time*

interval separating the image pair, P. Velocities (displacements normalized by the time lag between the images of *P*) were presented in a reference system co-moving with the somites. Thus, we use the term “velocity” to describe a vector-value characterizing both the rate and direction of the displacements of selected objects. The term “speed” is used to describe the magnitude of the velocity vector.

Active cell velocities were calculated as the local vectorial difference between the cell- and ECM-derived velocity vectors (Supplemental Fig. 2.2G, I). The “reliability” weight assigned to the vectorial difference is the lesser of the two weights assigned to the vectors. As the CIPA-predicted displacement vectors may point in various directions, even within a small area, we obtained the locally prevalent direction and speed of active motion by replacing each vector by a local average within a radius of 100 μm (Supplemental Fig. 2.2J). To show how disorganized the initial set of vectors within the zone of averaging was, we plotted the standard deviation of the set as a color code. For statistical comparison of embryos, certain areas were selected in the caudal heart and on both sides of the future omphalomesenteric veins. Velocity vectors from different embryos, but within the same location, were pooled. Data obtained from different embryos were considered statistically independent.

Results

The structure of early cardiac ECM

We collected quail embryos at stages ranging from HH8-, when endothelial and endocardial progenitors first demonstrated a strong QH1 immunoreactivity, to HH11. Whole-mount embryos were immunolabeled for QH1 and selected ECM components, fibronectin and fibrillin-2, and the anterior embryonic tissues were subjected to confocal microscopy. At HH8-, ECM fibrils were already abundant in the vicinity of QH1-positive endothelial/endocardial progenitors (Fig. 2.1A, A′), however for later stages we noted an increasing degree of association between fibronectin and vascular progenitors. By HH10, the forming cardiac tube and omphalomesenteric veins were surrounded by a fibronectin "sheath" (red arrows in Fig. 2.1B′, C′).

Fibrillin-2 was organized in coarser structures than fibronectin. Fibrillin-2 fibrils also indicated a certain degree of association with the membranes of endothelial/endocardial progenitors. At HH10 and 11 fibrillin-2 was detected only on the endocardial side of the cardiac jelly (red arrows in Fig. 2.1D′), whereas fibronectin was present on both the myocardial (blue arrow in Fig. 2.1D′) and endocardial sides of the cardiac tube ECM. At the stages investigated, both ECM components were interspersed, but did not colocalize to identical filamentous structures.

Figure 2.1. Endocardial tube assembly takes place in a microenvironment abundant in fibronectin and fibrillin-2 ECM.

A-D: maximum intensity dorso-ventral projections of confocal stacks obtained at HH8- (A), HH8 (B), HH10 (C), HH11 (D) stages of development. Whole mount specimens were immunostained with monoclonal antibodies QH1 (red), B3D6 anti-fibronectin (green), and JB3 anti-fibrillin-2 (blue). A′ - D′: single, 2.5-4 μm thick optical plane images selected from the regions marked with rectangles in panels A-D. In addition to the multicolor merged image, distinct panels show each immunofluorescence label inverted for better contrast. Scale bars: A-D — 100 μm, A′, C′ — 40 μm, B′, D′ — 20 μm. Fibronectin fibrils demonstrate an increasing degree of association with endocardial cell surfaces at progressively later developmental stages (red arrows). Fibronectin is also associated with the myocardium at HH11 (blue arrow). Fibrillin-2 fibrils are somewhat larger in diameter and appear to be aligned with the QH1-positive cell surfaces (A-C, A′-C′, red arrows). Both types of ECM surround the endocardial layer in the assembled heart tube (D, D′).

Figure 2.1

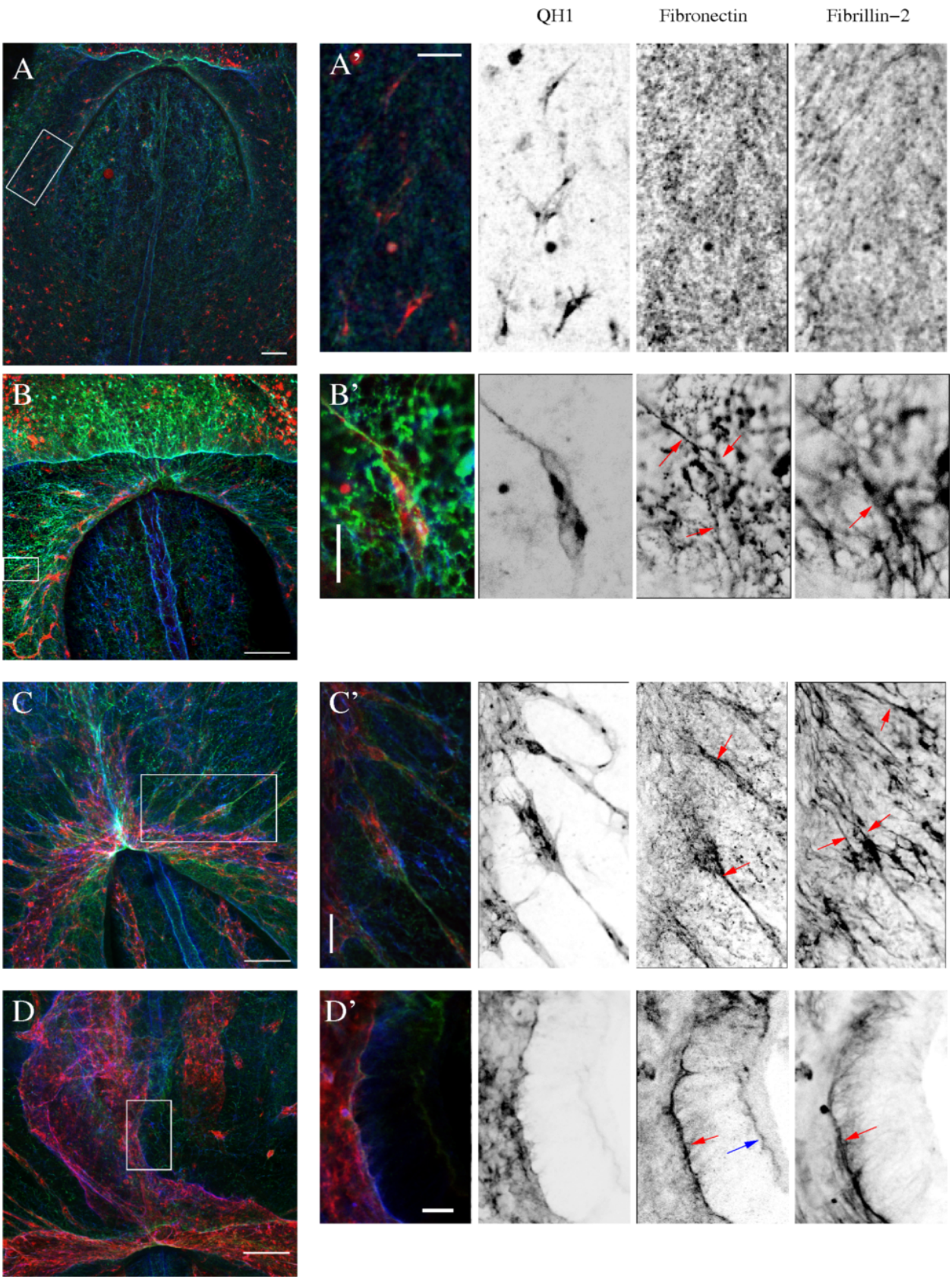

ECM from the caudal embryo contributes to the caudal heart tube

Fibronectin and fibrillin-2 were immunolabeled in vivo with distinct fluorophores in live, HH7 quail embryos (n=9). The specimens were recorded in time-lapse between stage HH8- and HH12. The displacements of individual ECM fibrils were followed using a manual tracking procedure. ECM structures preserved recognizable features during the transition from their initial, lateral positions in the precardiac mesoderm to their inclusion into the cardiac tube ECM at HH10. The large ECM density within the forming heart tube precludes filament tracking at later stages of development. Figure 2.2 and demonstrates that both fibronectin and fibrillin-2 fibrils are engaged first in a centripetal, then in a midline-directed movement. Adjacent trajectories are very similar, regardless of the molecular identity of the tracked ECM component.

By extensive ECM tracing, the anatomical origin of ECM filaments that contribute to the developing heart tube was determined in HH8 embryos. We analyzed n=3 embryos in which both ECM constituents were labeled. Tracking was performed independently for each ECM component. The obtained trajectories were assigned four groups depending on the filament's fate at HH10.

By superimposing the four groups on DIC image sequences, the approximate boundaries were identified for each category of markers (Fig. 2.2B). The resulting ECM positional fate maps were similar for each embryo analyzed as well as for both fibronectin and fibrillin-2. We consistently found that ECM flanking the AIP at HH8- contributed to the anterior one third of the heart tube at HH10 (the red area in Fig. 2.2B).

Bilateral areas located laterally to the caudal segments of the "red" or cranial ECM zone (denoted as yellow areas in Fig. 2.2B) are the source of ECM fibrils that were translocated to the middle portion of the cardiac tube by HH10. The regions contributing ECM to the caudal heart tube and omphalomesenteric veins maps to the posterior ends of the AIP and caudally extends to the level of the second or third somite pair (green areas in Fig. 2.2B). The lateral borders of this caudal-most region closely approach the boundary of the area opaca.

ECM from the cranial embryo is incorporated into the growing heart tube from the cranial end

Upon initial assembly at HH10, the heart tube undergoes rapid elongation of all three contributing layers (endocardium, cardiac jelly and myocardium), concomitant with the onset of looping (Fig. 3.3B). We followed immunolabeled individual ECM fibrils on the ventral surface of the foregut, in the vicinity of the tubular heart. These fibrils are included in the ECM layer separating the foregut endoderm and ventrally positioned splanchnic mesoderm (Fig. 3.3A). Between HH10 and early HH11 a number of ECM fibrils were displaced towards the ventral midline with subsequent inclusion into the anterior pole of the elongating cardiac tube and dorsal mesocardium (Fig. 3.3B). Due to dramatic changes in morphology of the anterior embryo that occur between HH7 and HH10, we could not reliably trace the earlier (prior to HH10) origins of these filaments.

Figure 2.2. Fibronectin (red) and fibrillin-2 (green) fibrils derived from the LPM at HH8- translocate to the heart by HH10.

A: Corresponding epifluorescence (left) and DIC (right) image pairs, representing development between HH8- and HH10. ECM movements are indicated by the superimposed trajectories. Scale bars — 100 μm. B: Schematic fate map of ECM fibrils in a HH8- stage embryo. ECM from the colored areas incorporates into the cranial (red) or middle (yellow) portions of the heart tube, or to the caudal heart tube and the omphalomesenteric veins (green) by HH10. Blue dots indicate ECM fibrils that do not incorporate into the heart. The fate map shown is a representative example out of 3 specimens that were imaged and analyzed by identical methods.

Figure 2.2

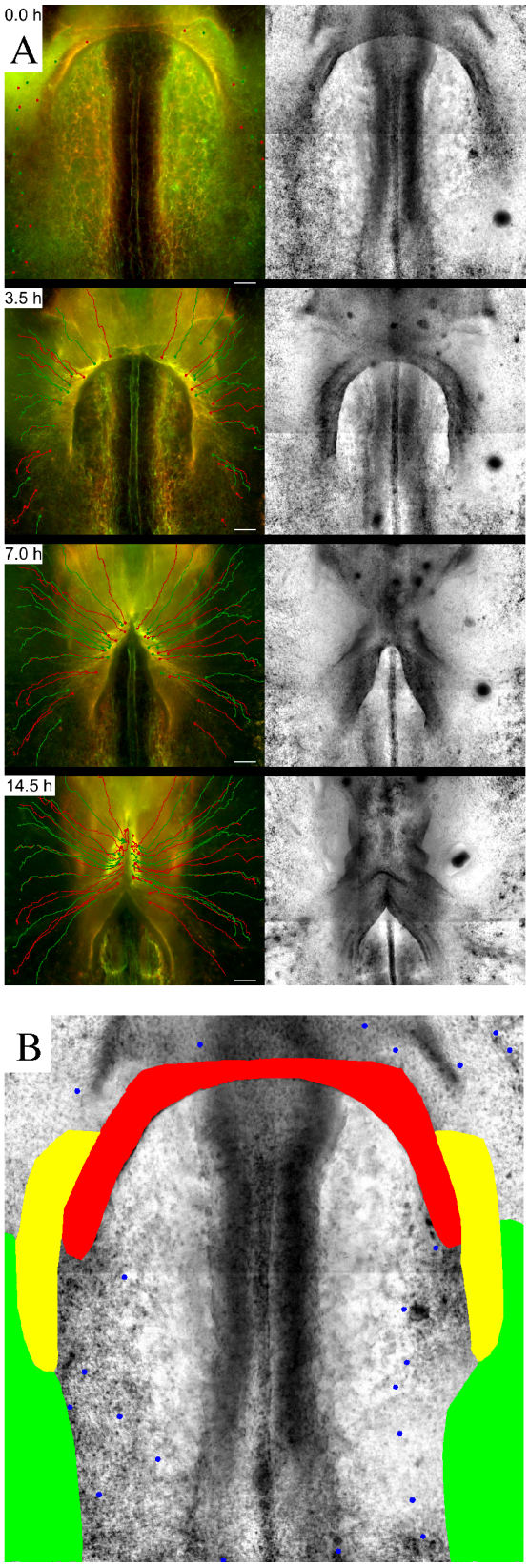

Figure 2.3. ECM positioned ventral to the pharyngeal endoderm is translocated towards the anterior portion of the tubular heart and contributes to its elongation after HH10.

A: Schematic transverse section, adopted from Lillie, 1930. B: Corresponding fibrillin-2 immunofluorescence (left) and DIC (right) image pairs are shown. During the elapsed 4 hours, the length of the cardiac tube substantially increases (DIC panels). Superimposed trajectories of individual fibrils are color-coded: red, green and blue colors indicate progressively later trajectory segments. The movements of fibrillin-2 fibrils are indicated by the red arrows in panel A. Scale bar-100 m.

Figure 2.3

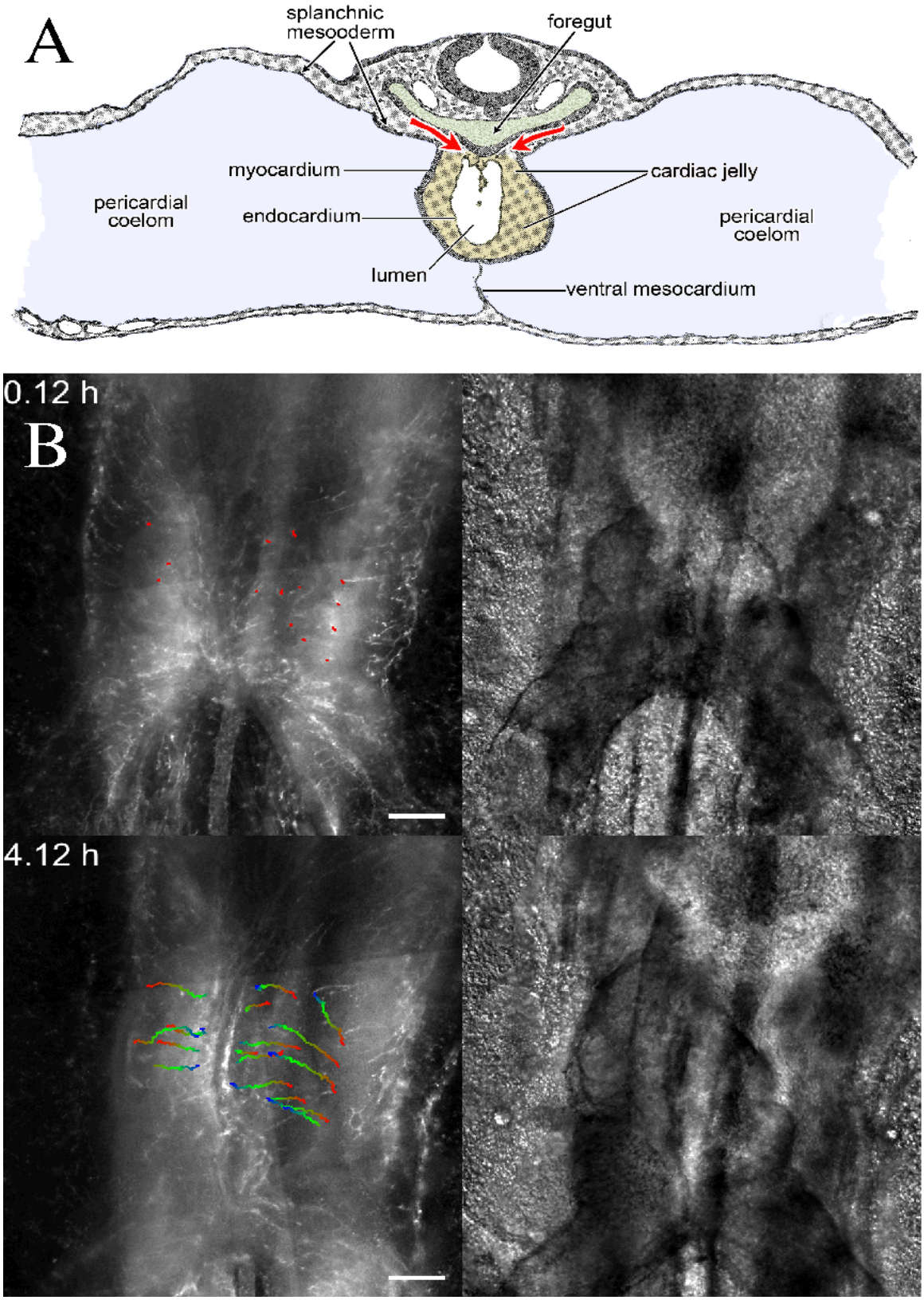
A
splanchnic mesoderm
foregut
myocardium
cardiac jelly
pericardial coelom
endocardium
pericardial coelom
lumen
ventral mesocardium
0.12 h
B
4.12 h

Exogenous fibronectin participates in tissue movement and incorporates into the heart tube along with the endogenous precardiac mesoderm ECM

To show that tagged ECM filaments, suitably located in the anterior LPM, indeed incorporate in the cardiac jelly, we performed experiments utilizing exogenous, fluorescently conjugated human serum fibronectin (BD Biosciences). 7-10 ng of either AlexaFluor647 or 555 fluorophore-labeled fibronectin was delivered subendodermally into the LPM of quail embryos at HH6-8- (n=6). The endogenous fibronectin network of these embryos was also immunolabeled. Recordings of subsequent embryonic development revealed that the exogenously added human fibronectin incorporated into the quail ECM network and participated in its displacements in a manner indistinguishable from endogenous fibronectin molecules (Supplemental Fig. 2.3). As a control, we delivered 100-150 ng of BSA conjugated to AlexaFluor 647 to the contralateral side of each embryo. Time-lapse recordings demonstrated that the BSA signal completely dissipated within 4 hours after injection, whereas the exogenously added fibronectin signal was detectable for up to 12 hours. Furthermore, the distribution of fluorescent BSA was devoid of any fibril-like patterns throughout the experiment.

To determine the position-fates of exogenously added fibronectin in the LPM, 25-30 ng of fluorescently conjugated fibronectin were microinjected into 6-10 adjacent sites along the LPM of HH7-8- embryos (n=12). Injections were performed in such a way that medial (paraxial) and lateral (precardiac) portions of the anterior mesoderm were targeted with differentially labeled fibronectin molecules (Fig. 2.4A, top panel). Time-

lapse imaging was used to record the rearrangements of exogenously added fibronectin occurring between HH8- and 11. Beginning at stage HH8, ECM aggregates derived from the laterally positioned human fibronectin pool are seen to move towards the ventral midline, where fibrils eventually become incorporated in the tubular heart (arrowheads in Fig. 2.4A).

In transverse cryosections of the heart tube we compared the distribution of endogenous and exogenously added fibronectin (Fig. 2.4). The former was detected by immunostaining sections with monoclonal anti-fibronectin antibody, B3D6. In each embryo sectioned following the time-lapse acquisition (n=5), exogenously added fibronectin was found exclusively on the endocardial side of the cardiac jelly (i.e., the basal side of the endocardium). In embryos fixed at HH10 (n=2; data not shown), exogenous fibronectin, delivered to the caudal embryo, was found on the basal side of the endocardium, throughout the length of the cardiac tube. This is consistent with our tracking results (Fig. 2.2), suggesting that (endogenous) fibronectin derived from the caudal embryo gives rise to ECM of the early heart tube (at HH10). At the same time, in embryos fixed at HH11-12 (Fig. 2.4) caudally-derived exogenous fibronectin was mostly found associated with the endocardium in the caudal half of the heart (n=3).

However, if a 10-fold greater amount (200-250 ng) of exogenous fibronectin was delivered to the LPM at HH7, the fluorescent molecule was also found in small amounts on the myocardial side of the cardiac jelly throughout the length of the heart tube, in embryos fixed at HH11 (Supplemental Fig. 2.4). In contrast, no contribution to the cardiac jelly was detected from the medially positioned exogenous fibronectin (green in

Fig. 2.4A) either by time-lapse imaging of live embryos or in transverse sections of fixed tissue (data not shown).

Early endocardial development, visualized by TIE1 promoter activity

The TIE1 promoter is active in endothelial cell progenitors beginning at late HH6 (Sato et al., 2010). Thus, the TIE1:H2B-YFP transgenic embryos offer a novel way to study the movements of future endocardial cells throughout heart development. To analyze the developmental stage-dependent movements of future cardiac ECM and endocardial cells, we identified seven characteristic morphological states of the anterior embryo that we further refer to as endocardial stages, ES1-7 (Supplemental Fig. 2.5). These stages represent a 14-16 hour interval from HH8- to 11. During this time the nascent endocardium undergoes a dramatic transition from a predominantly single-cell progenitor organization to a tubular, lumenized tissue. Our classification scheme is based on the apparent changes in (TIE1+) endocardial organization, and stands in contrast to the standard HH classification of avian embryonic development. Classification of HH stages 7-14 is primarily based on the somite pair number (Hamburger and Hamilton, 1951; Bellairs and Osmond, 2005). However, addition of new somites and progression of endocardial morphogenesis are not always precisely temporally correlated.

At ES1-3 endothelial/endocardial progenitors are flanking the AIP; at this stage the apparent linear distance between the caudal border of the headfold and the

posterior margin of the anterior intestinal portal is minimal, with few Tie1::H2B-YFP+ endocardial progenitors seen at the ventral midline. Although the foregut and the heart tube are at different dorsal/ventral planes, we used an increase in the projected distance between the two anatomical landmarks (viewed ventrally) as the index of foregut regression and midline mesoderm fusion. Both the headfold-to-AIP index (distance) and the number of Tie1::H2B-YFP+ progenitors progressively increased during ES2 and 3.

The ES4 stage was typified by an elongated plexus of Tie1::H2B-YFP+ pre-endocardial cells assembled at the ventral midline, i.e., the nascent endocardial tube. Also, at ES4, aggregations of endothelial/endocardial progenitors mark the sites of the omphalomesenteric veins, which form anterior and ventral to the AIP. By ES5 the developing endocardial plexus/tube has nearly doubled in length. Nascent omphalomesenteric veins incorporate an increasing number of cells at subsequent stages (ES5-7), with the concomitant organization of endothelial cells into tubes. Subsequently, individual small-caliber endocardial tubes fuse to form a single lumenized tube (confirming the findings of Drake et al., 2006). We ranked embryos with linear heart tubes displaying a slight asymmetry to the right as ES6, while “C-shaped” hearts are defined as ES7. With respect to the HH classification, ES1 corresponds to HH8-, ES2-4 to HH8-8+, ES5 to HH9, ES6 to HH10, and ES7 to early HH11.

Figure 2.4. Exogenous fibronectin, injected into the LPM, incorporates into the cardiac tube.

Human fibronectin conjugated to Alexa555 (red) was injected into the anterior LPM at HH7, while fibronectin-Alexa647 (green) was delivered to the paraxial mesoderm and medial-most regions of the LPM. A: Corresponding epifluorescence (left) and DIC (right) image pairs, showing an embryo at HH8- (top), HH8+, HH10, and HH11 (bottom) stages of development. Some fibronectin fibrils derived from the lateral (red) pool are progressively displaced towards the forming heart tube, which begins to exhibit Alexa555 fluorescence at HH10 and 11 (white arrowheads). At the same time, a large portion of the laterally injected fibronectin pool remains associated with mesodermal and endodermal tissues in the anterior embryo. The medially delivered (green) fibronectin pool does not contribute to the cardiac jelly. Scale bars — 100 μm. B-D: Transverse cryosections through the heart tube of the same embryo shown in panel A, fixed at HH 11. Approximate planes of section are indicated in the bottom right frame of panel A. Red fluorescence signal corresponds to the exogenous fibronectin-Alexa555. The green signal shows the distribution of endogenous quail fibronectin, labeled with B3D6 antibody post-sectioning. DAPI staining of cell nuclei is shown in blue. Human fibronectin is present at the endocardial-cardiac jelly interface (asterisks). nc: notochord, e: endocardium, m: myocardium. Scale bars — 40 μm.

Figure 2.4

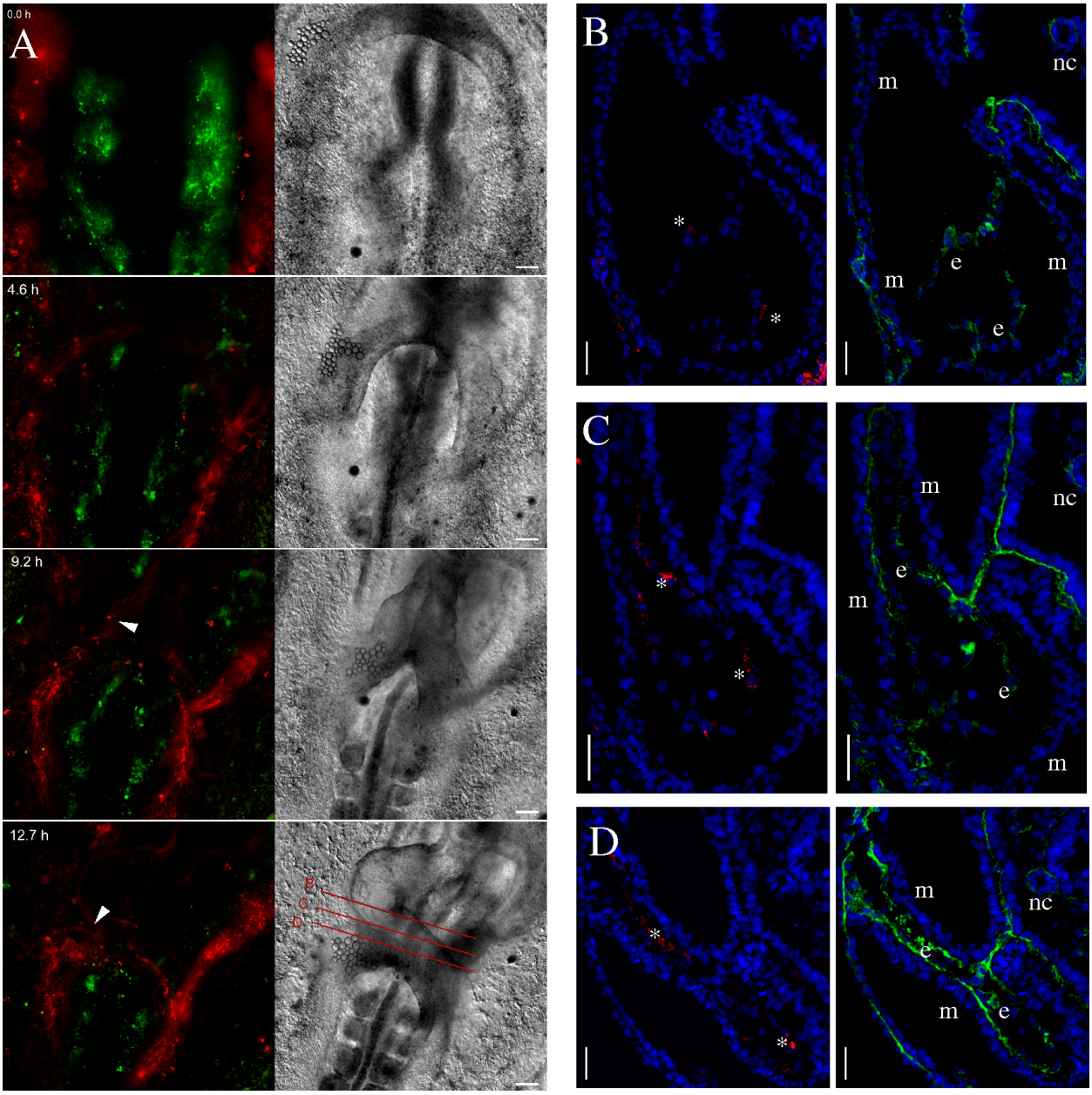

Tissue movements visualized by ECM displacements

Quantitative characterization of ECM movements during early heart development was performed using epifluorescence recordings of 6 embryos, each microinjected with fluorophore-conjugated antibodies labeling fibronectin and fibrillin-2. Image pairs that correspond to the various endocardial stages (ES) were subjected to PIV analysis. In-plane (two-dimensional) ECM displacements were measured in each deconvolved focal plane by independent computations. The velocity data are presented in a reference system co-moving with the somitic mesoderm. This procedure allows us to establish the typical "local" ECM movements characteristic for each stage of the heart development process as well as to compare movements of fibronectin to those of fibrillin-2.

Figure 2.5 shows the pattern and distribution of fibronectin and fibrillin-2, as well as a typical velocity snapshot of their movements in an early (ES1, panel A) and later (ES7, panel B) stage of heart development. In the early stages, the ECM moves centripetally, quite uniformly along the posterior margin of the AIP. In later stages, movements diminish at the anterior aspect of the forming heart, while the posterior aspect of the heart continues its centripetal, medio-posterior expansion.

We compared ECM displacement speeds at three distinct reference points: one located at the most anterior, and two at the left and right portions of the AIP "arch" (Fig. 2.5A and B). An ANOVA analysis comparing the velocity magnitudes at the three locations failed to reveal statistically significant differences at any of the seven endocardial stages investigated ($p>0.5$). Thus, we consider the centripetal contraction of

the posterior margin of the foregut (endodermal tissue) uniform along the whole posterior margin. The speed of centripetal expansion is fastest at ES2 (around 70 μm/h) and drops continuously afterwards (Fig. 2.5C).

At each grid point of the PIV calculation, we can calculate the difference between the displacement vectors characterizing the two ECM components. Except for the first stage (ES1), the mean magnitude of the calculated difference is less than 10% of the magnitude of the total tissue displacement, and this difference may reflect systematic errors in our PIV analysis. Thus, while fibronectin and fibrillin-2 do not co-localize in the same filaments, their tissue-scale displacements are virtually identical at each stage of the transition from planar precardiac mesoderm to formation of the heart tube. Therefore, either fibrillin-2 or fibronectin can be used as a reporter for tissue-scale movements.

Movement of endocardial and endothelial progenitors

To characterize the motile behavior of endocardial and endothelial cells, Tie1::H2B-YFP nuclei were traced in consecutive image stacks both manually and by using the automatic tracker program CIPA. As Fig. 2.6 demonstrates, endocardial and endothelial progenitors may be located near one another at HH8, but then the two groups progressively separate as the endocardial progenitors, located within a horseshoe-shaped field, begin their centripetal movement towards the embryonic midline. The boundary, which separates future endocardial cells from endothelial cells, is quite sharp

(Fig. 2.6A, right panel). Furthermore, the anatomical origin of the cardiac jelly ECM (Fig. 2.2B) closely corresponds to that of the endocardial progenitors.

Representative recordings of Tie1:H2B-YFP embryos, which were also microinjected with fluorophore-labeled ECM antibodies, were analyzed by manually tracking TIE1+ nuclei and ECM filaments. As Fig. 2.6B reveals, cell and ECM trajectories are surprisingly similar. This degree of similarity suggests that the active motility of future endocardial cells is small relative to the local ECM environment. To estimate active cell motility, at each recorded time point we subtracted the average displacement of nearby-traced ECM filaments from the observed cell displacements. As Figs. 2.6C and D demonstrate, the trajectories of active cell movements (red) are random, with little persistence compared to the trajectories of total cell displacements (green) corresponding to Fig. 2.6B.

At HH9-10 the endothelial/endocardial progenitors form a vascular plexus (DeRuiter et al. 1993), associated with splanchnic mesoderm ventral to the foregut. Cells constituting this plexus engage in a midline-directed movement commencing at HH10 and continuing until at least HH12 (Supplemental Fig. 2.6). This movement also correlates in location and timing with the medial-ward ECM motion seen in Fig. 2.3.

To characterize better the active movement of Tie1+ cells, we selected on average six, but at least four, embryos at each stage of heart development (ES1-7). We determined the local ECM movements by PIV analysis; YFP-expressing nuclei were tracked either by the automatic CIPA tracker (raw data not shown) or by PIV analysis (Supplemental Fig. 2.5, panel three). Active cell movements (Supplemental Fig. 2.5,

panel four) were established as the difference between the local (PIV- or CIPA-estimated) cell-based and ECM displacement vectors. This analysis reveals that while the total cell displacements (just like the ECM movements) are centripetal (Supplemental Fig. 2.5, ES3), active cell movements have a medially-directed bias in the medial-most regions of the omphalomesenteric veins (Supplemental Fig. 2.5, ES5), while in the more lateral aspects of these veins, such a medial bias is not observed.

Cellular movement speeds, averaged from multiple specimens, are shown in Fig. 2.7C. As expected, due to the local averaging, values obtained by PIV are somewhat smaller than the values obtained by the CIPA tracker, and both are higher than the values obtained for ECM displacements. The average speed of active cell movement decreases slightly from 20 μm/h to 15 μm/h between the early and later stages of heart development. The calculated mean speed of the lateral drift is 7 +/- 2 μm/h; thus fluctuations in cell speed are substantial, which is in agreement with the random walk-like trajectories calculated in Fig. 2.6D (red plots).

Figure 2.5. Large-scale displacements of fibronectin and fibrillin-2 structures are identical.

A, B: Fibronectin and fibrillin-2 immunostaining (inverted for better contrast) and their superimposed images (third column) are shown together with the corresponding PIV velocity vector map (fourth column). The embryos shown represent an early (ES1, panel A) and a later (ES7, panel B) stage of development. The velocity fields show fibronectin (red vectors) and fibrillin-2 (green vectors) movements in a selected frontal optical plane intersecting the forming heart. Vectors represent velocities as extrapolated displacements during one hour. The reliability of the vectors is indicated by color brightness. Overlap between the two colors appears as yellow. Dots indicate the absence of movement, i.e., velocities smaller than 10 μm/h. Scale bars — 100 μm. C: Mean speed of centripetal ECM movements along the AIP and the inflow region, measured within locations similar to the indicated circles in panels A and B. For each endocardial stage of development, the average speed of ECM displacements is shown for both fibronectin (red) and fibrillin-2 (green). The average magnitude of the difference between the two is presented in yellow. Error bars indicate SEM; distinct specimens were considered statistically independent.

Figure 2.5

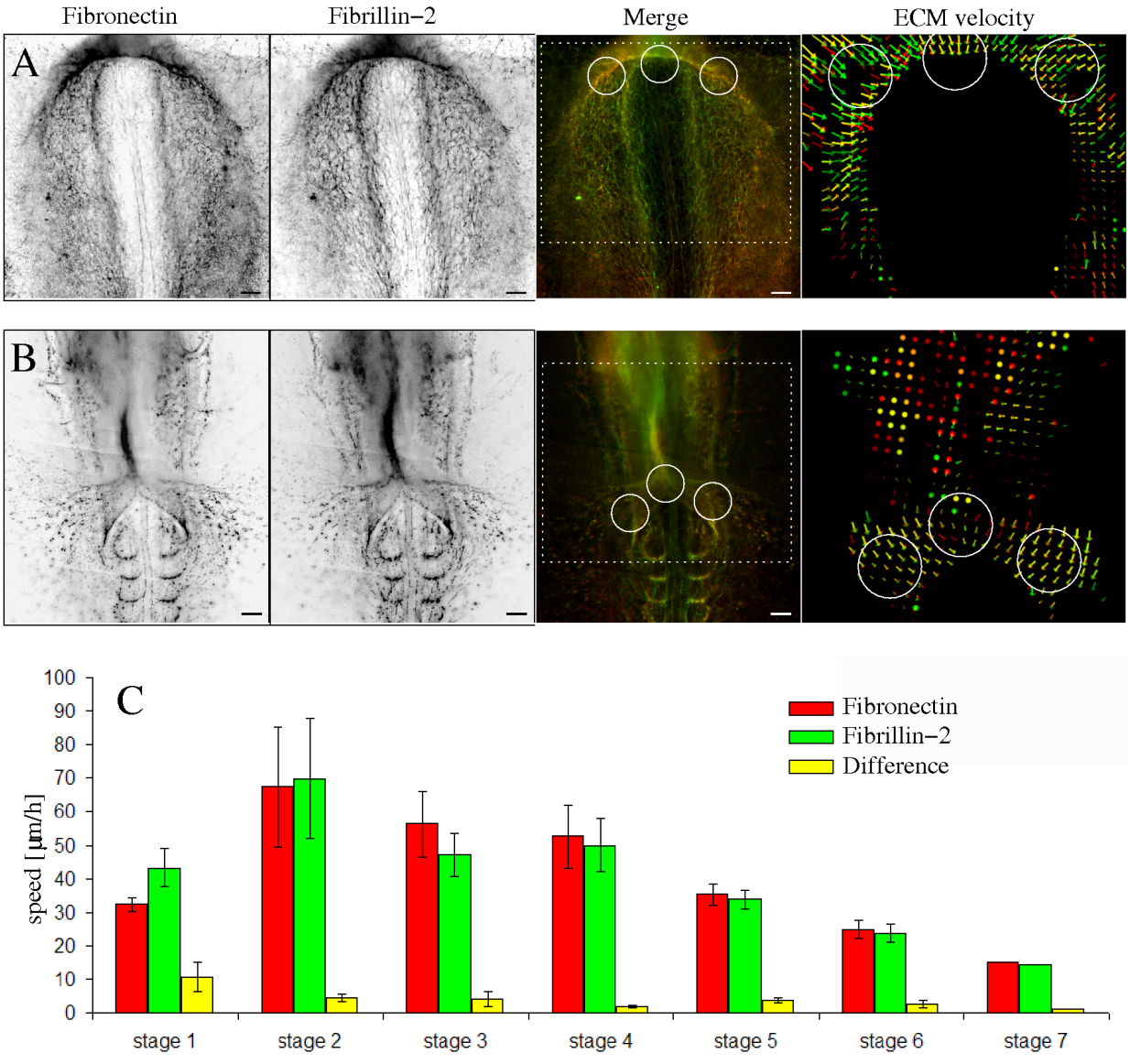
Fibronectin
Fibrillin−2
Merge
ECM velocity
A
B
C
Fibronectin
Fibrillin−2
Difference
speed [µm/h]
100
90
80
70
60
50
40
30
20
10
0
stage 1
stage 2
stage 3
stage 4
stage 5
stage 6
stage 7

Figure 2.6. TIE1+ endocardial progenitors are spatially segregated from the endothelial population and participate in coordinated midline-directed displacement along with the ECM in the adjacent tissue.

A: Epifluorescent images of a Tie1::H2B-YFP transgenic embryo at early (HH8, left) and later (HH9, right) stages of development, with superimposed trajectories of endothelial and endocardial progenitors. Cell trajectories were obtained using the CIPA automated tracking software; the color-code conveys timing information as in Fig. 3. Scale bars — 100 μm. B: Trajectories of manually-traced Tie1::H2B-YFP pre-endocardial cells (green) are compared with those of fibrillin-2 filaments (red). C: Trajectories representing the total (green) and active (red) movements of tracked pre-endocardial cells. Trajectories shown in panel C are re-plotted in such a way that each cell starts from the origin (green trajectories). Active cell movements (red trajectories) were estimated by subtracting the local ECM movements at each frame from the total displacements. D: Mean displacement vs. elapsed time for the total (green symbols) and active (red symbols) cell movements. On a double logarithmic plot a line with slope 1 (green line) indicates persistent motion (displacement and elapsed time are proportional), while a line with slope 1/2 (red line) indicates random walk (displacement is proportional to sqrt(t)). Error bars represent standard deviation, obtained from a pool of all tracked cells.

Figure 2.6

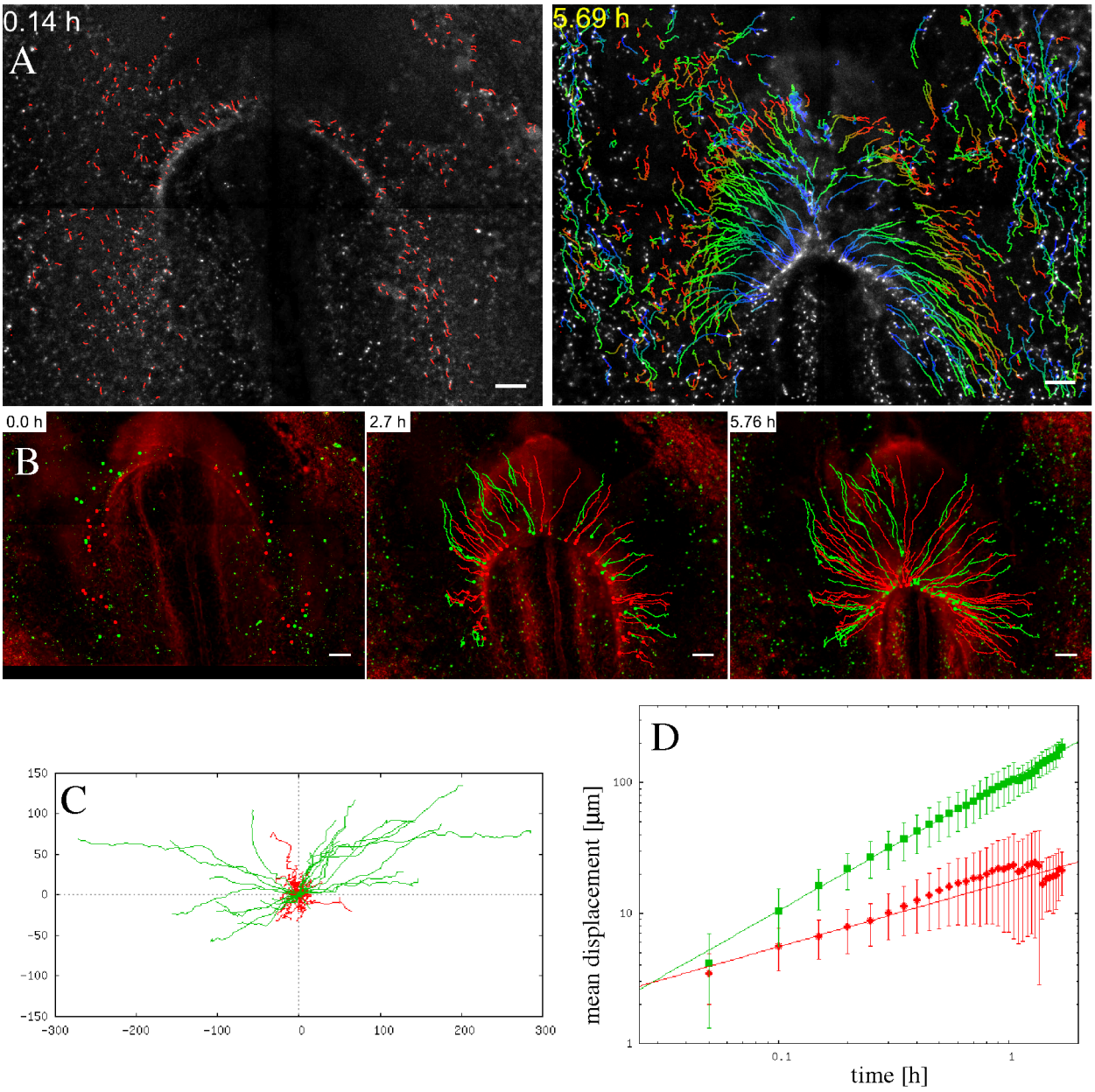
0.14 h
A
5.69 h
0.0 h
B
2.7 h
5.76 h
C
150
100
50
0
-50
-100
-150
-300
-200
-100
0
100
200
300
D
mean displacement [µm]
100
10
1
0.1
1
time [h]

Figure 2.7. Active and total movements of Tie1::H2B-YFP pre-endocardial cells.

A representative specimen is shown at an early (panels A and A′, ES 1) and a later (panels B and B′, ES 7) stage of heart development. Images in panels A and B show velocity vectors (red for ECM and green for cells) in a selected frontal optical plane intersecting the forming heart. Velocities are indicated as extrapolated displacements over a 1h long time period, the yellow square indicates a linear size of 100 μm. The reliability of the vectors is estimated by the contrast of the local fluorescence, and indicated as color brightness. The locally prevalent direction and speed of active cell movements was determined by averaging the vectors of active cell velocities within a radius of 100 μm. These vectors, projected to a frontal plane, are shown in A′ and B′, and thus represent the local directional bias of active cell movements. The color assigned to the vectors indicates the local standard deviation of active cell movements: blue and red colors indicate locally ordered (small standard deviation — vectors pointing in similar directions) and disordered movements, respectively. Notice the tendency to move towards the heart in the vicinity of the forming heart tube (asterisks). C: Speeds of active (bars 1 and 2) and total (bars 3 and 4) cell movements, the corresponding speed of ECM displacements (bar 6), and for comparison the calculated difference in the movements of the two ECM components (bar 5) are shown for the seven stages of endocardial development (See Supplemental Fig. 5). Cell displacements are estimated by two methods, PIV (bars 1 and 3) and automated cell tracking (bars 2 and 4), and yield similar results.

Figure 2.7

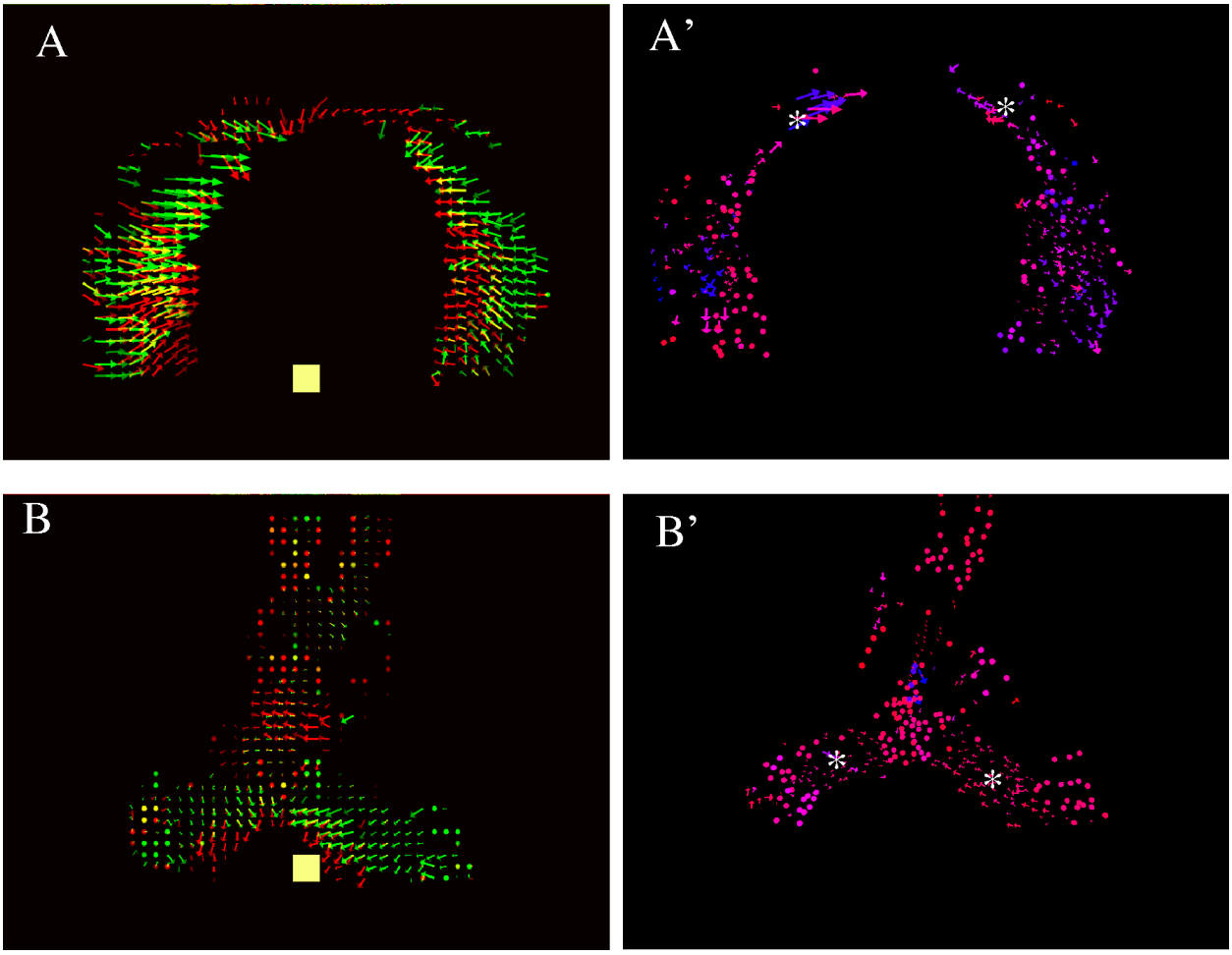

Tissue movements are able to convect passive objects

To give further support to the idea that minimal autonomous directed motion is required from the endocardial cells to construct the heart, we tested whether passive objects placed in the vicinity of the precardiac mesoderm are transferred to the heart tube by means of global tissue flow. We performed the experiments using embryos (n=3) in which fibrillin-2 was immunolabeled at HH7-8- (right before or at ES1). Subsequently, latex beads, 6.5 μm, were placed under the endoderm by a series of microinjections. Delivery of the beads was targeted to the regions that correspond to the position of precardiac mesoderm at HH 7 as defined in recent fate mapping studies (Cui et al, 2009; Abu-Issa, Kirby, 2008). Time-lapse imaging commenced at HH8 (ES1-2) and continued until HH11-12 (ES7 and beyond). For analysis, we selected the groups of beads that moved towards the ventral midline and incorporated into the heart tube (based on subsequent confocal analysis).

Beads placed caudal to the AIP entered the heart tube from the inflow end (e.g. the group of beads indicated with an (a) in Fig. 8). Beads positioned ventrally to the foregut at HH8 [groups marked with (b) and (c) in Fig. 8] were incorporated into the forming heart tube from its anterior (outflow) pole. Both outcomes correlate with the position-fates of the ECM in corresponding areas (Figs. 2.2 and 2.3). Moreover, PIV analysis of bead velocities results in similar values to those of adjacent fibrillin-2 ECM (data not shown). The calculated difference between the displacement vectors of the two components is less than 10% of the magnitude of total tissue displacements: a finding that also serves as a negative control for our active motility calculations.

Figure 2.8. Tissue motion transfers passive objects to the site of cardiogenesis.

A: Microinjected latex beads (green) within a HH8- embryo, also immunolabeled for fibrillin-2 (red). Arrows a-c indicate groups of beads that were incorporated in the forming heart tube at HH12. B: Confocal micrograph of the same embryo at HH12, immunostained with QH1 antibody. A 24 μm thick confocal stack through the heart tube was obtained along the dorso-ventral axis. The image shown is a maximum intensity projection, beads are shown in green, fibrillin-2 in red and QH1 in blue. As determined by tracking the beads through the time-lapse image sequence, arrows a-c indicate identical groups of beads in both panels. In agreement to our results shown in Figs. 2 and 3, the group of beads indicated by (a) entered the heart tube from the caudal end, and those indicated by (b) and (c) were included in the forming heart from the cranial pole.

Figure 2.8

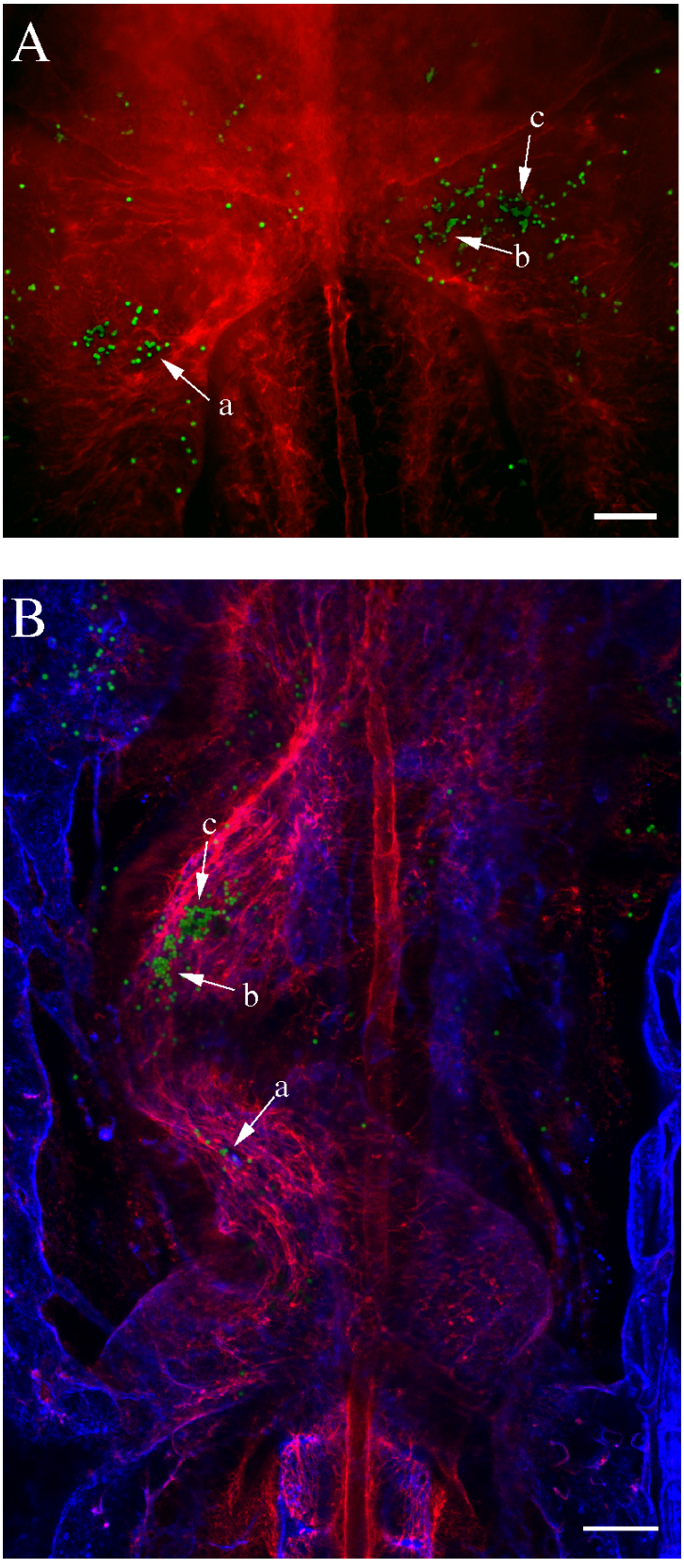

Discussion

The source of early cardiac ECM

At early stages, components of the primitive heart ECM (including ECM associated with the heart splanchnic mesoderm and endoderm) include collagens I, IV, fibrillins -1 and -2, fibronectin, and laminin (Drake et al., 1990). It is believed that many of these components persist and contribute to the cardiac jelly at tubular heart stages (reviewed in Little and Rongish, 1995).

The current understanding of cardiac jelly formation between the myocardium and endocardium relies on the biochemical studies of Krug et al (1985). As the endocardial and myocardial tubes are fusing at the ventral midline, the myocardium secretes a thick acellular matrix that helps to separate the two cell layers of the heart. The cardiac jelly exists as the fusion between this larger myocardially-derived BM (having a lamina densa and an extended reticular lamina) and an attenuated, endothelial-associated BM (composed only of a lamina densa), but is not itself organized as a basement membrane-like structure (Kitten et al., 1987).

The myocardium, however, does not secrete all components of the cardiac ECM. In rat embryos the mesoderm actively expresses fibronectin at the early primitive streak stages, but then this expression ceases at the pre-headfold stage. Fibronectin expression is resumed by endocardial cells in the early heart tube at the 5-somite stage (Suzuki et al., 1995), which morphologically corresponds to HH8+ in avians. The endocardium continues to actively express fibronectin until the 14-somite (HH11 stage).

In contrast, myocardial cells do not express fibronectin at any of these early stages of development. Thus, the endocardium is believed to be the main source of fibronectin in the cardiac jelly.

In addition to ECM components produced “de novo”, in this work we demonstrate that fibronectin and fibrillin-2 filaments (both endogenous and exogenously-added), which are associated with the LPM at HH8, become incorporated into the cardiac jelly by HH11. The ratio of the transported and newly-synthesized ECM is difficult to estimate. Our time-lapse recordings as well as confocal microscopy studies indicate that the incorporated, endogenous, labeled ECM is abundant enough to form an ECM-dense layer that is continuous at the resolution of optical microscopy.

ECM movements

This work represents the first demonstration of ECM filaments being translocated and incorporated into a future organ. Our group has previously shown that fibrillin or fibronectin-containing ECM fibrils are convected during primitive streak formation and gastrulation (Zamir et al., 2006; 2008) and vertebrate axis formation (Czirok et al., 2004). Further, recent work by others showed fibronectin fibrils are translocated in the presomitic mesoderm during avian axis elongation (Benazeraf at al., 2010).

Like cardiac precursor cells, ECM filaments are displaced and enter into the forming heart tube at both the anterior and posterior regions. The ECM is added to the elongating heart tube concomitantly with the addition of cardiac segments. The area of

the LPM that contributes ECM to the forming heart closely corresponds to the fate map of myocardial precursors (Cui et al., 2009) and our data on endocardial precursor cell origin (See Fig. 6). Like the cells contributing to the primary heart field, the ECM fibrils come from specified regions of the embryo and maintain their anterior-posterior relationships to one another (Figure 2.2). Thus, both cellular and ECM fate maps have three somewhat overlapping regions which distribute to different portions of the heart along the anterior-posterior axis. The ECM and cells contributing to the anterior portion of the Stage 10 heart tube were observed in the anterior-most "arch" spanning the embryonic midline (Figs. 2.2 and 2.6).

ECM movements and morphogen gradients

The maintenance of anterior-posterior positional order during the time the cardiac jelly (fibronectin and fibrillin-2) is accumulated (Fig. 2.2) has implications for the establishment/maintenance of ECM-bound morphogen gradients. If gradients of morphogens are "pre-established" outside of the forming heart tube, and if the ECM-bound morphogens are then swept into the heart with the same relative positions, a corresponding anterior-posterior morphogen gradient may be maintained. Similarly, any left/right asymmetry in the distribution of ECM molecules/bound morphogens in the lateral plate would likely be maintained in the heart tube.

Although we have no direct evidence that fibronectin and/or fibrillin-2 are binding morphogens key to heart morphogenesis, other studies have shown that fibronectin

controls the availability of growth factors such as TGFbeta (Fontana et al., 2005; Leiss et al, 2008), and can bind VEGF (Wijelath et al. 2002), in some cases acting in a synergistic manner with heparan sulfate (Stenzel et al., 2011). In addition, although this study focused on the movements of fibronectin and fibrillin-2, we propose that other ECM components (including those that bind morphogens) likewise are displaced as part of an interconnected ECM scaffold; indeed it is difficult to argue that the ECM does not move as a composite material.

In general terms, the cells closest to a source of a given morphogen are believed to be exposed to a higher concentration gradient of that morphogen. Thus, endocardial cells moving with their nearby ECM (and any ECM bound morphogens) toward the midline have the *potential* to be exposed to a relatively "static" morphogen level, provided the morphogen bioavailability also remains constant. The degree to which cells are sensitive to the ECM-bound morphogens is influenced by numerous factors, including: 1) the rate of morphogen accumulation, 2) the time between morphogen secretion and binding to the ECM, 3) the length of time a given morphogen remains bound to the ECM, 4) the spatiotemporal activity of potential proteolytic enzymes, 5) the "half-life of the morphogen in solution, 6) the location of binding partners/receptors and 7) the morphogen diffusion rate (Yu et al., 2009; Drocco et al., 2011). Thus, although potential target cells and ECM-bound morphogens move together, it is entirely possible that the displacements of the ECM could have little bearing on the morphogen gradient. If a morphogen is secreted by a cell and is quickly bound to nearby ECM, and if that morphogen remains bound for only a short period of time, then the movement of the

ECM is not a major influence on the repositioning of the morphogen (i.e. the morphogen is not “carried” by the ECM any substantial distance).

The fact remains that the ECM is highly dynamic, and that at the tissue-level scale, its movements are predictable and reproducible (Fig. 2.2). These empirical data indicate the need to study cell signaling within the context of a physiologically relevant, highly dynamic ECM environment.

The source of endocardial cells

Cardiac progenitors are among the first cell populations to undergo ingression through the primitive streak, which in turn is followed by their rapid anterior and lateral movements. Subsequently, cardiac progenitor cells, i.e. those cells that will reside in the midline heart tube by HH 10, assume their temporary residency within a specific area of the anterior lateral plate splanchnic mesoderm, generally referred to as the primary heart field. It is a widely-held belief that early in avian cardiovascular development (HH 5), both the myocardial and endocardial cells are found in this primary heart-forming region. However, recent work by Tzahor and colleagues (Milgrom-Hoffman et al., 2011) in the chick embryo indicate the endocardial-forming field is situated outside of the cardiac crescent, and is continuous with the vascular endothelial plexus. Their work suggests an endothelial origin of the endocardium. Thus, controversy still exists over when and where the two avian cardiac lineages and the endothelial lineage(s) are first specified and the exact location and extent of the respective precursor fields (Cui et al.,

2009; reviewed in Harris and Black, 2010). In contrast, in zebrafish the endocardium originates from a distinct region in the anterior cardiogenic mesoderm, located more rostral than the source of myocardial progenitors (Bussmann et al., 2007; Schoenebeck et al., 2007).

Regardless of when and where the endocardial precursors are first specified, the endocardium arises through a process of de novo vasculogenesis from a distinct population of precursors in the anterior lateral plate mesoderm. We have demonstrated that pre-endocardial cells and vascular endothelial cells are separated by a sharp horseshoe-shaped boundary within the anterior LPM (Fig. 2.6). We believe that cells located on the “endocardial” side of this boundary are subject to the midline-directed tissue movement. While we are not in a position to claim that position fate is the only determinant of these two cohorts of Tie1+ precursors, we do believe that position fate plays an important role in the formation of blood vessels versus the endocardium.

The endocardial tube is formed from the bilateral field of endocardial precursors by the centripetal movement of these cells along the posterior margin of the anterior intestinal portal; importantly the cells positioned at the midline and lateral margins appear to move with the same speed. After HH10, as the endocardial tube continues to elongate, we see cells contributing to the endocardium from the closely associated vascular plexus located ventral to the foregut endoderm (Supplemental Fig. 2.6).

By developing a system of substages between HH8- to 11 (Supplemental Fig. 2.5), which better characterize endocardial morphology, we show the reproducibility in the progression of endocardial formation from a scattered pool of precursors initially

located between the anterior LPM and endoderm. The seven substages, which we refer to as ES1 - ES7, are distinguishable from one another by the characteristics of the Tie+ positive cells and the morphological events that are occurring concomitant with endocardial morphogenesis. As discussed in detail in the results, defining characteristics included the number, location and organization of the Tie+ endocardial precursors as well as the general morphology of the cranial embryo as it relates to elongation of the foregut, regression of the anterior intestinal portal, and elongation of the endocardial tube and cardiac bending.

Tissue and active cell movements

The most likely interpretation for the shared large-scale movement pattern between the two ECM components and endocardial progenitors is a model whereby the whole tissue (cells and the associated ECM as a composite material) moves and deforms in response to mechanical forces, exerted by cells within the heart field or in adjacent tissue layers. The finding that microinjected inert objects also translocate to the forming heart, in an identical manner, is entirely consistent with such a view. In previous works, we have operationally defined “tissue motion” as the coordinated movements of cells and their local ECM environment (Zamir et al., 2006; 2008; Czirok et al., 2006; Perryn et al., 2008; Sato et al., 2010). Displacements associated with tissue motion are correlated over large distances, up to a several hundred microns (Szabo et al., 2011). As we have shown in this work, active motility of endocardial progenitors, defined as the

difference between the local cell and ECM displacements, is much smaller and more random than the movements characterizing tissue deformation. The randomness and smaller scale of active cell movements was recently also demonstrated for cells of the pre-somitic mesoderm (Benazeraf et al., 2010).

Although our work clearly shows that tissue motion predominates in the repositioning of pre-endocardial cells to form the midline endocardial tube, it is important to determine what role the cell autonomous motility plays in endocardial morphogenesis. The random active cell movements can play an important role in the reorganization of the local ECM. At later stages of cardiac development, the observed directional component of the autonomous motion may be critical for the precise repositioning of the precursors. The calculated autonomous speeds of 20 μm/h are in the same range as those reported for endothelial cells moving in culture (10 μm/h: Szabo et al., 2010, 50 μm/h: Kouvroukoglou et al., 2000). In comparison, the active movement of gastrulating mesoderm cells are somewhat faster, in the range of 60 μm/h (Zamir et al., 2006).

The driving forces for endocardial progenitor motion are likely to differ between avian (and other higher vertebrate) embryos and zebrafish; the latter model system has been used for studies of endocardial morphogenesis in a number of recent studies (Bussmann et al., 2007; Schoenebeck et al., 2007; Fish et al., 2011). Even though many aspects of cardiac development are very similar in zebrafish and avians (reviewed in Alexander and Stainier, 1999), some significant differences exist and must be taken into account. For instance, Bussmann et al. (2007) described two facets of endocardial morphogenesis distinct in zebrafish and higher vertebrates. First, unlike in avian

embryos, zebrafish endocardial progenitors engage in posterior movements from the discrete region they occupy in the cardiogenic mesoderm to the site of the heart tube assembly. Second, in contrast to our results in the avian embryo, in fish embryos, endocardial precursors appear to rapidly migrate to the site of heart tube formation, where they arrive and form a sheet prior to the formation of bilateral myocardial primordia and initiation of their midline-directed movements (Bussmann et al., 2007). After their arrival at the ventral midline, endocardial cells direct angular movements of myocardial progenitors in zebrafish (Holtzman et al., 2007). Bussmann et al. also pointed out the virtual absence of dynamic imaging-based studies of endocardial progenitor motion in avian or mouse embryos, a gap that the current study aims to help fill.

In contrast to zebrafish endocardial morphogenesis, assembly of the avian endocardium occurs simultaneously with that of the myocardium, and both cell types simultaneously engage in antero-medial motion. This points to myocardial movements as the potential driving force for tissue motion, a force in turn that leads to endocardial cell displacements. The coordinated movements of myocardial cell populations were indeed suggested to “drive” the formation of the heart tube in chick (DeHaan 1963) and in rat (Suzuki et al., 1995). However, since the endocardial cells are clearly moving with the associated ECM, such a mechanism would require another adhesion substrate, i.e., a layer of ECM distinct from the one associated with the endocardial precursors. Our monoclonal antibody labeling of endogenous fibrillin-2 and fibronectin do not show such distinct ECM layers in optical or physical sections. Potentially myocardial progenitors

could move relative to ECM components not fluorescently labeled in this study. However, given the importance of fibronectin for myocardial movements (Linask and Lash, 1986; Trinh and Stainier, 2004) one would expect myocardial progenitors to rely on it as the adhesion substrate, at least in part. Surprisingly though, our recent preliminary data suggest that myocardial cell movements relative to fibronectin ECM are relatively small, and are very similar in speed and magnitude to endocardial precursor active movements.

Another tissue candidate potentially responsible for driving tissue movement in the anterior embryo is the endoderm. This function would complement an important signaling role of the endoderm in cardiac development, reported for zebrafish, *Xenopus*, chick and mouse (Lough and Sugi, 2000). In avian embryos (as well as mouse and human), the endoderm undergoes a series of morphogenetic movements, involving dramatic tissue folding events, to form the gut tube. Elongation of the formed gut involves rapid posterior movement of the anterior intestinal portal (AIP), concomitant with narrowing of the endodermal tube. The foregut and the heart tube are physically associated via a mesentery (dorsal mesocardium) throughout the initial cardiac assembly stages, making the movements of the endoderm and cardiogenic mesoderm tightly coupled.

The mechanisms that drive foregut assembly and elongation remain poorly understood in avian and mammalian systems. Stalsberg and DeHaan (1968) suggested that in avians, the foregut elongates as a result of tension applied at the anterior intestinal portal, and the tension arises from the regression of the primitive streak and

elongation of the notochord. The same force may be transmitted to the subjacent splanchnic mesoderm (including cardiogenic mesoderm), acting to drag that layer medially and caudally (Stalsberg and DeHaan, 1968). In the mouse, foregut and heart tube formation were suggested to depend upon visceral extraembryonic endoderm movements (Narita et al., 1997). Further, in studies in which the transcription factor GATA4 (expressed in precardiac splanchnic mesoderm and foregut endoderm) has been knocked out, visceral endoderm defects, gut malformations, and abnormal heart morphogenesis result (Kuo et a., 1997; Molkentin et al., 1997; discussed in Rojas et al., 2010). The authors demonstrate that GATA4 has a role in the formation of the anterior intestinal portal, and subsequent foregut and heart tube morphogenesis via a role in lateral to ventral folding. The mechanism of gut formation is different in zebrafish and *Xenopus*, where the endoderm forms from a "rod" of cells, which develops a lumen and gives rise to the gut tube (reviewed in Spence et al., 2011).

Recently the local residual stresses were mapped in the early epiblast and a tissue mechanical model was proposed for headfold formation (Varner et al., 2010). We expect an approach similar to Varner and colleagues would aid in our understanding of the underlying mechanisms of foregut formation and its possible role in driving cardiac progenitor displacements to the ventral midline.

The work presented here lays the basis for our ongoing and future studies aimed at the characterization of the relative movements of endocardial and myocardial progenitor cells, their ECM environment and surrounding non-cardiac cell populations in live developing avian embryos. In addition to experimental embryology and imaging

approaches, it is clear that mathematical modeling will prove useful in determining what biophysical mechanism(s), such as force generation, are necessary to form the cardiac tube at the midline.

Supplemental figures

Figure S2.1. Fluorescent antibody-mediated in vivo labeling of ECM, combined with epifluorescence time lapse microscopy, provides sufficient resolution to allow tracing of ECM aggregates (fibrils) in time and space.

Top panels demonstrate individual frames from a time-lapse image sequence, describing the development of a quail embryo with the fibrillin-2 ECM labeled (in vivo) using JB3 antibody-AlexaFluor488 conjugate. Bottom panels contain the regions delineated with rectangles in each of the top panels. Time elapsed from the beginning of image acquisition is indicated in the top left corner of each image. Example ECM aggregates with recognizable morphology are demarcated with red, blue, and green ellipses in each of the bottom panels, with each color corresponding to the same ECM aggregate in every image. Scale bars – 100 μm.

Figure S2.1

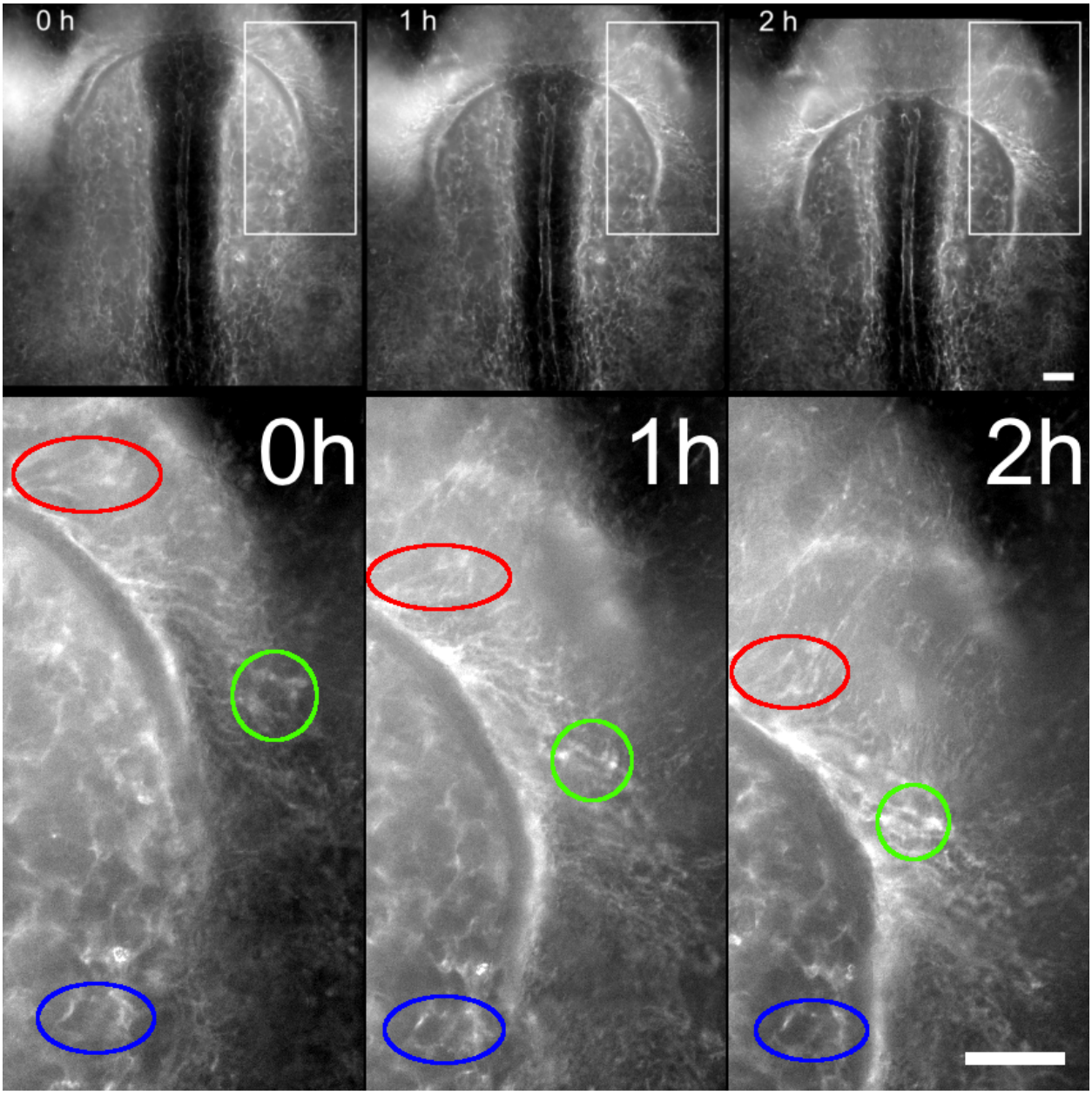

Figure S2.2. Image processing workflow to analyze cell and ECM displacements during heart formation.

A: Block diagram representing the various stages of data analysis. The process is demonstrated through images shown in panels B-J. B: Image pairs characteristic for a certain stage of heart development are selected. The two sets of images were acquired 20 minutes apart, in multiple focal (Z) planes and multiple microscopy modes. Here two deconvolved sections are shown, characteristic for an endocardial stage (ES) 3 heart. The red and green channels represent fibronectin immunofluorescence and TIE1 positive nuclei, respectively. C: By a manual masking procedure, image regions are selected that contain either the forming heart (Ca), or the paraxial or somitic mesoderm for anatomical reference used later (Cb). Images shown are obtained from panel Ba: a similar procedure is applied for the image shown in panel Bb. D: PIV displacement estimation for the TIE1+ nuclei (Da), pre-cardiac ECM (Db) and reference ECM (Dc). The images depict the analyzed fluorescence pattern both at the earlier (red) and later (green) time points. The PIV-derived displacement vectors are represented with white lines, with a circle at their end point. Areas shown in higher magnification allow the comparison of the PIV vectors with the corresponding patterns. Easily recognizable patterns are marked by cyan circles. E: The PIV data are weighted by the local standard deviation of the immunofluorescence intensity. Here the weights are represented as gray scales: white vectors represent highly reliable data obtained from detail-rich areas, while black (or transparent) displacement vectors indicate data obtained from low signal

areas. F: Cell (green) and ECM (red) displacement data in a reference system co-moving with the embryonic axis. Thus, the lateral shift of the embryo apparent in Panels Dc and Ec was compensated for. The square represents an area of 100 mm X 100 mm. G: Active cell movements (white), calculated as the difference of the apparent cell displacements (green) and ECM displacements (red) displayed in panel F. Displacements smaller than 10 μm are represented as dots. H: Individual displacements of TIE1+ nuclei, obtained using the automatic CIPA tracker. Two deconvolved images acquired within three minutes are shown, the earlier in the red and the later in the green channel. The CIPA-predicted displacements are represented as white tracks with the current location denoted by an open circle. I: Active movement of TIE1+ cells (white), calculated as the difference of the apparent CIPA-predicted displacements (green) and PIV-predicted ECM displacements (red). J: As the CIPA-predicted displacement vectors may point in various directions even within a small area (asterisk), we obtained the locally prevalent direction and speed of active motion by replacing each vector by a local average within a 100 μm radius. To show how disorganized the initial set of vectors within the zone of averaging are, we plot the standard deviation of the set as a color code. Red colors represent smaller standard deviation (hash mark), while blue colors designate more disoriented movements (asterisk).

Figure S2.2A

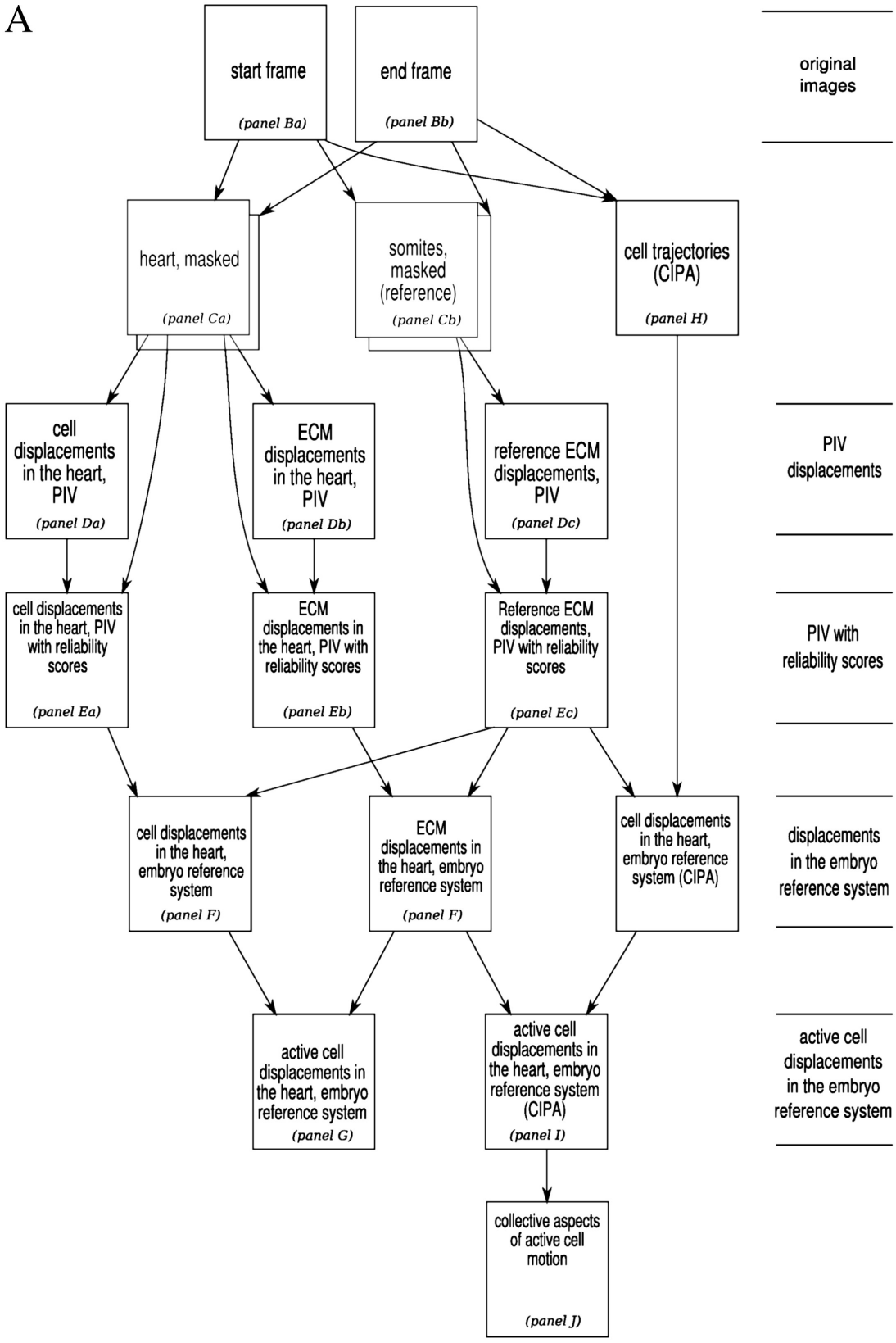
A
start frame
(panel Ba)
end frame
(panel Bb)
original images
heart, masked
(panel Ca)
somites, masked (reference)
(panel Cb)
cell trajectories (CIPA)
(panel H)
cell displacements in the heart, PIV
(panel Da)
ECM displacements in the heart, PIV
(panel Db)
reference ECM displacements, PIV
(panel Dc)
PIV displacements
cell displacements in the heart, PIV with reliability scores
(panel Ea)
ECM displacements in the heart, PIV with reliability scores
(panel Eb)
Reference ECM displacements, PIV with reliability scores
(panel Ec)
PIV with reliability scores
cell displacements in the heart, embryo reference system
(panel F)
ECM displacements in the heart, embryo reference system
(panel F)
cell displacements in the heart, embryo reference system (CIPA)
displacements in the embryo reference system
active cell displacements in the heart, embryo reference system
(panel G)
active cell displacements in the heart, embryo reference system (CIPA)
(panel I)
active cell displacements in the embryo reference system
collective aspects of active cell motion
(panel J)

Figure S2.2B, C, D, E

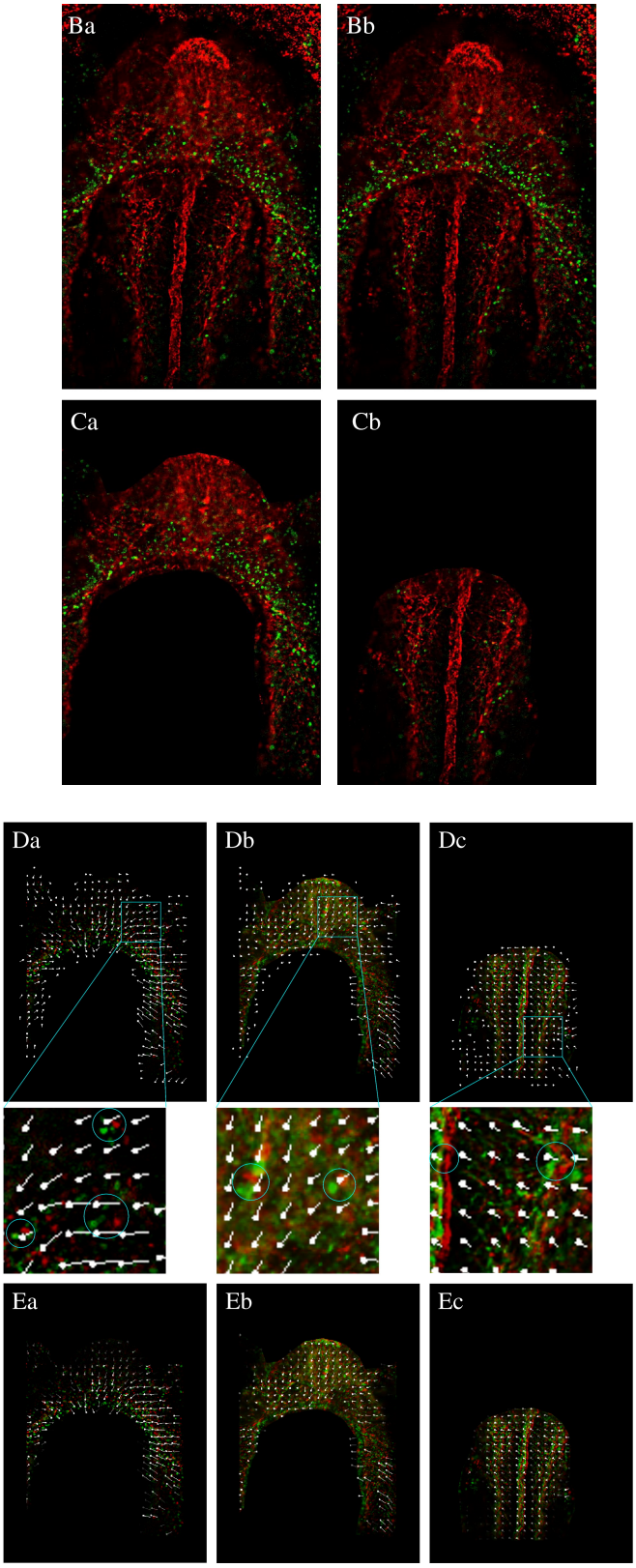

Figure S2.2F, G, H, I

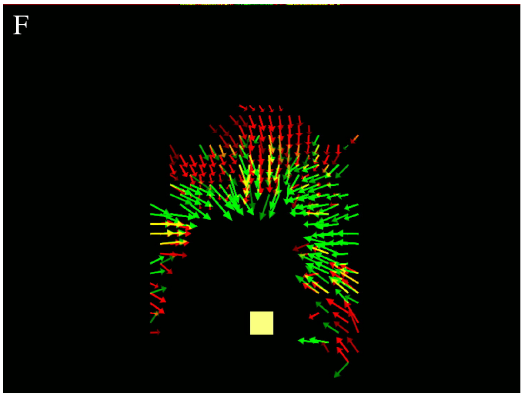

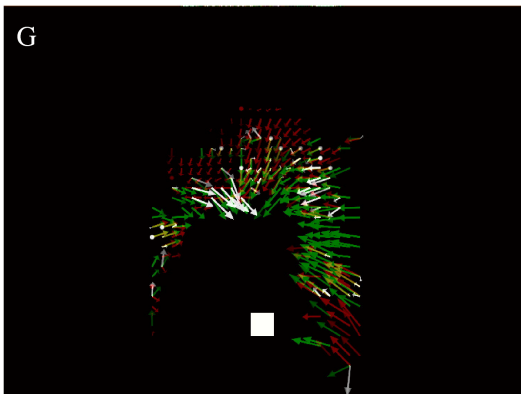

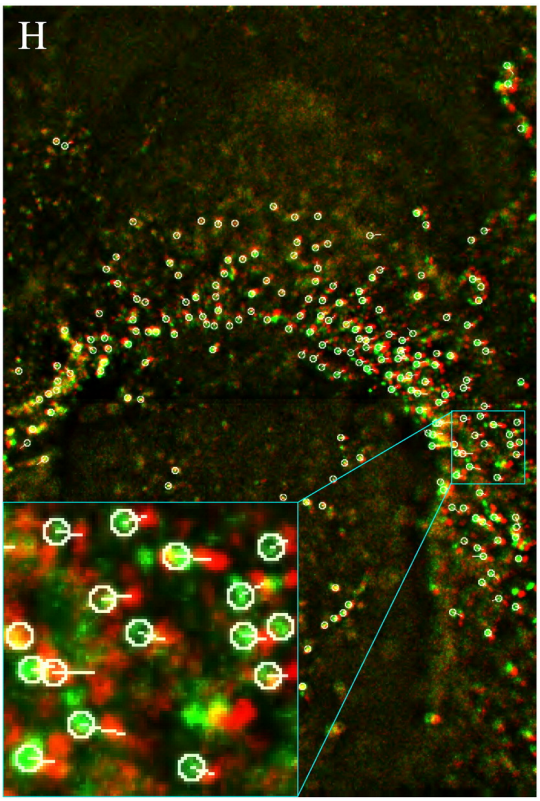

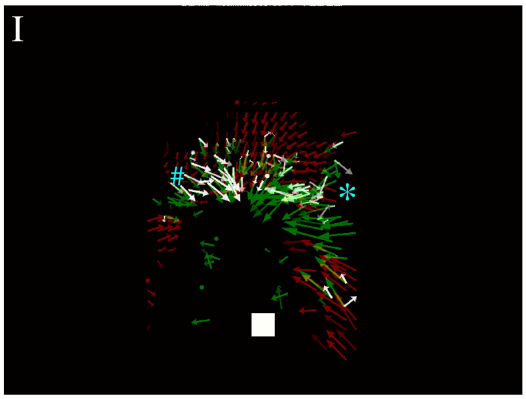

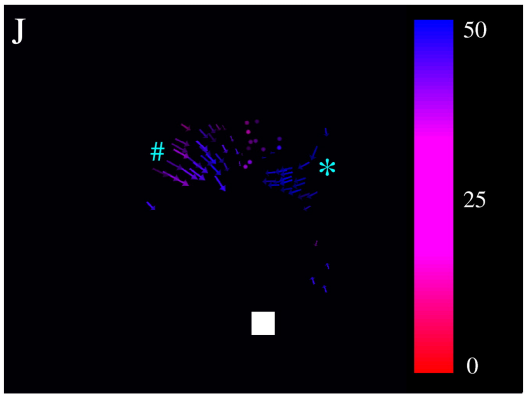

Figure S2.3. Fluorescently labeled human fibronectin incorporates into the quail fibronectin network and participates in tissue displacements.

Fluorophore-conjugated human fibronectin (green) was injected into the LPM at the embryonic left (observer's right) side of a HH6 quail embryo (A). The site of injection is demarcated with the rectangle and shown in higher magnification in (C). A 10-fold higher amount of fluorescent BSA (green) was injected at the embryonic right (observer's left) side. The endogenous fibronectin network was immunolabeled by B3D6 antibody (red). Images in (B) were taken 7 hours after injection. Note the characteristic network-like arrangement of exogenous (green) fibronectin that undergoes deformations and displacements concomitantly with the endogenous quail ECM. BSA did not form any pattern upon injection, and was not detected in the embryo after 7 hours. Scale bars — 100 μm.

Figure S2.3

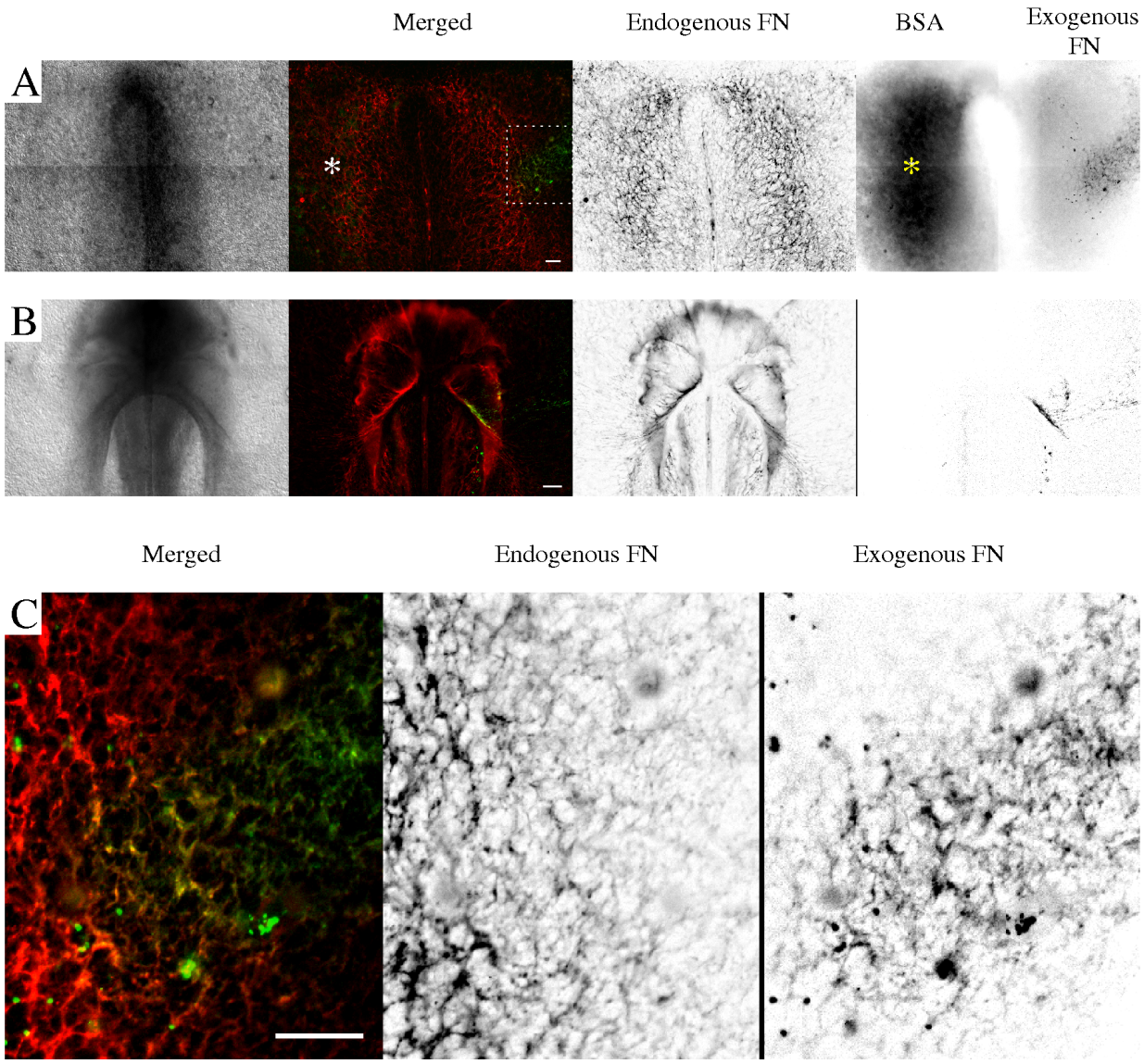
Merged
Endogenous FN
BSA
Exogenous FN
A
B
Merged
Endogenous FN
Exogenous FN
C

Figure S2.4. Exogenous fibronectin can incorporate into both myocardial and endocardial sides of the cardiac jelly when delivered in large quantities.

The anterior lateral plate mesoderm of a quail embryo was injected with 200-250 ng of fluorescent human fibronectin at HH7. After fixation at HH11, 10 μm transverse cryosections were prepared. A-C are transverse sections through the heart tube at the levels schematically shown in D. The immunolabeled endogenous fibronectin is shown as green (right panels of A-C). The exogenous fibronectin (red) is associated with both myocardial (asterisks) and endocardial cell layers. e: endocardium, m: myocardium, cj: cardiac jelly. Scale bars – 40 μm. (D) is modified from Lillie, 1930.

Figure S2.4

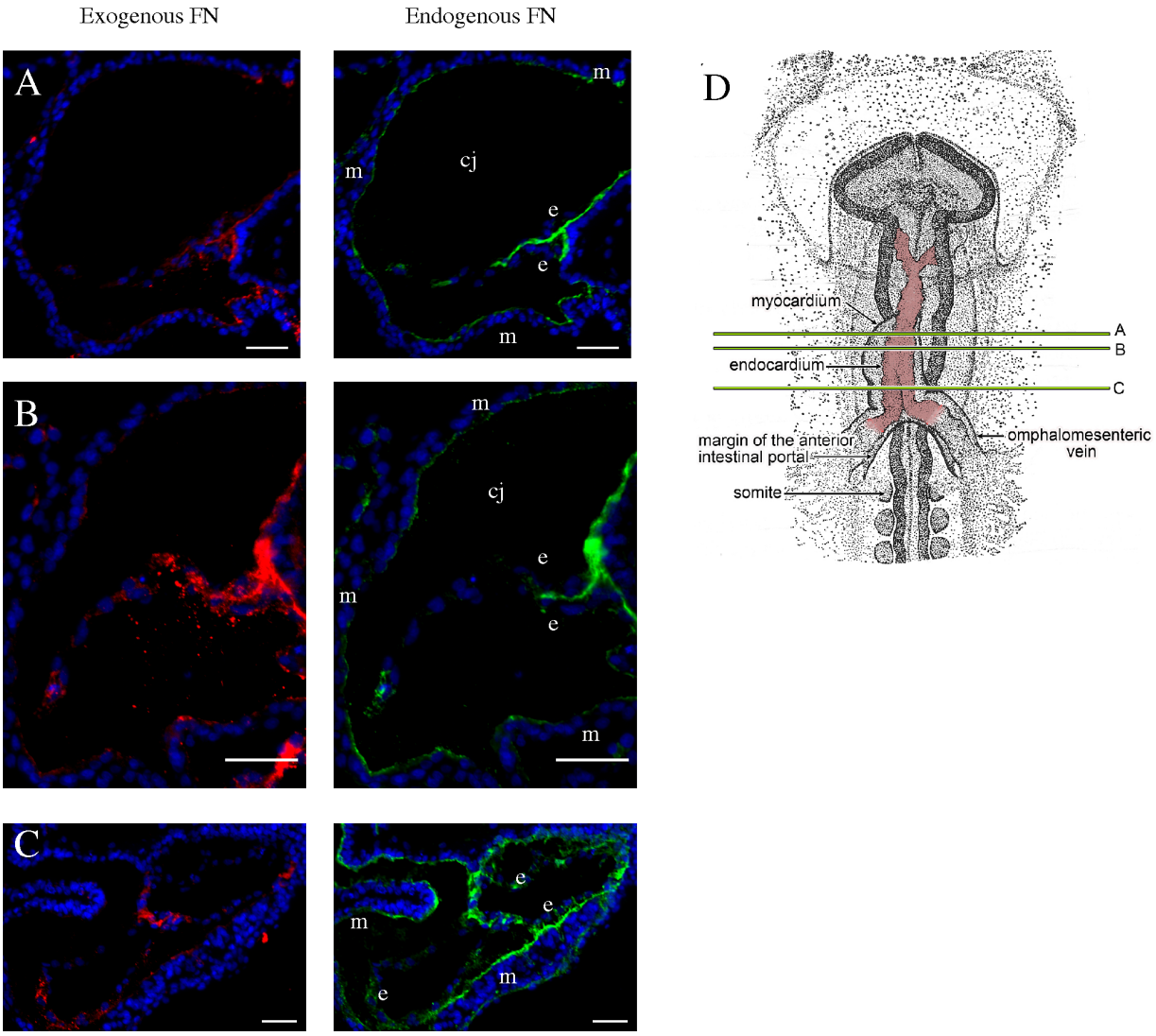
Exogenous FN
Endogenous FN
A
B
C
D
m
cj
e
myocardium
endocardium
margin of the anterior intestinal portal
somite
omphalomesenteric vein

Figure S2.5. Stages of endocardial morphogenesis between HH8- (ES1) and HH11 (ES7).

Left panels show DIC images, the second column contains epifluorescence images with ECM (fibronectin or fibrillin-2) in red and nuclei of endothelial/endocardial cells in green. The third panel (derived from PIV data) demonstrates corresponding cell (green) and ECM (red) movements within selected frontal planes as vectors extrapolating displacements for a 1h time period. The reliability of the vectors is estimated by the contrast of the local fluorescence, and indicated as color brightness. The locally prevalent direction and speed of active cell movements was determined by averaging within a radius of 100 μm the vectors of active cell velocities. These vectors, projected to a frontal plane, are shown in panel 4, and thus represent the local directional bias of active cell movements. The color assigned to the vectors indicates the local standard deviation of active cell movements: blue and red colors indicate locally ordered and disordered movements, respectively (see Fig. 2.7 and Supplement Fig. 2.2J). Notice the tendency to move towards the heart in the vicinity of the forming heart tube (asterisks). HF - headfold, AIP - anterior intestinal portal, NC - notochord, VV - vitelline (omphalomesenteric) veins, HT - heart tube, DA - dorsal aortae. Scale bars - 100 μm.

Figure S2.5A

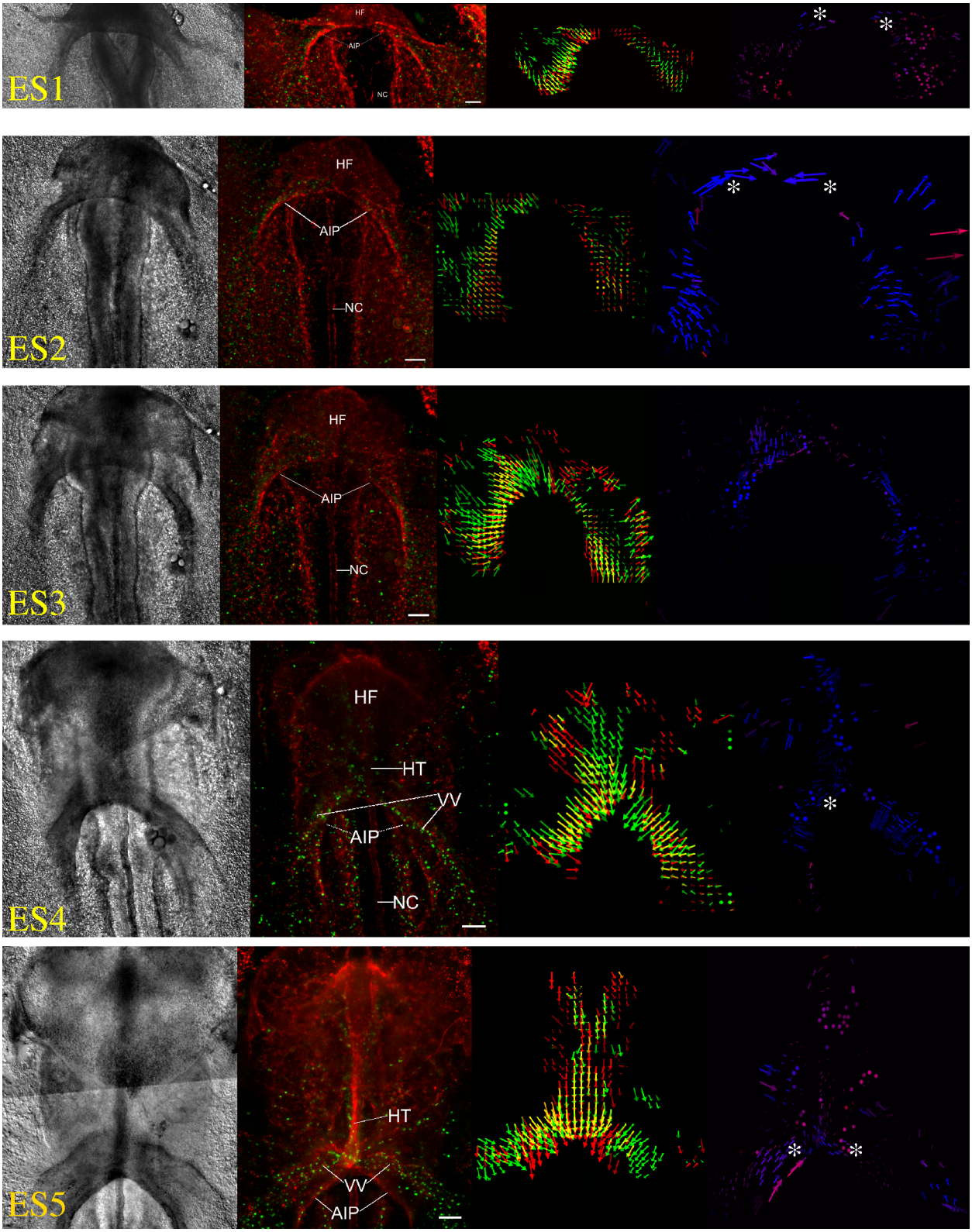
ES1
HF
AIP
NC
ES2
HF
AIP
NC
ES3
HF
AIP
NC
ES4
HF
HT
VV
AIP
NC
ES5
HT
VV
AIP

Figure S2.5B

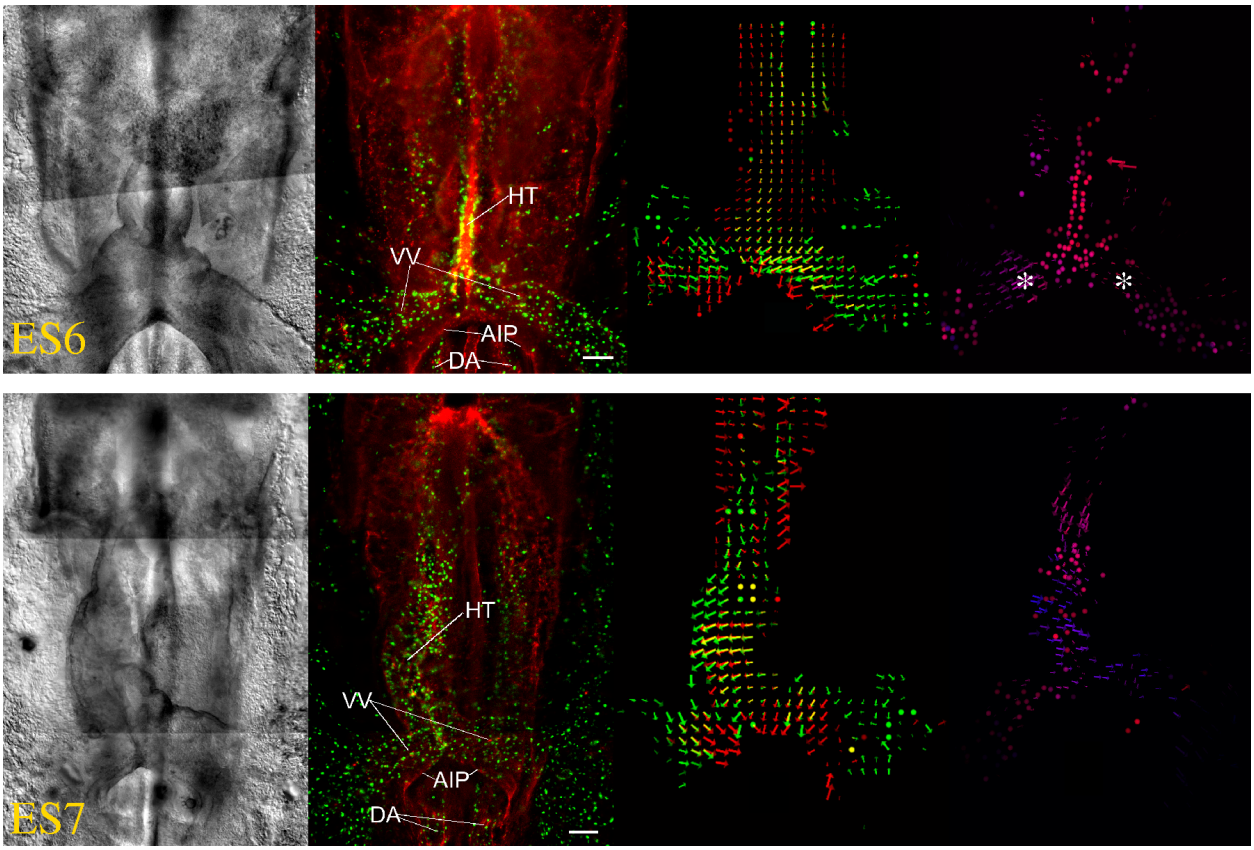

Figure S2.6. An extensive vascular plexus is flanking the forming heart tube at HH10 and later.

DIC (A) and epifluorescence (B) image of a Tie1::H2B-YFP transgenic embryo at HH11. Panel C represents a magnified region delineated with a rectangle in (B). Note a large number of endothelial/endocardial progenitors located ventrally to the foregut: a population that engages in movement towards the anterior heart tube at the same time as similarly positioned ECM fibrils do (Fig. 3). Scale bars — 100 μm.

Figure S2.6.

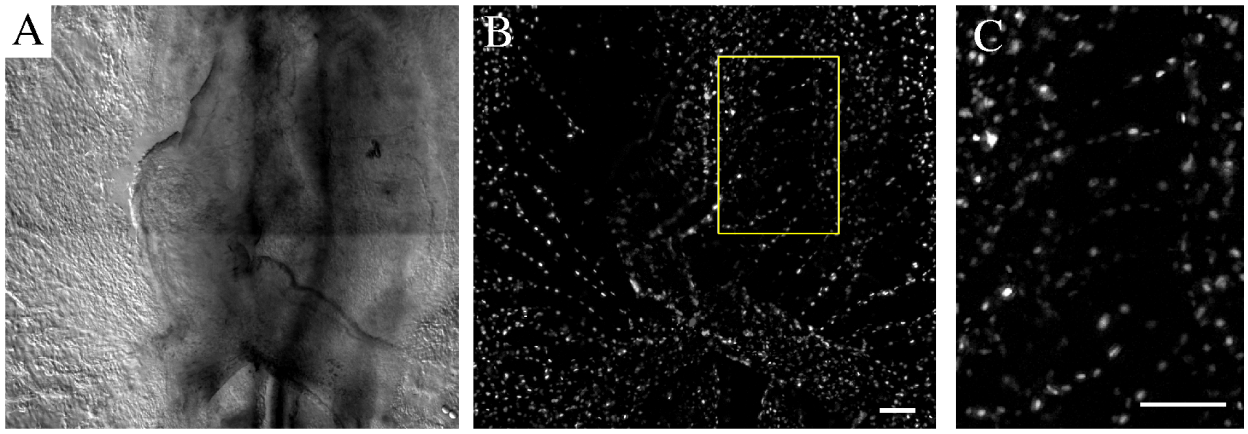

CHAPTER THREE:

Coordinated deformation of myocardial progenitor fields precedes their fusion at the midline, and contributes to the heart tube formation

Abstract

Development of a contractile layer of the heart, the myocardium, involves the movement of bilateral progenitor fields to the embryonic midline. The driving forces for this antero-medial movement have been researched and debated for almost a century. In the current study, we demonstrate that myocardial progenitor fields undergo a series of coordinated deformations that are able to propel their displacements in the anterior direction. These deformations are independent of the endoderm folding during foregut formation, which drives the medial component of the myocardial displacement. Collectively, these two events contribute to the displacement of myocardial primordia to the site of heart tube assembly. By co-labeling myocardial progenitors with either fibronectin ECM or the endoderm in live quail embryos, we demonstrate that motion of all three components to the midline is largely coordinated during heart tube assembly stages. At the same time, myocardial cells demonstrate distinct anterior-directed movement relative to the endoderm. We describe cell rearrangements at the medial myocardial field edge that mediate its contraction (shortening). Based on the results of mechanical perturbations that remove the constraining influences of the surrounding tissues on the heart fields, and computational modeling, we propose that uniform deformation (curling) of the myocardial sheet can drive the anterior-directed movement of the heart fields. The same activity in the context of the surrounding mesoderm also explains the observed c-shaped folding of the myocardium in the dorsal direction (a feature that naturally develops within the cardiogenic mesoderm in caudal to cranial

progression; van den Berg et al., 2009; Abu-Issa and Kirby, 2008).

We conclude that antero-medially directed movement of cardiac progenitor fields to the site of tubular heart assembly relies on a coordinated influence from: 1) endoderm folding and foregut elongation that drive the convergence at the midline, and 2) deformations intrinsic to the myocardial primordia that mediate apparent movement in the anterior direction, and reposition the myocardia along the dorso-ventral embryonic axis, to achieve the optimal orientation for their fusion at the midline. Finally, in contrast to previous suggestions, we see little evidence of active (relative to the ECM) migration of myocardial cells in avian embryos.

Introduction

Early formation of a vertebrate heart includes a sequence of carefully timed and regulated cell movements. In chick, cardiac progenitors (including both endocardial and myocardial precursors) are among the first to ingress through the primitive streak during gastrulation. From the primitive streak pre-cardiac cells travel to the anterior lateral plate mesoderm, where they organize into the bilateral cardiogenic, or heart, fields. Later, the two heart fields translocate to the embryonic midline and fuse to give rise to the tubular heart (reviewed in Fishman and Chien, 1997; Opitz and Clark, 2000; Abu-Issa and Kirby, 2007). In avians and mammals convergence of cardiac progenitor fields at the midline occurs in a very morphologically complex tissue environment. Firstly, the developing heart tube in these organisms is physically linked to the forming foregut via a mesentery. The foregut is lined by endoderm, which forms through three-dimensional tissue folding, followed by rapid elongation (Stalsberg and DeHaan, 1968, Varner et al., 2012). Mechanisms of foregut formation, and the positional relationship between the developing foregut and heart in zebrafish and *Xenopus* differ from those in avians and mammals (Wallace and Pack, 2003; Reed et al., 2009; Spence et al., 2011).

Secondly, throughout their movement to the embryonic midline, myocardial progenitors remain incorporated into a cohesive epithelial sheet, continuous with the adjacent splanchnic mesoderm that will form the muscular wall of the foregut (Bellairs and Osmond, 2005). Integrity of epithelial organization (maintained through interactions with fibronectin ECM) was shown to be critically important for myocardial movements (Trinh and Stainier, 2004). Several studies proposed that myocardial progenitors

actively propel the midline-directed movement of cardiogenic fields (DeHaan, 1963; Rosenquist and DeHaan, 1966; Wiens 1996). Myocardial migration was suggested to be a major force for heart tube assembly; occuring relative to the underlying endoderm of the foregut, with fibronectin as a possible source of the directional information (Linask and Lash, 1986; Linask and Lash, 1988a; Linask and Lash, 1988b).

Recently, Varner et al. (2012) challenged this view by providing evidence for a primary role of endoderm contraction in driving convergence of heart fields at the midline. These authors, however, did not exclude the possibility that myocardial progenitors may play a role in this process, in addition to or parallel to that of the endoderm. Therefore, the extent to which myocardial progenitors are involved in mediating their relocation to the site of tubular heart assembly remains to be determined. Also, very little is known of individual cell behaviors of differentiating myocardial cells within the progenitor field en route to the embryonic midline.

In the current study, we demonstrate that myocardial progenitor fields undergo a series of coordinated deformations that are able to propel their displacements in the anterior direction. These deformations are independent of endoderm folding during foregut formation, however both contribute to the displacement of myocardial primordia to the site of heart tube assembly. By co-labeling myocardial progenitors and fibronectin ECM or the endoderm in live quail embryos, and employing a particle image velocimetry (PIV)-based motion analysis algorithm (Aleksandrova et al., 2012), we demonstrate that motion of all three components to the midline is largely coordinated in HH8-9 quail embryos. At the same time, myocardial cells demonstrate anterior-directed movement

relative to both substrata. We describe cell rearrangements and shape changes that occur at the medial edge of the myocardial field and mediate its contraction. Using mechanical perturbations to remove the constraining influences of the surrounding tissue, we demonstrate that isotropic deformation (curling) of the myocardial sheet in a dorsal direction (a feature that naturally develops within the cardiogenic mesoderm in caudal to cranial progression; van den Berg et al., 2009; Abu-Issa and Kirby, 2008) can drive the movement of the myocardial field forward past the incision site. We use computational modeling to confirm that folding of the myocardial sheet in a ventral direction in combination with its contraction along the medial edge can reproduce the behavior of myocardial progenitor fields during normal cardiogenesis, as well as in mechanically perturbed states. Finally, using pharmacological inhibitors, we compare the sensitivity of endodermal and myocardial tissue contractility to perturbation of the actin cytoskeleton, cell proliferation, Rho kinase (ROCK) signaling and focal adhesion kinase function.

We conclude that antero-medially directed movement of cardiac progenitor fields to the site of tubular heart assembly relies on a coordinated influence from: 1) endoderm folding and foregut elongation that drive the convergence at the midline, and 2) deformations intrinsic to the myocardial primordia that mediate apparent movement in the anterior direction, and reposition the myocardia along the dorso-ventral embryonic axis, to achieve the optimal orientation for their fusion at the midline.

Experimental Procedures

Quail embryo preparation

Fertile wild type quail (*Coturnix coturnix japonica*) eggs (Ozark Egg Co., Stover, MO) were incubated for varying periods of time (from 20 to 36 h) at 37°C to reach stages HH6 to HH11 (Hamburger and Hamilton, 1951). Embryos were then isolated and cultured as in Cui et al., 2009 (modified EC culture; Chapman et al., 2001).

Plasmid generation and transfection for myocardial progenitor labeling

Genomic DNA was prepared from three HH12 chick embryos using Tri Reagent (Sigma) according to the manufacturer's instructions. Primer sequences 5'- AAAAAATTAATCAAGGCTATGACTGCTGGAGTG-3' and 5'-AAAAAGCTAGCCAGAGGTGCTGGTGGTGCTG-3' were used to PCR amplify the region between -931 and +56 of Cardiac Myosin Light Chain 2 (CMLC2) gene. This region was defined based on significant sequence and regulatory element position correspondence to the well-characterized CMLC2 promoter in zebrafish (Huang et al., 2003). To generate pCMLC2::EGFP plasmid, CMLC2 promoter was subcloned into pEGFP-C1 vector (Clontech) between *AseI* and *NheI* restriction sites in place of the CMV promoter. To generate pCMLC2::MitoRFP, CMLC2 promoter was similarly subcloned into pEGFP-N1 vector (Clontech) between *AseI* and *NheI* sites. Then, EGFP

ORF was replaced by the cassette consisting of a mitochondrial localization signal fused to RFP (MitoRFP) using *XhoI* and *NheI* restriction sites. MitoRFP cassette was derived from pCoxIV-RFP (a generous gift from Dr. Rusty Lansford, University of Southern California). To generate constructs for myocardial-specific expression of constitutively active (caRho) and dominant negative (dnRho) variants of RhoA we placed chicken CMLC2 promoter to substitute for the original chicken beta-actin promoter into RhoA-CA and RhoA-DN constructs described in Rupp and Kulesa, 2007 (plasmids were a kind gift from Dr. Paul Kulesa's laboratory). CMLC2 promoter sequences were obtained by PCR amplification from pCMLC2::mito-RFP plasmid using primers 5'-AAAAAATTAATCAAGGCTATGACTGCTGGAGTG-3' and 5'-AAAAAGCTAGCCAGAGGTGCTGGTGGTGCTG-3'. PCR product was digested with AseI/NheI and cloned into the corresponding restriction sites of the RhoA-CA and RhoA-DN constructs.

For transfection, plasmid DNA was delivered into the sub-endodermal space of HH6 quail embryos in complex with Lipofectamine 2000 (Invitrogen) by microinjection using a PLI-100 (Harvard Instruments) apparatus. Embryos were incubated at 37°C until the fluorescent signal from reporter expression became detectable, usually 4-5 h.

Immunofluorescent labeling of ECM *in vivo*

Monoclonal antibodies directed against fibrillin-2 and fibronectin ECM proteins (JB3, B3D6; Rongish et al., 1998, Czirok et al., 2006; DSHB, Iowa City, IA) or a quail

endothelial cell surface marker (QH1; Pardanaud et al., 1987; DSHB) were directly conjugated to AlexaFluor 488, 555 or 647 (Molecular Probes) according to the manufacturer's instructions. The direct conjugates were injected into the lateral plate mesoderm as 5-40 nl boluses using a PLI-100 (Harvard Instruments) microinjector as described in Little and Drake, 2000. Microinjections were performed 30-60 minutes prior to the beginning of the image acquisition to allow for antibody diffusion and antigen binding.

Endoderm labeling *in vivo*

MitoTracker® Green FM dye (Invitrogen) was diluted in DMSO to 1 mM concentration according to the manufacturer's recommendations. Obtained stock solution was further dissolved to 500 nM in PBS. HH8 embryos, placed on paper rings as described above, were submerged into the resultant solution with ventral side down, and placed into a humidified incubator at 37°C for 30 min. Following three 5 min washes with PBS at room temperature, the quality of labeling and integrity of the endoderm in each embryo was assessed under a Leica DM6000 epifluorescent microscope.

Wide-field time-lapse imaging

Automated microscopy of immunolabeled quail embryos was performed as described elsewhere (Czirok et al., 2002; Zamir et al., 2008). To enhance contrast, selected epifluorescence image stacks were deconvolved by a commercial, blind adaptive deconvolution software (Autoquant X, MediaCybernetics). Manual tracing of image details was performed using custom software (see, e.g., Czirok et al., 2004).

Post-fixation immunofluorescence labeling

Embryos were fixed and prepared for immunolabeling according to Little and Drake, 2000. Monoclonal antibodies against avian epitopes (JB3, B3D6, QH1; DSHB, Iowa City, IA), directly conjugated to AlexaFluor 488, 555 or 647, were added at 1:1000 dilutions; rabbit polyclonal anti-GFP antibody, conjugated to AlexaFluor 488 (Molecular Probes, Eugene, OR) – at 1:400, and mouse monoclonal antibody MF20 (DSHB, Iowa City, IA) – at 1:10 dilution in 3% BSA for overnight incubation. Goat anti-mouse secondary antibodies, conjugated to AlexaFluor 488, 555 or 647 (Molecular Probes, Eugene, OR), were used to follow the MF20 staining at 1:10 dilution in 3% BSA. Nuclei were counterstained with 4′,6-diamidino-2-phenylindole (DAPI) at 500 nM in PBS.

Confocal imaging

Confocal imaging of whole-mount embryo specimens was performed using a Nikon 90i upright microscope with a Nikon C1 confocal scan head and Nikon Plan Apochromat 10x and 20x objectives.

Preparation of transverse plastic sections

Embryos were dehydrated through the graded ethanol series, placed in JB4

infiltration medium (Electron Microscopy Sciences, Hatfield, PA) at 4ºC overnight, and embedded in JB-4 resin following manufacturer's protocol. Subsequently, 10µm sections were prepared.

Pharmacological inhibitor treatments

The following inhibitors were used in this study: Cytochalasin D (actin polymerization inhibitor; Sigma), Y27632 (ROCK inhibitor; Sigma), PF 573228 (FAK inhibitor; Tocris Bioscience), Mitomycin C (DNA cross-linking agent; Sigma). Stock solutions were prepared at 10-100 mM concentrations in DMSO or ddH_2O following manufacturer's instructions for each reagent. Stock solutions were then diluted in PBS to 10 μM – 1mM working concentrations as specified in the *Results* section for each experiment. 20-30 μl of reagent solutions or solvent controls were delivered by pipetting to the ventral surface of embryos in EC culture.

Microincisions

50 – 800 μm cuts through the endoderm and adjacent splanchnic mesoderm of HH8 embryos were performed under a Leica stereomicroscope using tungsten needles. Embryos were then incubated at 37ºC on a microscope stage (Czirok et al., 2002; Zamir, et al., 2008) for 0.5 – 1.5 h prior to initiation of time-lapse image acquisition.

Particle Image Velocimetry (PIV) analysis

We used the two step algorithm of Zamir et al., 2005; implemented in MatLab (Mathworks, Inc.) and as described in Aleksandrova et al., 2012. Briefly, images were divided into overlapping tiles, each 75 μm wide. The displacements of the tiles were determined by cross-correlation analysis; for each tile we searched the next image for the location that exhibited the most similar intensity pattern. The resulting displacement vectors were then interpolated and denoised by a thin-plate spline fit, yielding our coarse displacement map. This map was used to construct a second, higher resolution one. The cross-correlation procedure was repeated with tiles that were only 30 μm wide. To reduce ambiguities associated with smaller tiles (patterns within smaller tiles are less unique), the subsequent image was scanned only in the vicinity of positions predicted by the coarse map. In this study we did not apply a final smoothing (spline fitting) step, but kept the results of the second cross-correlation analysis.

Within the whole embryo, the ECM label was highly non-uniform, as some areas were exposed to more antibody than others. Image tiles corresponding to areas where the immunofluorescence was weak are very noisy; hence the cross correlation analysis was more error-prone. To reflect this, for each PIV-derived displacement vector we assigned a weight, the local standard deviation of fluorescence intensity. Thus, displacement vectors characterizing a detail-rich region carry more weight in the subsequent analyses than those obtained in a weakly-labeled area.

The PIV comparing displacements of the endoderm and myocardial progenitors has been performed by identical methods. However, the images of the MitoTracker-mediated labeled endoderm were not suitable for deconvolution. Hence, we projected the maximal image intensities of the 'z-stack' into a single image for each frame, and used the resulting 'z-projected' image for PIV analysis. Thus, instead of performing the PIV analysis on each collected z-plane, it was performed only at a single collapsed image. To compare endoderm and myocardial movements, both optical channels were analyzed the same way.

Motion analysis

To characterize ECM and cell rearrangements at various stages of heart development, pairs of deconvolved image stacks were selected. The images within the stacks were taken 20 minutes apart. A given pair, *P*, was analyzed through the following procedure. By manual masking, two additional image stack pairs were derived: one containing the forming heart, the other the somites or the pre-somitic mesoderm (to be used as a reference). The corresponding optical sections and fluorescence channels were compared by PIV analysis as described above. Velocities (displacements normalized by the time lag between the images of P) were presented in a reference system co-moving with the somites. Thus, we use the term “velocity” to describe a vector-value characterizing both the rate and direction of the displacements of selected objects. The term “speed” is used to describe the magnitude of the velocity vector.

Active cell velocities (Aleksandrova et al., 2012) were calculated as the local vectorial difference between the cell- and ECM-derived velocity vectors (Aleksandrova et al., 2012). The “reliability” weight assigned to the vectorial difference is the lesser of the two weights assigned to the vectors. For statistical comparison of embryos, certain areas were selected around the anterior intestinal portal (AIP). Velocity vectors from different embryos, but within the same location, were pooled. Data obtained from different embryos were considered statistically independent.

Computational modeling

Modeling biological pattern formation typically involves the use of partial differential equations (PDE), which offer a well-respected way to represent tissue mechanical quantities such as stresses and strains. The use of PDEs in simple systems allows full analytical solution, i.e., predicting model behavior for arbitrary parameter choices. Individual cell activity, however, is not resolved using a PDE approach. In order to connect cellular-scale activities, such as active “intercalation” or collective migration, directly to organ pattern formation it is necessary to model individual cells and then reconcile these data with tissue scale behavior. Thus, we make a connection between cellular events and the next larger scale of biological organization.

Presently, the most widely used models of morphogenesis represent cell-cell adhesive interactions as "fluid" droplets; for example, the cellular Potts model and its grid-free version, the Subcellular element model. These model choices are motivated by the non-Newtonian fluid-like behavior of simple cell aggregates. Such cell-based models

have been used to formulate hypotheses for cellular activities, such as chemotactic guidance. While results from these models have been encouraging, in our estimation the available simulations include biomechanical artifacts, which present difficulties, notably, friction against a non-existing (undescribed) frame of reference.

We have developed a substantially modified version of Dr. Timothy Newman's (University of Dundee) subcellular element model, which eliminates some of its mechanical limitations. In our model, the mechanical connectivity of the cells are explicitly represented as elastic beams connecting adjacent particles. The beams, connecting individual cells, can be compressed and stretched, bent and twisted. The great advantage of explicit cell-cell contact representation is that we can formulate plastic stress relaxation by removing and inserting these links, as well as by changing the equilibrium properties of the links.

The mechanical equilibrium of the resulting structure can be calculated by solving the steady state of a coupled Ordinary Differential Equation system. The model will be further refined as information on the mechanical properties of the relevant tissues become available.

Quantitative analysis of the AIP regression and myocardial displacement speeds in control and experimentally treated embryos

To characterize AIP regression, we placed markers at the first somite pair and the anterior most portion of the AIP (illustrated in Fig. 3.11A). The distance between the

center of mass of the somite markers and the marker at the AIP was used as our measure of AIP position. Foregut elongation speeds were defined as the change in the AIP-somite distance. As this speed decreases as development progresses, we distinguished between three phases of foregut elongation. Depending on the AIP-somite distance, we assigned the AIP as early, intermediate and late, when the distance was larger than 600 um, between 300 and 600 um and less than 300 um, respectively.

The significance of observed changes in AIP regression/foregut elongation speeds were established by the following procedure. Each analyzed embryo contributed a single (time-averaged) AIP speed value, in three possible categories: early, intermediate and late (depending on the somite-AIP distance). Data obtained from control and specifically treated samples were pooled, and each resulting data set was compared with the data set obtained from control embryos (untreated embryos, except for the transfected Rho constructs, which were compared with embryos transfected with myocardial-specific GFP constructs). The significance of alteration in sample mean was established using a two-tailed Welch's t-test.

To assess the movements of myocardial cells in embryos perturbed as in Fig. 3.6E, CMLC2::GFP or CMLC2::MitoRFP-expressing cells were tracked manually at the incision boundary (as demonstrated in Fig. 3.11C). To determine the local ECM movement, or that of the wound/incision edge, we implemented the following procedure: i) the center of mass of the tracked cells were calculated at both side of the embryo. Since the tracked cells are in close proximity, the center of mass gives a convenient approximate location of the myocardial cells. ii) Centered around the position of the

center of mass, a PIV cross-correlation calculation was performed on the ECM images, yielding the typical ECM displacements at those areas. As the most prominent feature on these images is the wound edge, the PIV analysis essentially returns the movement of the incision boundary. iii) Knowing the positions of the myocardial cells as well as the incision boundary, their relative speed, v, was calculated for each frame. iv) The autonomous myocardial activity was characterized as the magnitude of v, averaged over 10 frames following experimental perturbation (addition of reagents).

The significance of observed changes in myocardial “curling” activity was established by the following procedure. Each analyzed incision contributed a single (time-averaged) activity value. Data obtained from control and specifically treated samples were pooled, and each resulting data set was compared with the data set obtained from control embryos (subjected to transfection and incisions, but no additional reagents). The significance of alteration in sample mean was established using a two-tailed Welch's t-test.

If the t-test based comparison of measurement results in control and experimentally-treated embryos yielded $p<0.05$, the induced changes in AIP regression speeds or speeds of myocardial displacements at the incision edge for a given reagent were considered significant.

Results

Myocardial progenitors at HH8-11 move relative to the fibronectin ECM, but the speed of this relative ("active") motion is insufficient to account for apparent displacement.

To generate reporter constructs for specific labeling of individual myocardial progenitors within heart fields, we used the region between -931 and +56 of chick Cardiac Myosin Light Chain 2 gene (CMLC2; thereafter referred to as CMLC2 promoter). Constructs mediating CMLC2 promoter-driven expression of GFP and RFP were delivered to quail embryos at HH5-6. According to Goswami et al. (1994), transcription of CMLC2 initiates at HH5 in chick. Fluorescent reporter expression was usually detectable by HH7+ – HH8- (3-4 somites), and found in a representative number of myocardial progenitors by HH8 (5-6 somites) in transfected embryos (Fig.2.1A, top panels). This is in good agreement with results of Han et al. (1992) on timing of sarcomeric myosin assembly.

The appearance and behavior of CMLC2::GFP and CMLC2::mitoRFP-expressing cells were typical of those expected for cells in the myocardial fields they were incorporated in as the former: 1) were distributed throughout the MF20+ myocardial fields, 2) did not differ in morphology from their untransfected neighbors, 3) were positive for sarcomeric myosin heavy chain (MF20; Bader et al., 1982) – a bona fide marker of myocardial differentiation, and 4) were able to proliferate as evidenced by formation of clonal groups and cell division events registered in time lapse sequences (Fig. 3.1A and data not shown).

In some embryos at HH8-9 we observed occasional fluorescent reporter-expressing cells in the splanchnic and somatic mesoderm outside of the continuous heart field. However, by HH11-12 expression of CMLC2 promoter-driven reporters was confined to the heart tube and the mesoderm immediately adjacent to it at its anterior and posterior ends (Fig 3.1A, bottom panels). In all cases we limited our analyses to cells located within crescent-shaped heart fields at HH8 as defined by others (Abu-Issa and Kirby, 2008; van den Berg et al., 2009).

To visualize the fibronectin ECM in the vicinity of myocardial fields, we microinjected fluorescently conjugated antibody B3D6 (DSHB; Little and Drake, 2000), into the sub-endodermal space of CMLC2::EGFP or CMLC2::mitoRFP-transfected quail embryos at HH7-8- (n=21), and recorded their development until HH11-12 in time lapse. Within obtained image sequences, we specified image pairs acquired 18-26 minutes apart from one another. Selected image pairs described progressive stages of myocardial progenitor movement to the midline, and were chosen in a way that allowed direct comparison between movement speeds of myocardial progenitors, measured in the current study, and those of their endocardial counterparts (Aleksandrova et al., 2012). A representative example of an embryo at initial and final stages of development included in the analysis is shown in Fig. 3.1B. In Fig. 3.1C stage 3 corresponds to HH8, stage 4 – to HH8+, stage 5 – to HH9, stage 6 – to HH10, and stage 7 – to HH11. Stages 1 and 2 were omitted from Fig. 3.1C as they described the events at HH7-8-, at which time the number of CMLC2::mitoRFP-expressing cells was insufficient for motion analysis.

Analysis of myocardial progenitor and fibronectin movements was performed using particle image velocimetry (PIV) as described in detail in Aleksandrova et al. (2012). Right panels in Fig. 3.1B show examples of vector maps that represent apparent movements of each component at stage 3 (HH8) and stage 7 (HH11). Values for apparent and active (relative to the ECM) motion speeds of myocardial progenitors are plotted alongside the displacement speed of fibronectin ECM in Fig. 3.1C. For the purposes of comparison Fig. 3.1C also includes information on apparent and active motion speeds of endocardial progenitors, measured in Aleksandrova et al., 2012. To ensure that results of the latter and our current study were directly comparable, three out of twenty one embryos used for PIV analysis were Tie1::H2B-YFP positive to allow for simultaneous visualization and measurements of endocardial, myocardial, and fibronectin movements. Endocardial motion data obtained from these embryos did not differ significantly from those reported in Aleksandrova et al., 2012. Similarly, values for ECM displacement measured in both studies were very similar at all stages (data not shown).

Figure 3.1. Characterization of myocardial progenitor movements relative to the fibronectin ECM:

A - maximum intensity dorso-ventral projections of confocal stacks obtained at HH8 (top panels), and HH11 (bottom panels). Whole mount specimens were immunostained with antibodies MF20 (red), B3D6 anti-fibronectin (blue), and anti-GFP (green) to enhance pCMLC2-GFP expression-mediated labeling of transfected cells. A′, A'' -10 μm plastic section taken at the levels indicated with horizontal white lines. Scale bars: 100 μm

B – representative epifluorescent images of embryos at the first and last stages included in the PIV analysis, with representative vector maps on the right. Red – fibronectin ECM, green – pCMLC2::EGFP-transfected myocardial cells. Scale bar and white squares – 100 μm.

C – mean speeds of apparent and active myocardial progenitor movements, compared to speeds of endocardial and ECM displacements at progressive stages of heart tube assembly.

Figure 3.1A

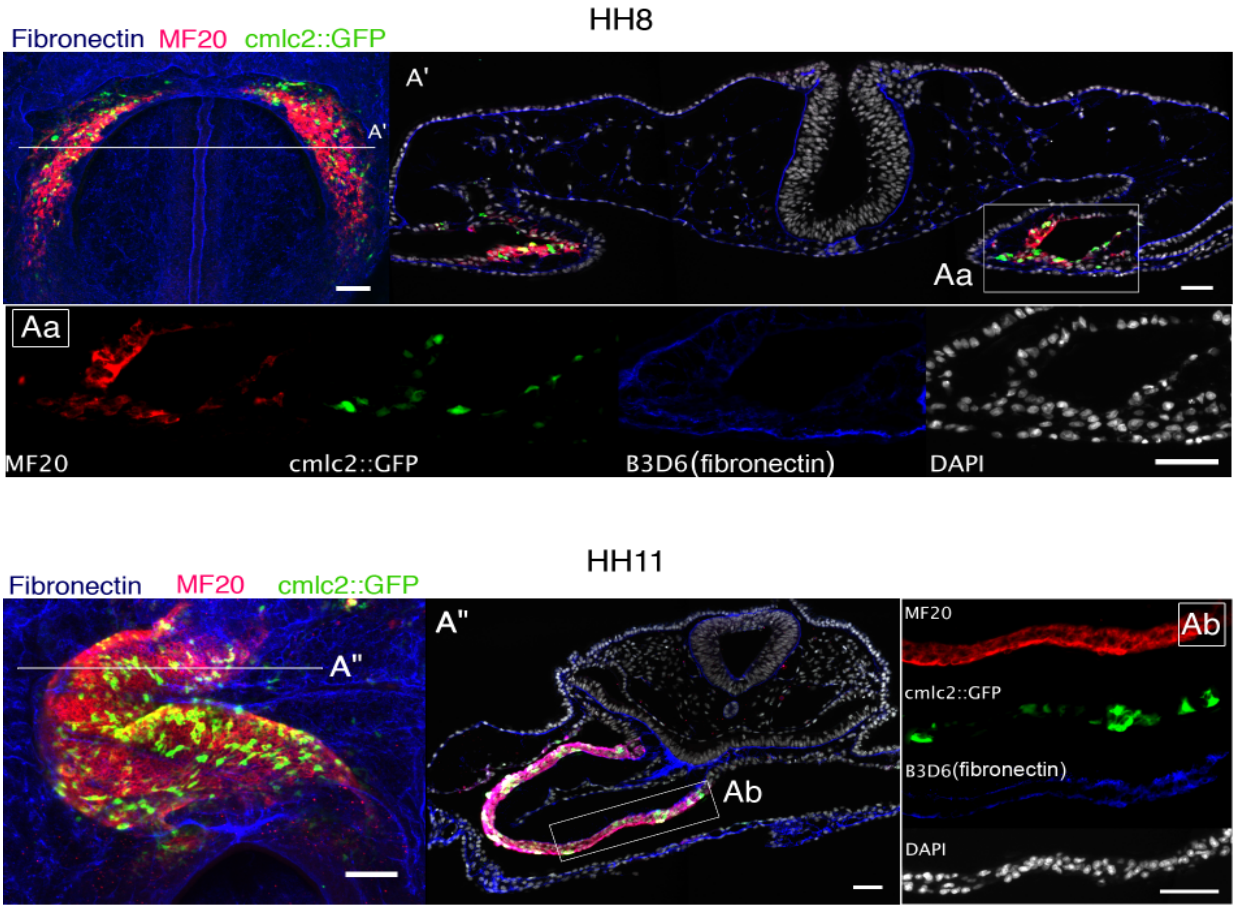
HH8
Fibronectin MF20 cmlc2::GFP
A'
A'
Aa
Aa
MF20
cmlc2::GFP
B3D6(fibronectin)
DAPI
HH11
Fibronectin MF20 cmlc2::GFP
A"
A"
Ab
Ab
MF20
cmlc2::GFP
B3D6(fibronectin)
DAPI

Figure 3.1B, C

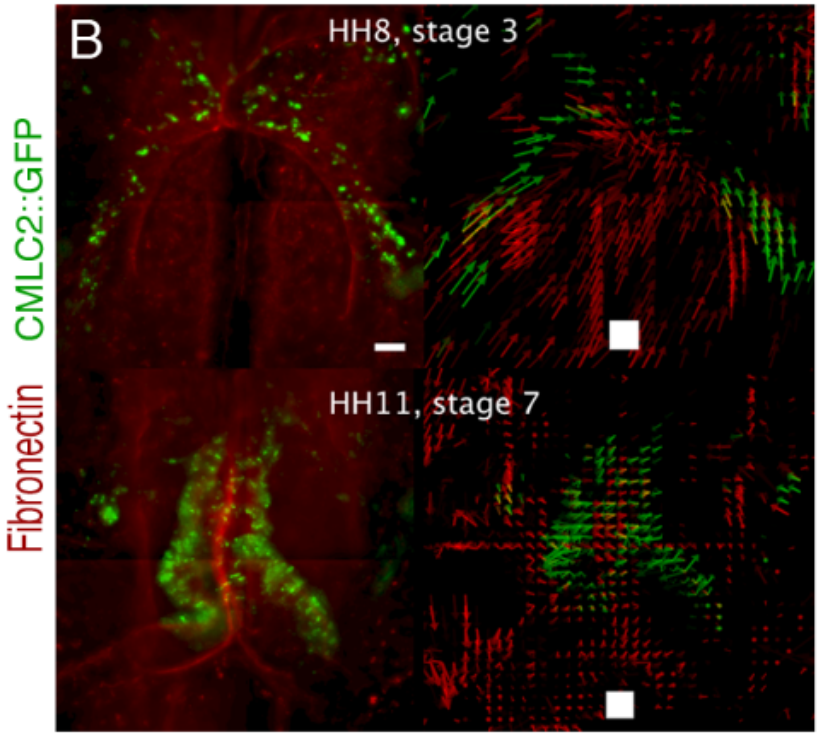
B
HH8, stage 3
HH11, stage 7
CMLC2::GFP
Fibronectin

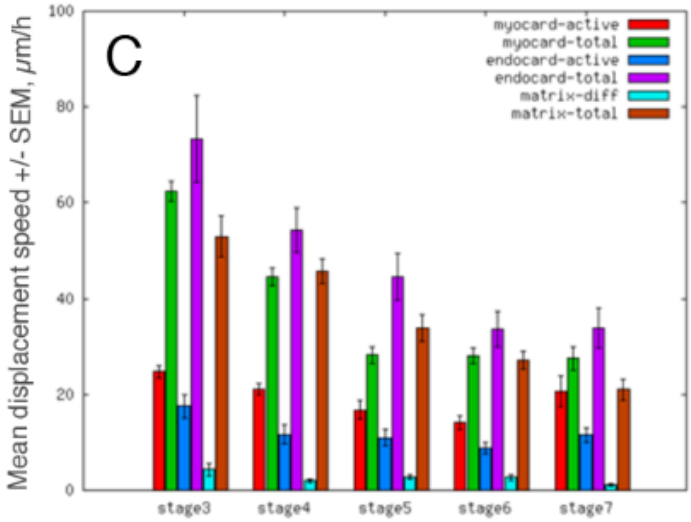
C
myocard-active
myocard-total
endocard-active
endocard-total
matrix-diff
matrix-total
Mean displacement speed +/- SEM, μm/h
0
20
40
60
80
100
stage3
stage4
stage5
stage6
stage7

Analysis of myocardial field movement relative to the underlying endoderm

To achieve endodermal labeling in quail embryos *in vivo*, we used MitoTracker Green dye, which is retained in mitochondria of live cells. An example of a labeled embryo is presented in Fig. 3.2A. As seen in Fig. 3.2A', MitoTracker Green staining allows the discernment of individual cells within the endodermal tissue. In our experiments we found that short exposure of the ventral side of the embryo to the dye solution causes retention of MitoTracker Green only in the endoderm, if its integrity was not compromised during treatment. Embryos transfected with CMLC2::mitoRFP (n=11) were stained with a 350-500 nm solution of MitoTracker Green as described above, at HH8. Subsequently, development of labeled embryos was recorded in time lapse for 4-5 hours with 10-12 min intervals between frames. Unfortunately, fading of MitoTracker Green fluorescent signal prevented further imaging.

In order to compare magnitudes and directions of endodermal and myocardial movements, we selected several image pairs (with images taken 20-24 min apart) for each specimen. Our PIV algorithm was used to generate vector maps such as those represented in Fig. 3.2B. Vectors describing apparent myocardial (red) and endodermal (green) movements were similarly directed towards the ventral midline, indicating that at HH8-9 both tissues move toward the midline in a coordinated fashion. At the same time, motion of the myocardium relative to the endoderm, illustrated with blue vectors in Fig. 3.2B, had a pronounced anterior directionality. Displacement speeds, calculated for the region represented in Fig. 3.2B, are shown in Fig. 3.2C.

Figure 3.2: Analysis of myocardial progenitor movements relative to the endoderm

A, A' – HH8 quail embryo with endoderm labeled with MitoTracker Green dye. Scale bars: A-100 μm, A' – 40 μm ;

B – A representative vector field from PIV analysis of myocardial movement relative to the endoderm. Red vectors correspond to myocardial progenitor displacements, green vectors illustrate movements of the endoderm, and blue vectors show relative movement between the two tissue types. Scale bar: 100 μm.

C – apparent myocardial, apparent endodermal, and active myocardial (relative to the endoderm) displacement speeds, measured for the region outlined in B.

Figure 3.2

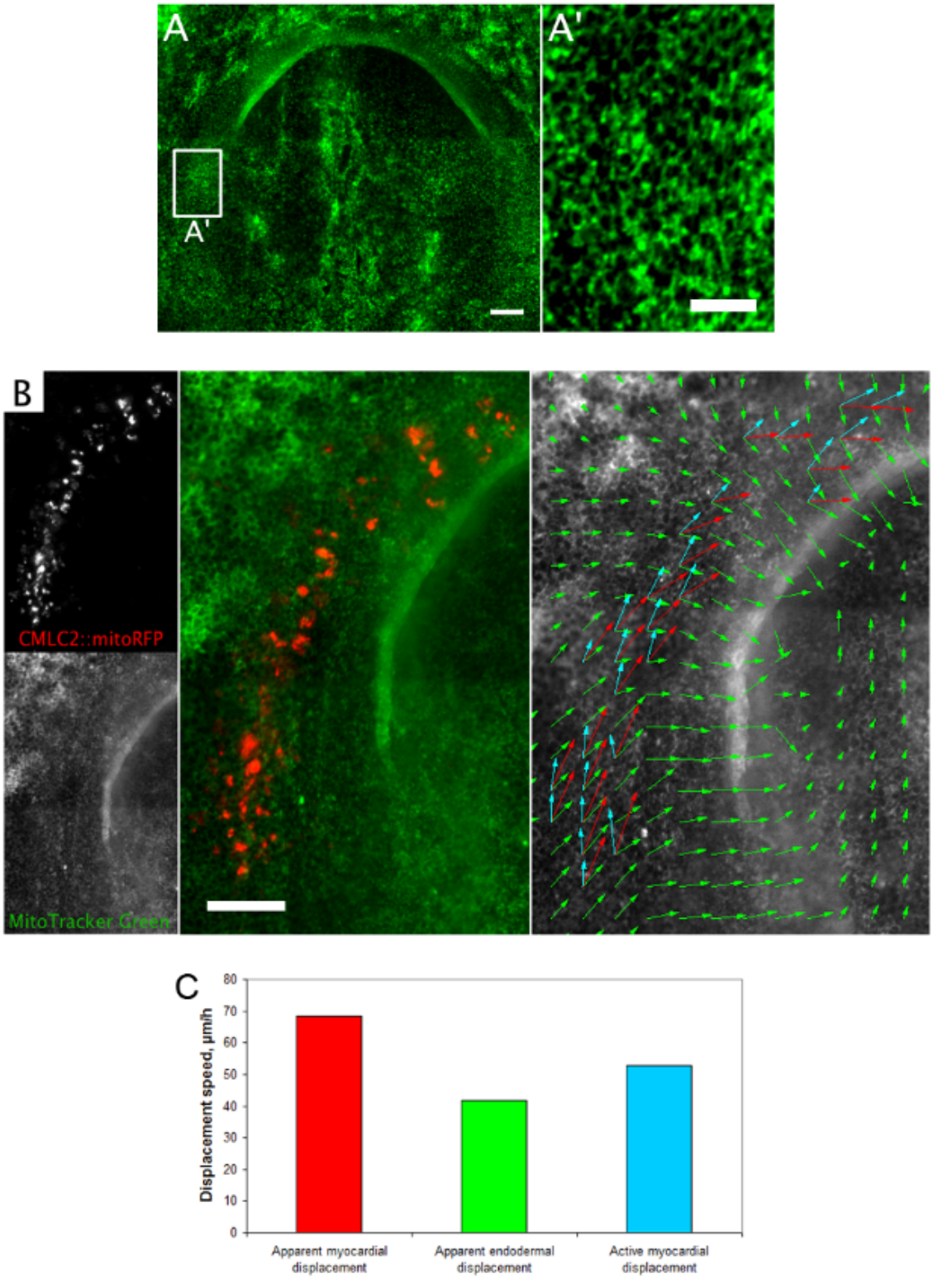
A
A'
A'
B
CMLC2::mitoRFP
MitoTracker Green
C
Displacement speed, µm/h
80
70
60
50
40
30
20
10
0
Apparent myocardial displacement
Apparent endodermal displacement
Active myocardial displacement

Myocardial progenitors and fibronectin ECM-containing fibrils demonstrate differential behaviors at the medial and lateral aspects of the heart field

Next, we set out to investigate the mechanism responsible for the anterior-directed movement of myocardial fields relative to the endoderm. To probe the morphology of heart fields at HH8-9 (a time within the HH8-11 interval when the apparent speed of myocardial progenitor movement is the highest; stages 3-5 in Fig. 3.1C) we performed serial sectioning of embryos (n=4) that were stained with MF20 to visualize myocardial progenitors, and DAPI. Cross-sectional anatomy of MF20+ myocardial fields closely matched that reported by the following 3D reconstruction-based studies. Abu-Issa and Kirby, 2008 used Nkx2.5 expression to visualize myocardial progenitors at HH8-12 for studies of patterning of the heart field. Later, van den Berg et al., 2009 utilized cardiac troponin I as a myocardial marker in their work on cell proliferation within the developing heart.

Abu-Issa and Kirby, 2008 reported that heart fields undergo a 120-130º inversion concomitantly with caudal movement of the AIP. In agreement with their results, we observe the change in positions of myocardial fields relative to the dorso-ventral axis of the embryo at different cranio-caudal levels at HH8-9. Fig. 3.3A' (reproduced from van den Berg et al., 2009) illustrates the overall morphology of cardiogenic fields at HH8, and serves as a reference for the position of individual sections shown in Fig. 3.3B along the cranio-caudal embryonic axis. As seen in Fig. 3.3B, myocardial progenitors (green) are continuous with the splanchnic mesoderm (MF20-negative tissue adjacent to the myocardial progenitors) comprising the ventral coelomic wall in the caudal aspect

of the heart fields. In the more anterior position, orientation of myocardial fields changes to dorso-lateral and, eventually, dorsal at their most cranial aspect (please refer to the provided guide for orientation).

Figure 3.3: Myocardial progenitor fields undergo a dramatic change in position along the dorso-ventral embryonic axis in caudal-to-cranial progression.

A' – a panel from Fig. 3 by van den Berg et al., 2009 (p. 182), illustrating the anatomy of myocardial fields at HH8;

B - a series of 10 μm-thick sections (taken 30-200 μM apart from each other) through the HH8 embryo at the level of the cardiac fields. An approximate position of each section relative to the cranio-caudal axis is indicated by lines connecting to A'. Green – MF20 antibody-labeled myocardial progenitors, blue – DAPI. d – dorsal, and v - ventral side of the embryo. All sections are presented in the same orientation. Scale bar: 100 μm.

Figure 3.3

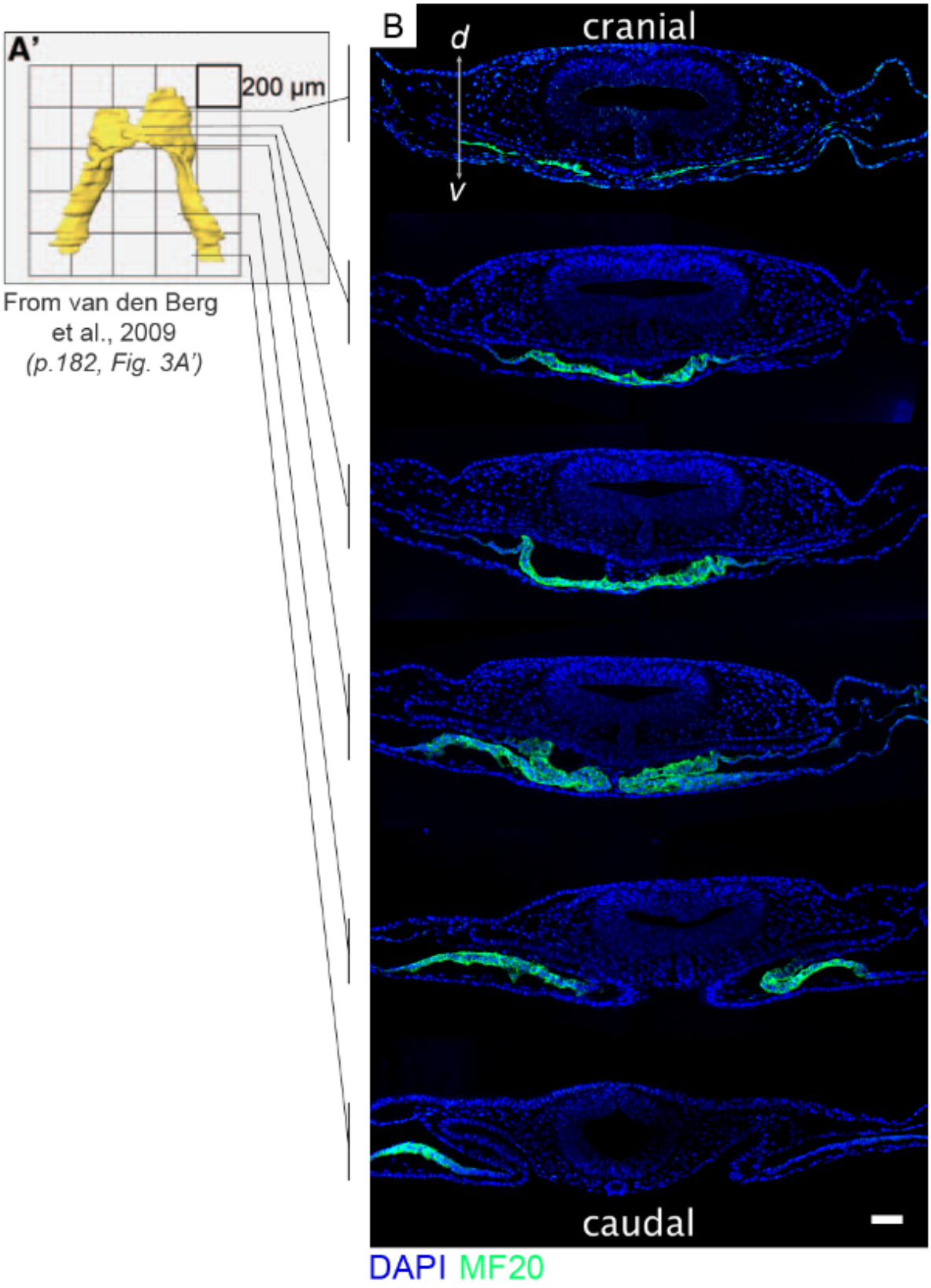
A'
200 µm
From van den Berg et al., 2009
(p.182, Fig. 3A')
B
d
v
cranial
caudal
DAPI MF20

In order to investigate the behavior of individual myocardial progenitors within heart fields at progressive steps of their antero-medial movement, we subjected three HH8 embryos (each expressing CMLC2::GFP in one or both myocardial fields) to time lapse imaging with 60-90 s interval between the consecutive frames. In Fig. 3.4A top panels show DIC, and bottom panels – epifluorescence (GFP) images of the embryonic right myocardial field at progressive time points between HH8 and 9. Epifluorescence images were colorcoded to render ventrally-positioned cells red, those positioned dorsally – blue, with the remaining z-planes acquiring intermediate colors of the spectrum in accordance with their position along the dorso-ventral embryonic axis. Cells along the medial aspect of the heart field undergo pronounced elongation perpendicular to the AIP edge (example cell groups are marked by asterisks Fig. 3.4A). Laterally positioned cells appear to maintain more constant shapes. Simultaneously with cellular elongation at the medial aspect, the lateral edge of the heart field turned ventrally (note the change in color from blue/green in Fig. 3-4Aa to yellow/red portion of the spectrum in Fig. 3-4Ab-c, apparent for the lateral aspect of the myocardial field).

To generate Fig. 3.4B, outlines of CMLC2::EGFP expressing cells from the region marked with brackets in Fig. 3.4A were traced at selected time points using tools of Adobe Photoshop CS4 (Adobe Systems Inc.). Then resultant shapes were plotted against the white background in black for the medial, and in grey – for the lateral aspect of the myocardial field. Outlines of medial cells changed progressively as the latter aligned with their long axes perpendicular to the AIP, and underwent further elongation.

At the same time, most of the lateral cells maintained relatively constant orientations and shapes.

Further, to assess the dynamics of ECM displacements in the vicinity of converging myocardial fields at HH8-9, we used PIV to assess the local differences in movement directionality in individual frames of time-lapse image sequences, where fibronectin or fibrillin-2 ECM was labeled *in vivo* as described above. Four image sequences were analyzed, two each for fibronectin and fibrillin-2. Representative images are shown in Fig. 3.5. There, PIV-derived 20 min displacement trajectories (green) are plotted over the second image in the pair used for analysis. Note that in the vicinity of the AIP (in the area corresponding to the medial edge of the myocardial field) trajectories indicate displacement in the antero-medial direction, whereas in more lateral regions this direction is strictly medial.

Figure 3.4: Medial and lateral compartments of the myocardial field show differential cell behaviors

A – DIC (top panels) and epifluorescence (GFP; bottom panels Aa-Ac) images of the embryonic right myocardial progenitor field in pCMLC2::GFP-transfected embryo. Individual planes within the z-stack were colorcoded to reflect the position of objects along the dorso-ventral embryonic axis as described in the text and illustrated by the provided spectrum bar. Elapsed times from the beginning of image acquisition are shown in the top left corners in Aa-Ac. Scale bar: 100 μm.

B – outlines of the cells within the region demarcated by brackets in Aa, traced and plotted as described in the text. Blue segmented line marks the AIP border. Elapsed times from the beginning of image acquisition are shown in the top left corner of each image.

Figure 3.4

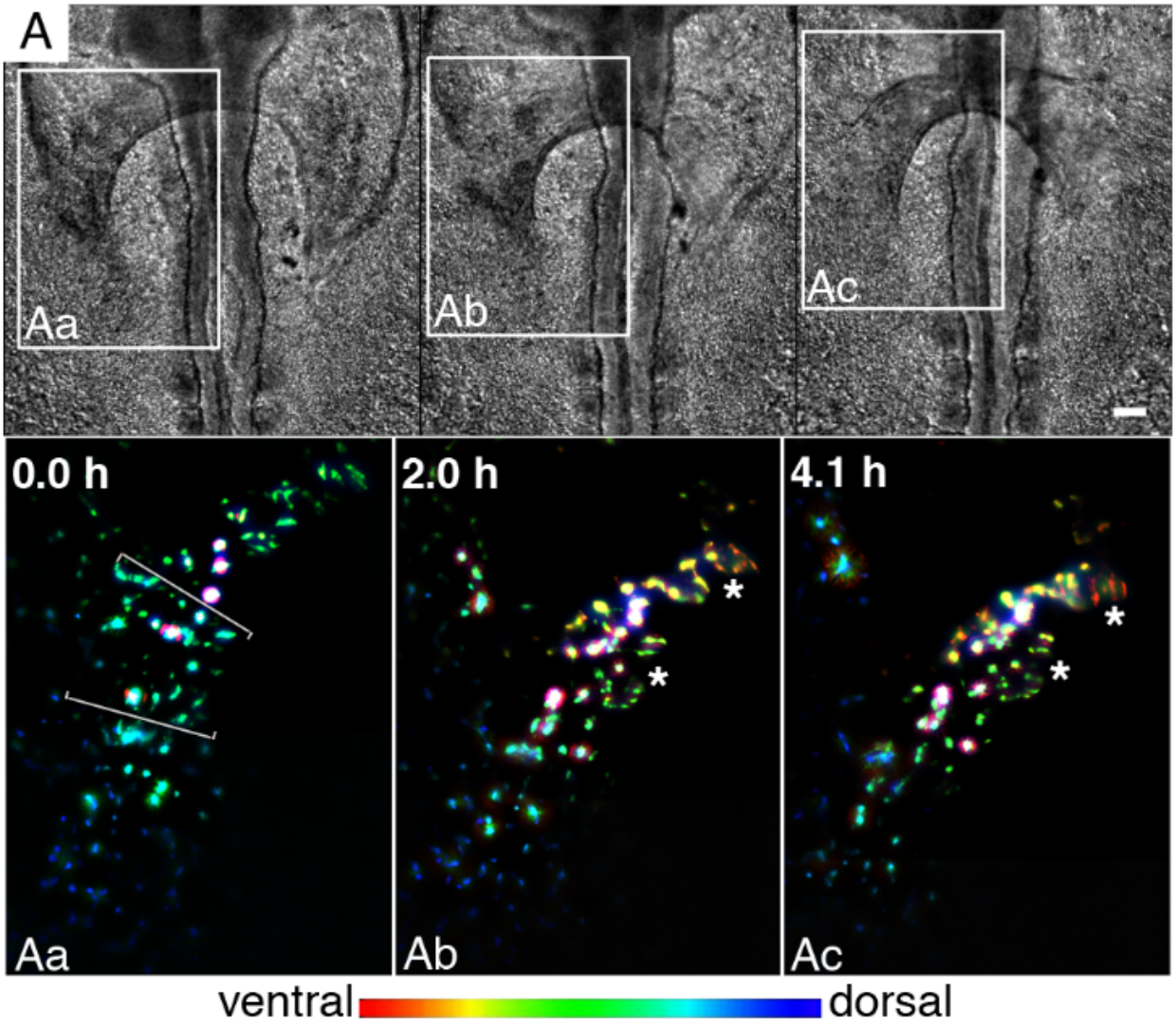

Figure 3.5: Differences in directionalities of fibronectin displacements in the vicinity of the AIP

A – HH8 embryo with *in vivo* labeled fibronectin ECM. Scale bar: 100 μm.

B - PIV was used to trace fibronectin displacements in the vicinity of the AIP. Red dots in the top panel indicate the centers of individual pixel arrays, traced by PIV. Resultant trajectories of ECM displacement during 20 min were plotted over the second image in an analyzed pair (green trajectories; bottom panel). Blue line separates areas with predominantly medial fibronectin displacements from those with prevailing antero-medial fibronectin displacements (illustrated by green arrows).

Figure 3.5

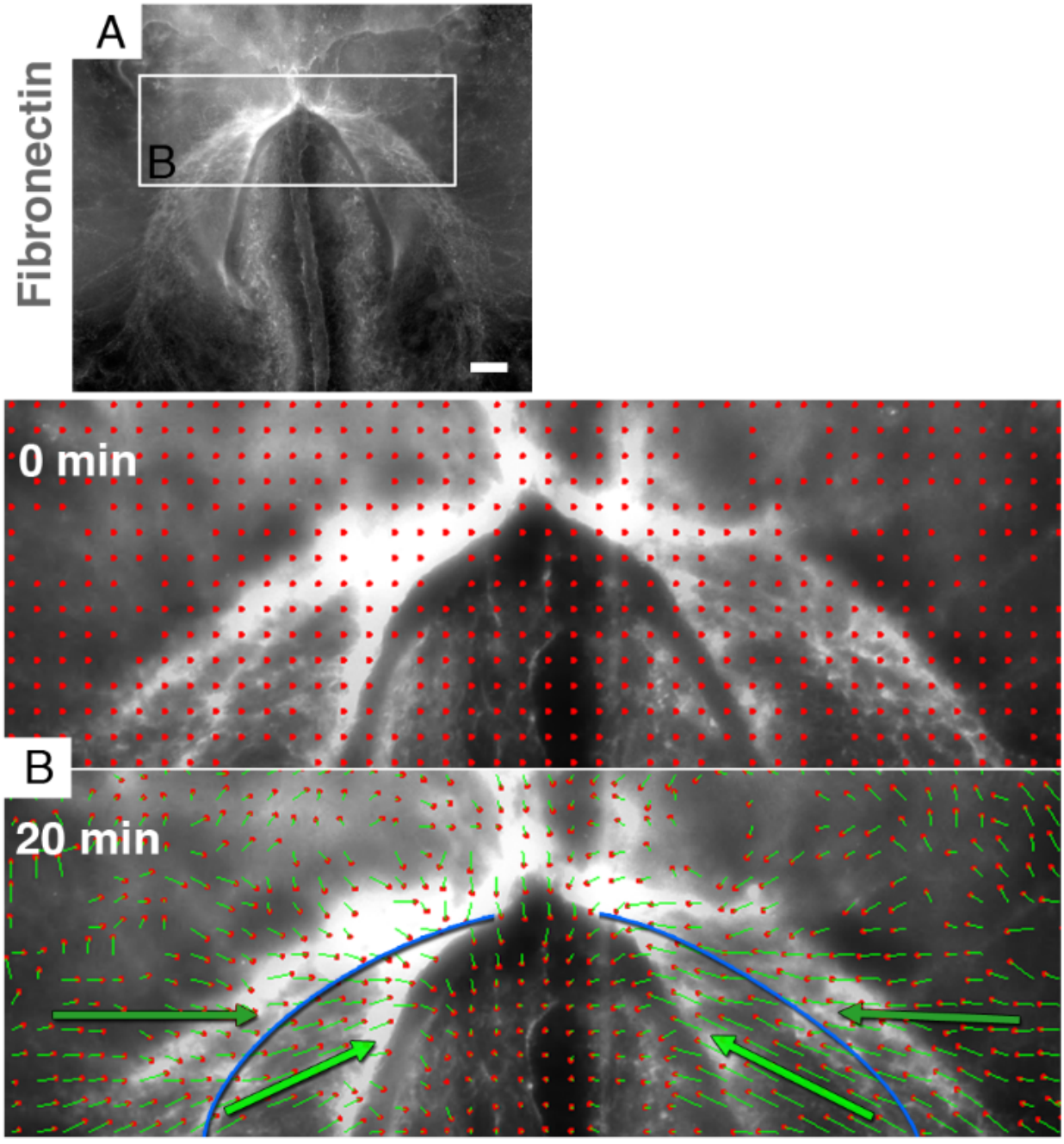

Mechanical perturbations, placed within specific regions of the heart fields, abrogate endoderm folding and reveal autonomous myocardial movements

In the attempt to release myocardial progenitor fields from the displacement-inducing influences of other tissues, most notably of the endoderm, we used tungsten needles to perform a series of incisions through the endoderm and underlying splanchnic mesoderm in selected regions within the anterior embryo at HH8. Myocardial progenitors and fibronectin ECM were labeled in each embryo as described above, prior to the surgery. Incision site positions are illustrated in Fig. 3.6A. In most cases (except for Fig. 3.6B), incisions were placed symmetrically at both sides of the embryo, to maintain the symmetrical distribution of forces (characteristic for normal development) acting on the wound. The number of embryos that underwent each type of perturbation, with time-lapse recording of subsequent events, ranged from n=6 for Figs. 3.6C and D to 34 for Fig. 3.6E.

Perturbations to the ventral midline endoderm have been shown to induce separation of cardiac progenitor fields, termed cardia bifida, by a number of early researchers (Glanzer and Peasley, 1970; Rosenquist, 1970; Satin et al., 1988). We were interested to determine if deformations within the myocardial field, described in the previous section (i.e. medial aspect contraction and concomitant ventral bending of the lateral heart field aspect), were affected by endodermal perturbation. Fig. 3.6B illustrates, that cell elongation along the medial edge of the heart field persists in embryos exhibiting cardia bifida (Fig. 3.6Ba). Likewise, ventral displacement of the lateral edge of the myocardial field (as in Fig. 3.4) was also evident (note the change in

color of the cells located at the lateral edge of the myocardial field from blue/green to yellow/red portions of the spectrum in Fig. 3.6Bb, where images were colorcoded as previously described).

In Fig. 3.6C, incisions were targeted laterally at approximately 100 um distance from the edge of the heart field. These types of incisions, as well as those placed medial to the myocardial fields (at the paraxial mesoderm or notochord; data not shown), had very little or no effect on the heart field movement towards the midline, and AIP regression.

Further, if 500-600 μm longitudinal incisions were placed within the myocardial field, a series of striking deformations ensued (Fig. 3.6D, Da). First, the myocardial fields gained unattached lateral edges, which bent ventrally and medially. Later, a portion of the heart field initially located posterior to the incision, advanced in the anterior direction past the wound edge. We propose, that observed deformations can be viewed as a cumulative result of forces exerted within the perturbed myocardial field. As illustrated in a schematic form in Fig. 3.6Db, the differentiating myocardium (dark green), attached to the surrounding non-myocardial mesoderm (light green), is undergoing a contraction along the medial edge (as in Fig. 3-4; magenta arrows). At the same time, it is also bending dorsally (via uniform curling) to generate a cup-shaped groove (as in Fig. 3-3; illustrated by blue arrows). The incision (red contour line) introduces an unattached edge, which in turn bends inwards (medially) as a result of the uniform dorsal bending/curling (blue arrows). The force generated by the isotropic curling in the myocardial field posterior to the incision propels the latter anteriorly (blue

segmented arrow) past the wound edge (red line), and causes further deformation of the perturbed myocardial primordium.

Even more pronounced myocardial field movement was achieved, when 200-300 *μ*m-long incisions were placed perpendicular to the AIP arch within the region demarcated with a white bracket in Fig. 3.6A. As seen in Fig. 3.6E, myocardial fields move anteriorly past the incision site. At the wound edge, the myocardium continues to advance over the ventral surface of the endoderm. This “rolling forward” movement of the myocardial fields drives cells at the wound edge to progressively more ventral and posterior positions (Fig. 3.6Ea). Figures 3.6Ec and 3.6Ed illustrate the cross-sectional anatomy of an embryo in Fig. 3.6E caudal to the posterior wound edge and at the level of the incision site, respectively. Note the characteristic cup shapes formed by the myocardial fields in the absence of endoderm folding. A portion of the myocardial field positioned ventrally relative to the endoderm in Fig. 3.6Ed also maintains a convex shape. Fig. 3.6Eb includes a schematic representation of the possible combination of forces acting on the perturbed myocardial field to generate the observed phenotype. As in Fig. 3.6Db the differentiating myocardium (dark green), attached to the surrounding non-myocardial mesoderm (light green), is undergoing a contraction along the medial edge (magenta arrows). Concomitantly it is also bending dorsally (by the uniform contraction) to generate a cup-shaped groove (blue arrows). The incision (red contour line) separates the myocardium and the adjacent non-myocardial mesoderm from the anterior tissues. The force generated by the uniform contraction (curling) of the myocardial field posterior to the incision propels the latter anteriorly (blue segmented

arrow) past the wound edge (red line). This process continues as bending is initiated at progressively more posterior levels of the differentiating myocardium. This drives further anterior displacement of the myocardial primordium and thus propels the formation of a characteristic “curl” at the wound edge.

As Figs. 3.6D and E demonstrate, the anterior-ward movement of the heart field continued when the anterior or lateral edge of the myocardial field was separated from the adjacent tissues, and in the absence of AIP regression-driven movement. Further, the myocardial fields in perturbed embryos underwent a characteristic c-shaped deformation similar, but more pronounced than that observed in normal embryos at HH8-9 (see Fig. 3.3B). We hypothesized that this deformation (driven by uniform curling), as it occurs progressively at more caudal aspects of the developing myocardial field, is responsible for the apparent myocardial endoderm-independent anterior-directed movements (quantified for normal embryos in Fig. 3.2). Our ongoing modeling efforts provide support to the stated hypothesis.

Figure 3.6. Typical phenotypes, induced by localized incisions through the endoderm and splanchnic mesoderm of HH8 embryos.

A – locations of incision sites (labeled B-E) that upon perturbation result in phenotypes shown in panels B-E.

Red – fibronectin ECM, green – CMLC2::GFP or CMLC2::mitoRFP-expressing myocardial cells. Gray contours delineate the wound edges at the beginning of an image acquisition. Myocardial fields are schematically outlined in red. Time elapsed from the beginning of time lapse image acquisition is listed on image panels. Acquisitions were typically initiated 0.5-1.5 h post-incision. Scale bars: 100 μm unless otherwise indicated.

B – selected images from the time-lapse sequence, illustrating that the **incision placed through the endoderm at the ventral midline** leads to the formation of two lateral "hearts" in the absence of midline fusion (a phenotype referred to as cardia bifida).

Ba, Bb – images of the embryonic left CMLC2::GFP-transfected myocardial field, color-coded to convey the information on dorso-ventral position as described previously. White contours illustrate the position of the AIP edge over time. Note the elongated shapes of CMLC2::GFP-expressing cells (indicative of a contraction; compare to Fig. 3-4) in Ba. An arrow and arrowhead in Bb indicate positions of the same cell groups in both images. Marked cells, along with the myocardial field region they were included in, assumed a more ventral position at the later time point.

Bc – confocal image of the embryo shown in B, stained with MF20 post-fixation (green) to visualize myocardial morphology in the bifid "hearts".

C – representative frames from a time-lapse sequence describing the development of an embryo, in which **incisions were placed through the endoderm and underlying splanchnic mesoderm lateral to the myocardial fields** (outlined by grey contours).

Ca - confocal image of the embryo shown in C, stained with MF20 post-fixation (green) to visualize myocardial morphology. Note that this type of perturbation does not prevent myocardial precursor arrival at the midline.

D – left panel: an initial time frame of an image sequence taken from an embryo with the **longitudinal incision placed within the myocardial fields (through the endoderm and differentiating myocardium) on both sides**. Subsequent deformations occurring within the region marked by the white rectangle are shown in the adjacent panels.

Da - confocal image of the region shown in D, stained with MF20 antibody (green) after post-imaging fixation to visualize myocardial morphology.

Db – a schematic representation of forces acting within the perturbed myocardial field to generate the observed phenotype. The differentiating myocardium (dark green), attached to the surrounding non-myocardial mesoderm (light green), is undergoing a contraction along the medial edge (as in Fig. 3-4; magenta arrows). At the same time, it is also bending dorsally to generate a cup-shaped groove (as in Fig. 3-3; illustrated by blue arrows). The incision (red contour line) introduces an unattached edge, which in turn bends inwards (medially) as a result of the uniform dorsal bending (blue arrows). The force generated by the dorsal bending in the myocardial field posterior to the incision propels the latter anteriorly (blue segmented arrow) past the wound edge (red line), and causes further deformation of the perturbed myocardial primordium.

E – representative frames from a time-lapse sequence describing the development of a specimen where **incisions were placed bilaterally perpendicular to the AIP arch through the endoderm and the underlying myocardium/splanchnic mesoderm.** Ea shows color-coded (as described previously) images that illustrate incision-induced deformations in the embryonic left myocardial primordium (positioned as the one outlined by the white rectangle in E). Note the progressive ventral displacement of the primordium ("curling").

Eb – a schematic representation of the possible combination of forces acting on the perturbed myocardial field to generate the observed phenotype. As in Fig. 3.6Db the differentiating myocardium (dark green), attached to the surrounding non-myocardial mesoderm (light green), is undergoing a contraction along the medial edge (as in Fig. 3-4; magenta arrows). Concomitantly it is also bending dorsally (by the uniform contraction) to generate a cup-shaped groove (as in Fig. 3-3; illustrated by blue arrows). The incision (red contour line) separates the myocardium and the adjacent non-myocardial mesoderm from the anterior tissues. As in Db, the force generated by the uniform contraction (dorsal bending) of the myocardial field posterior to the incision propels the latter anteriorly (blue segmented arrow) past the wound edge (red line). This process continues as bending is initiated at progressively more posterior levels of the differentiating myocardium. This drives further anterior displacement of the myocardial primordium and thus propels the formation of a characteristic "curl" at the wound edge. Ec and Ed are images of transverse sections taken through the embryo in E at the levels indicated in the right panel. Note that the myocardium forms pronounced cup-

shaped grooves posterior to the incision site (Ec), whereas the endoderm remains relatively planar. At the incision site (Ed), deformed ("curled") myocardium is found ventral to the endoderm. En – endoderm, mc – myocardium, nc – notochord, nt – neural tube, s – somite; D – dorsal, V - ventral, L – left, R – right. Scale bars in Ec and Ed: 50 μm.

Fig. 3.6A, B

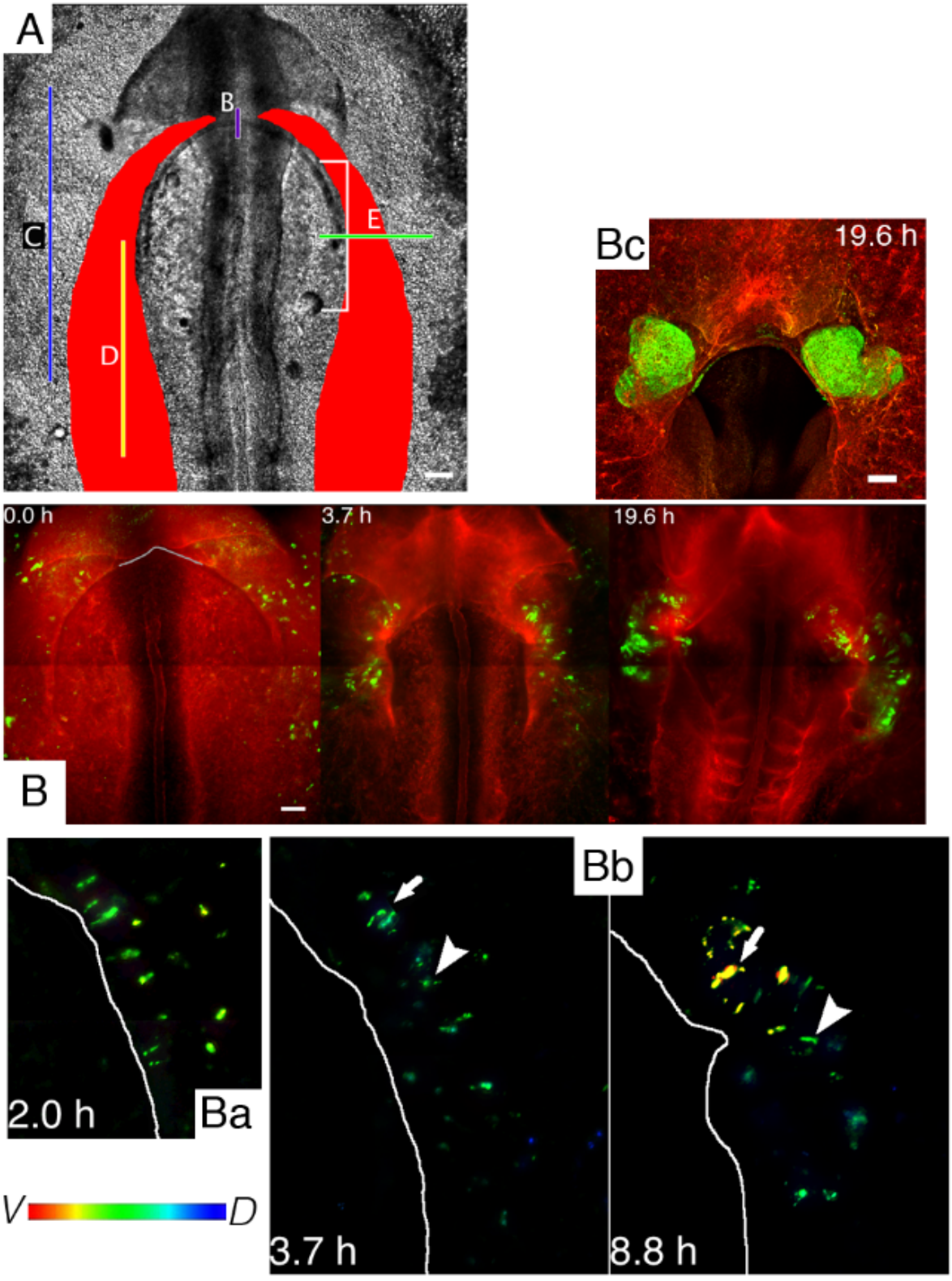

Figure 3.6C, D

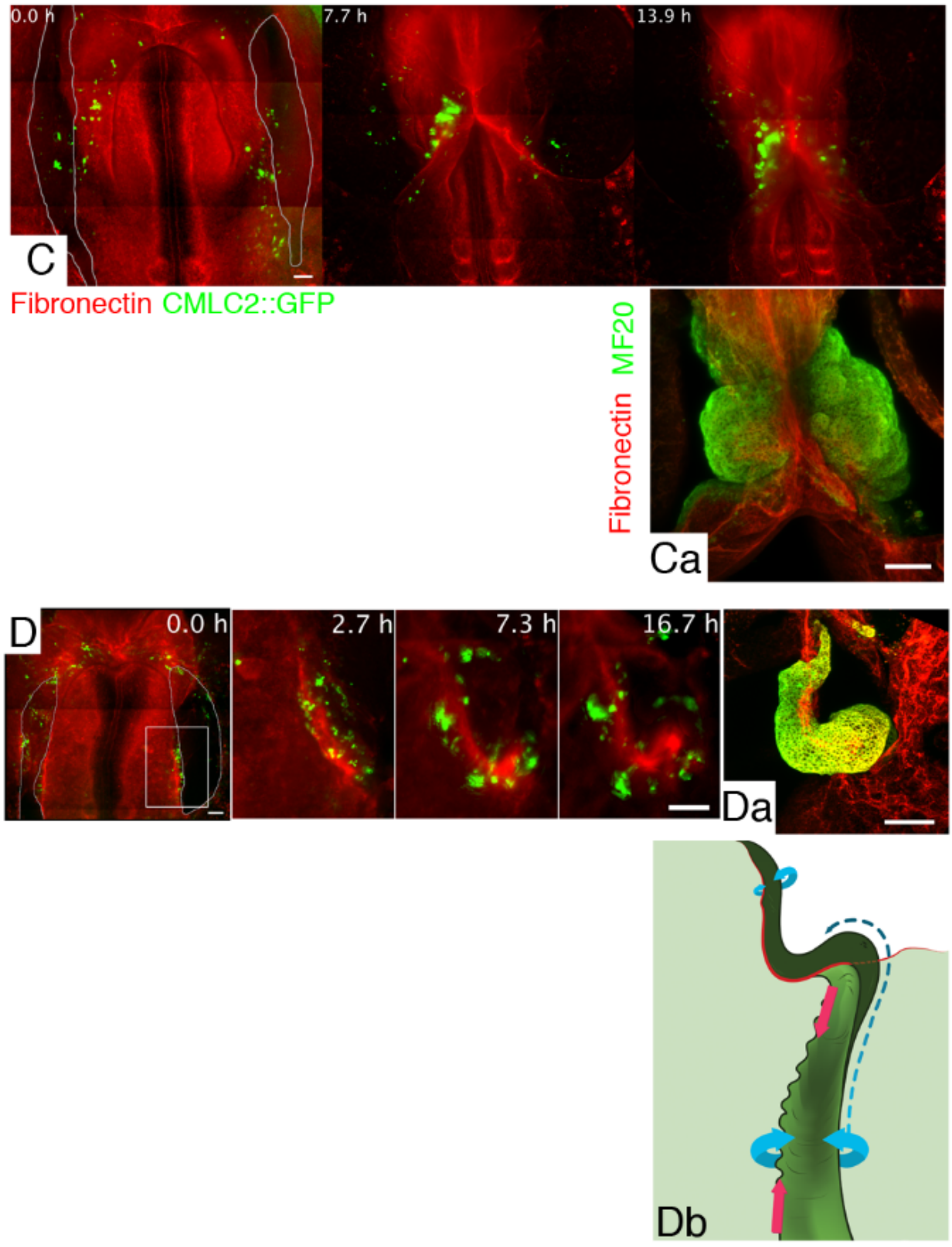
0.0 h
7.7 h
13.9 h
C
Fibronectin CMLC2::GFP
Fibronectin MF20
Ca
D
0.0 h
2.7 h
7.3 h
16.7 h
Da
Db

Figure 3.6E

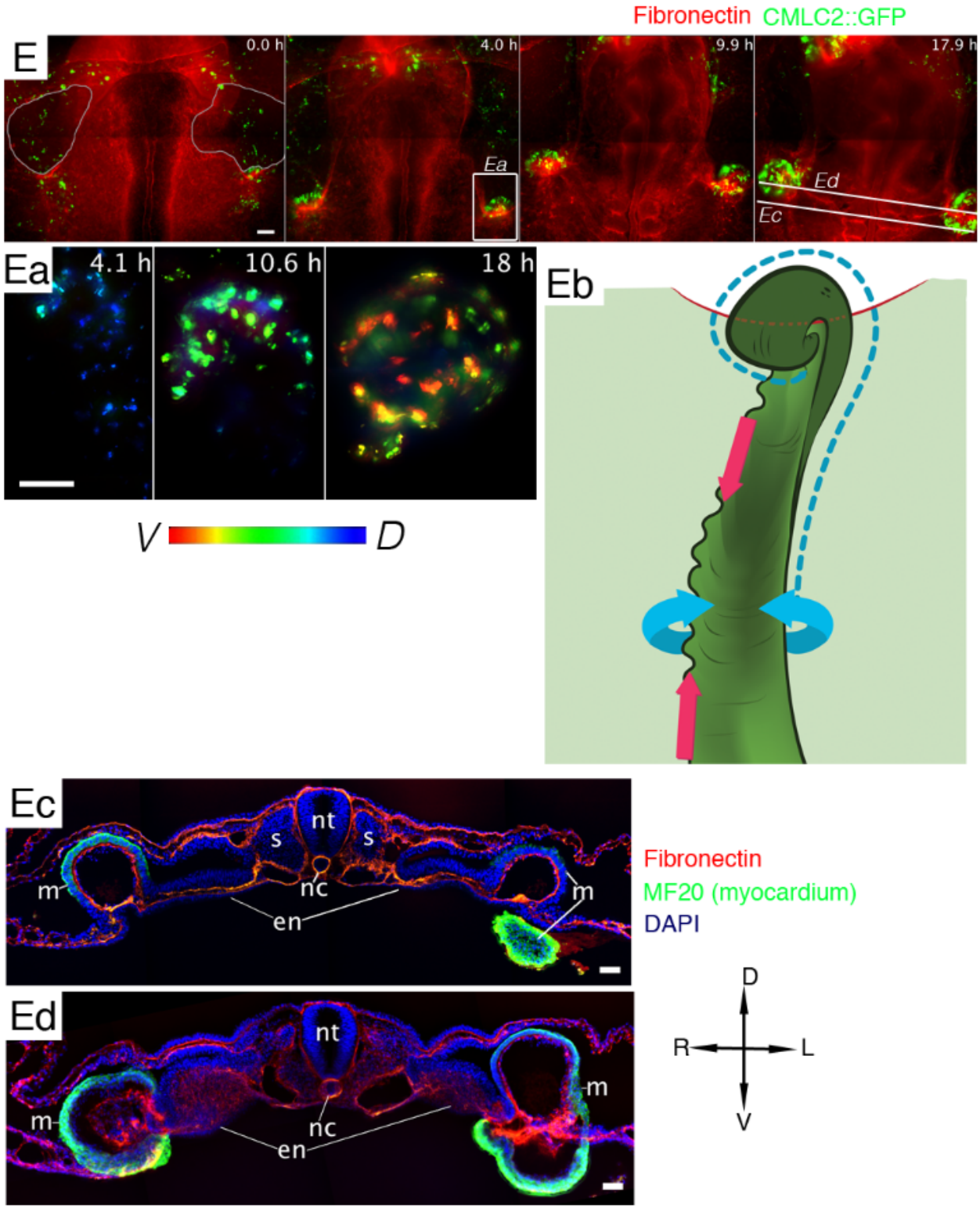
Fibronectin CMLC2::GFP
E
0.0 h
4.0 h
9.9 h
17.9 h
Ea
Ed
Ec
Ea
4.1 h
10.6 h
18 h
V
D
Eb
Ec
nt
s
s
m
nc
m
en
Ed
nt
m
m
nc
en
Fibronectin
MF20 (myocardium)
DAPI
D
R
L
V

Computational modeling of myocardial progenitor field behavior

Recently, we developed a substantially modified version of Dr Newman's subcellular element model (ScEM; Newman, 2005). Currently one particle represents a single cell, but the mechanical connectivity of the cells is explicitly represented as elastic beams connecting adjacent particles. The beams can be compressed and stretched, bent and twisted. Therefore, instead of the central forces of the original ScEM, these links can exert torques and forces that are not parallel to the line connecting the particles. The great advantage of explicit cell-cell contact representation is that we can formulate plastic stress relaxation by removing and inserting these links, as well as by changing the equilibrium properties of these links. Thus, for example, convergent-extension movements can be simulated by preferentially creating new links along one direction while removing links in the perpendicular direction. As each link is a simple elastic beam, the mechanical equilibrium of the structure can be calculated by solving the steady state of a coupled Ordinary Differential Equations (ODE) system. We argue, that the tissue is always in mechanical equilibrium, i.e., cell activity (contraction, rearrangement of the links) is slow compared to the time needed for the environment to accommodate these changes.

To analyze the tissue mechanics of the myocardial cell sheet, first we created a 3D model of the splanchnic (ventral) and somatic (dorsal) mesodermal layers surrounding the coelom as shown in Fig. 3.7A-C. In this hypothetical configuration the tissue is at rest as there are no cellular activities. By computational simulations we

evaluated the effect of a specific myocardial activity, which (in the absence of other mechanical constraints) would generate a uniform and isotropic curvature of the sheet. As Figs. 3.7D-F and 3.8 demonstrate, due to the mechanical interplays within the model, such a simple cellular activity can result in tissue deformations which are markedly distinct from the prescribed behavior, and show a great degree of similarity with the empirically observed myocardial movement patterns. In particular, at the anterior AIP the myocardium dislocates anteriorly relative to the more ventral endoderm layer. Furthermore, by moving the ventral (splanchnic) mesodermal layer medially, such a myocardial activity would contribute to the regression of the AIP. As an additional test, the model (with the same parameters) can also reproduce the observed ventrally curled myocardial layer, which develops as a response to a mechanical incision across the lateral AIP (Fig. 3.9).

Figure 3.7: Two characteristic states of a computational model developed to analyze the interplay between myocardial field deformations and the AIP movement.

The myocardium (red) is represented in a three dimensional arrangement within its mesodermal environment (white) shown from a posterior (a,d), anterior (b,e) and ventral (c,f) viewpoint. a-c: A hypothetical configuration in which myocardial cells do not exert any influence on their neighbors. This state serves as an initial condition for the simulations d-f: A configuration obtained by a simulation with active myocardial shape changes. A myocardial groove (arrows) develops, which protrudes into the coelomic cavity. A: anterior, P: posterior, D: dorsal, V: ventral. L: left, R: right.

Figure 3.7

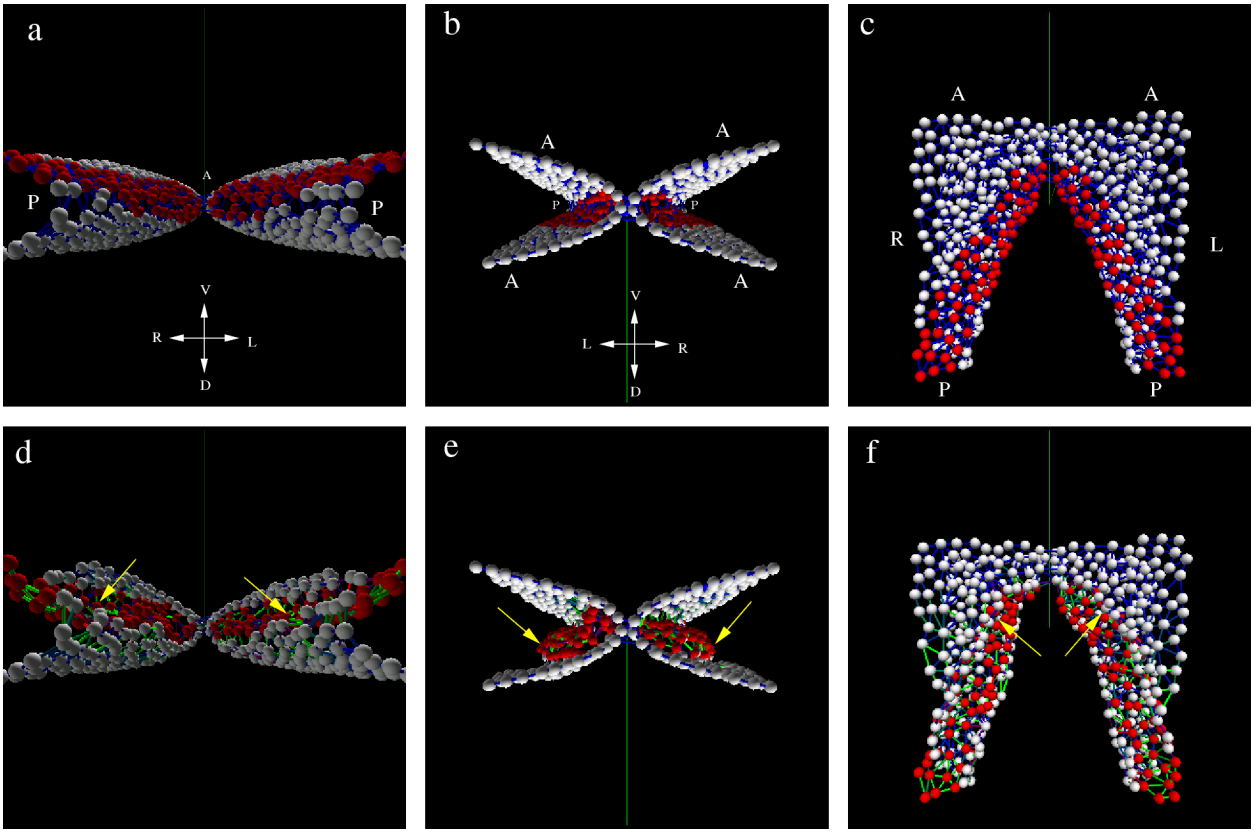

Figure 3.8: Myocardial and mesodermal cell displacements in the computational model, induced by a prescribed shape change of the myocardial fields resulting in a uniform and isotropic curvature.

Ventral-projected myocardial and mesodermal (non-myocardial) cell displacements are represented as red and green arrows, respectively. The sole myocardial activity was prescribed as a shape change resulting in a uniform and isotropic curvature (i.e., the same bending in the A-P and lateral-medial directions). Yet, due to the mechanical coupling with the surrounding tissue, this activity resulted in a lateral-anterior directed displacement of the myocardium in the anterior region (asterisk). The deformation of the myocardial cell stripe also induced a medially directed displacement of the ventral (splanchnic) mesoderm (bracket).

Figure 3.8

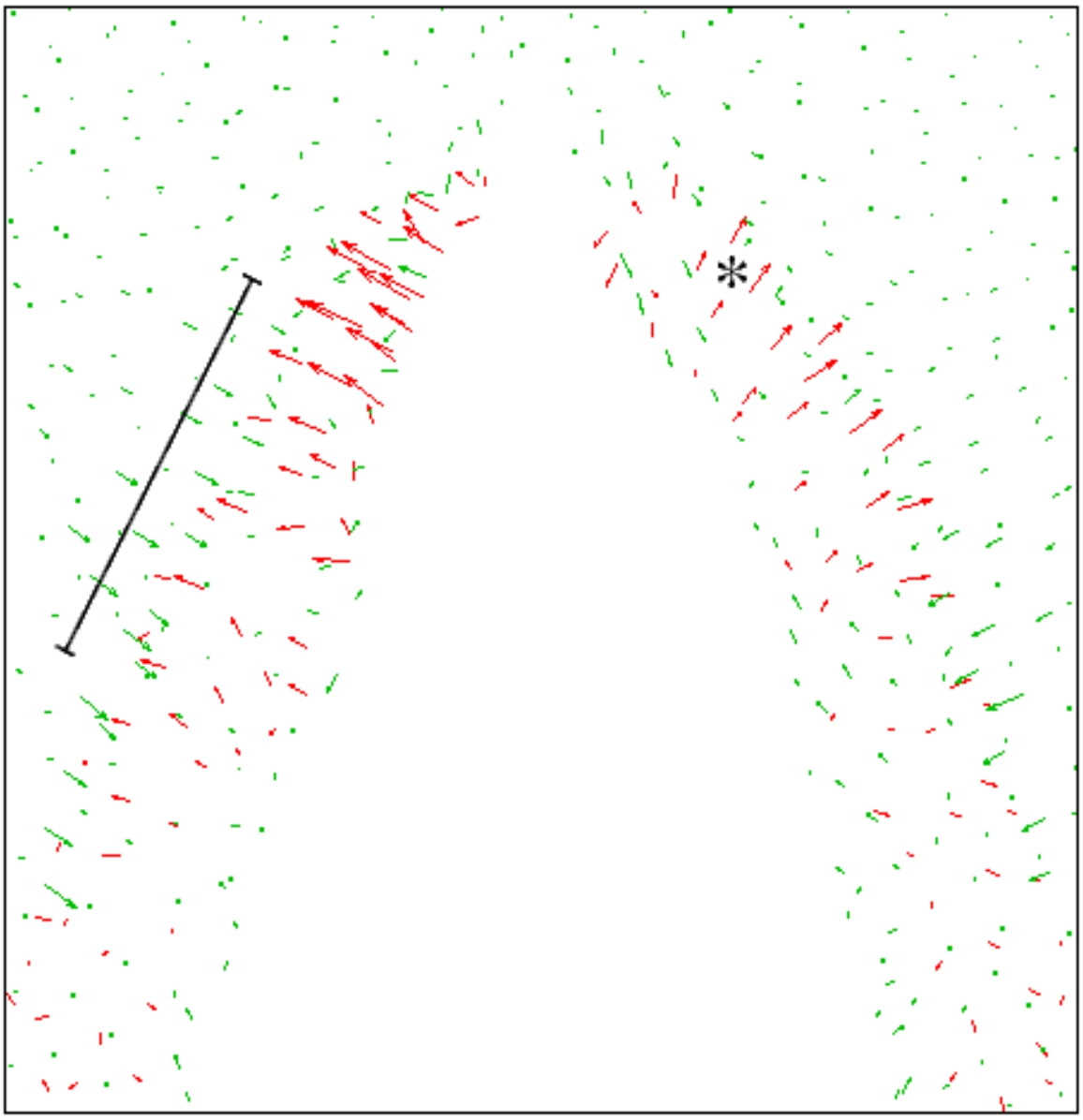

Figure 3.9: Computational simulation of endoderm/splanchnic mesoderm disrupting incision, placed perpendicular to the AIP arch. A mechanical discontinuity was introduced into the initial configuration by removing interconnecting beams along a line at the embryonic right side (yellow arrows), shown from a ventral (a) and lateral (b) aspect. The same myocardial behavior that was shown in Figs 3-7 and 3-8 here resulted in a pronounced ventral curling of the myocardium (blue arrows), shown from a ventral (c), lateral (d) and posterior (e) aspect. Compare to the incision-induced phenotype in Fig. 3-6E. A: anterior, P: posterior, D: dorsal, V: ventral. L: left, R: right.

Figure 3.9

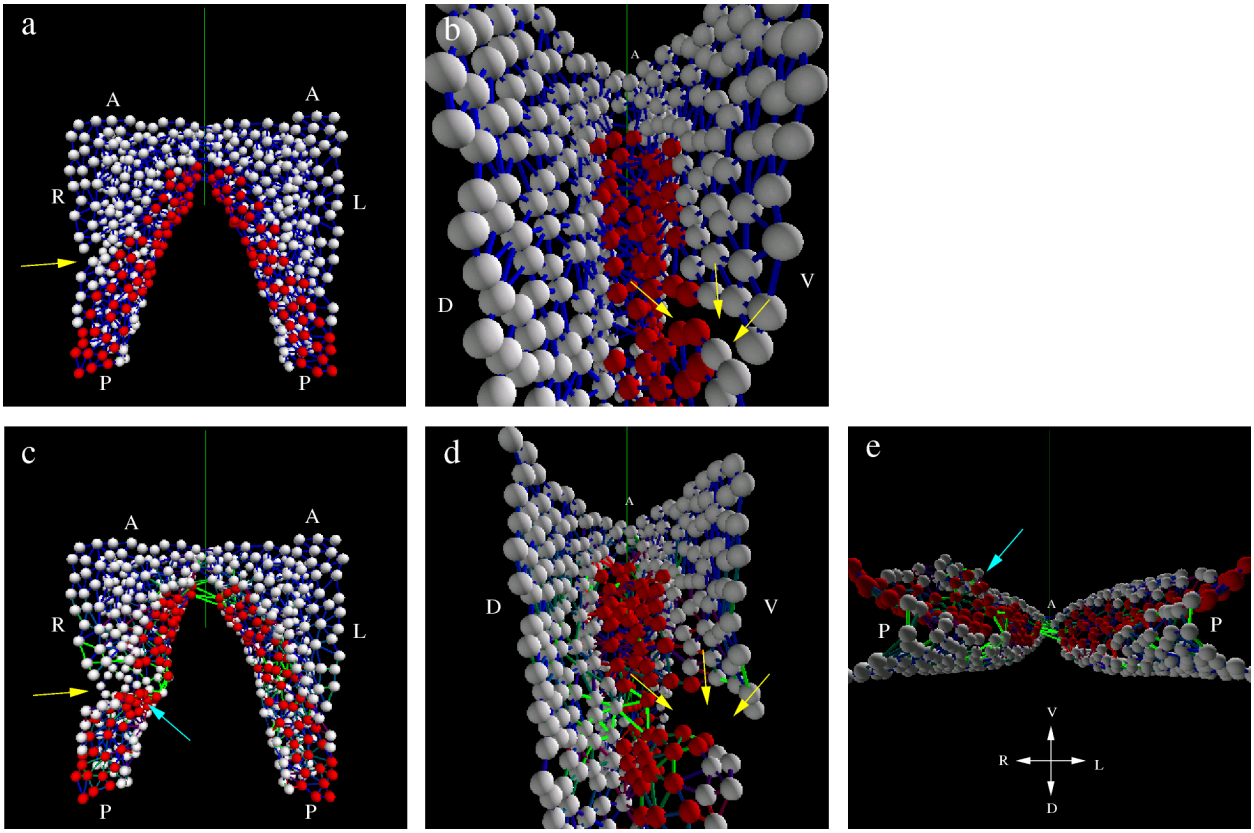

Proposed model to explain antero-medial displacements of the myocardial fields prior to heart tube assembly

Based on the data available to us, we propose the following combination of the concomitantly acting forces to act on and within the developing myocardial fields, and promote their observed antero-medial displacement. As seen in Fig. 3.10, the myocardial field (dark green) is incorporated into the cohesive mesodermal layer (light green). The myocardial field is located in the close vicinity of the AIP (purple semi-arch), and the mesoderm is overlain by the endoderm (the top, light purple tissue layer), continuous with the AIP. The latter undergoes a uniform contraction (purple arrows), leading to the midline-directed displacement of the mesoderm along with the incorporated myocardial field (a single purple arrow above the AIP). At the same time, the myocardial field undergoes the previously discussed deformations, namely the medial side contraction (pink arrows) and dorsal bending/curling (blue arrows). We argue that the combination of the above events leads to the net displacement of the myocardial field in the anterior and medial direction, illustrated by the segmented arrow in Fig. 3.10.

Figure 3.10: Proposed model to explain antero-medial displacements of the myocardial fields prior to heart tube assembly

A schematic representation of tissue deformations that occur within the myocardial fields at each side of the embryo, and within the adjacent tissues. Please refer to the text for an explanation.

Figure 3.10

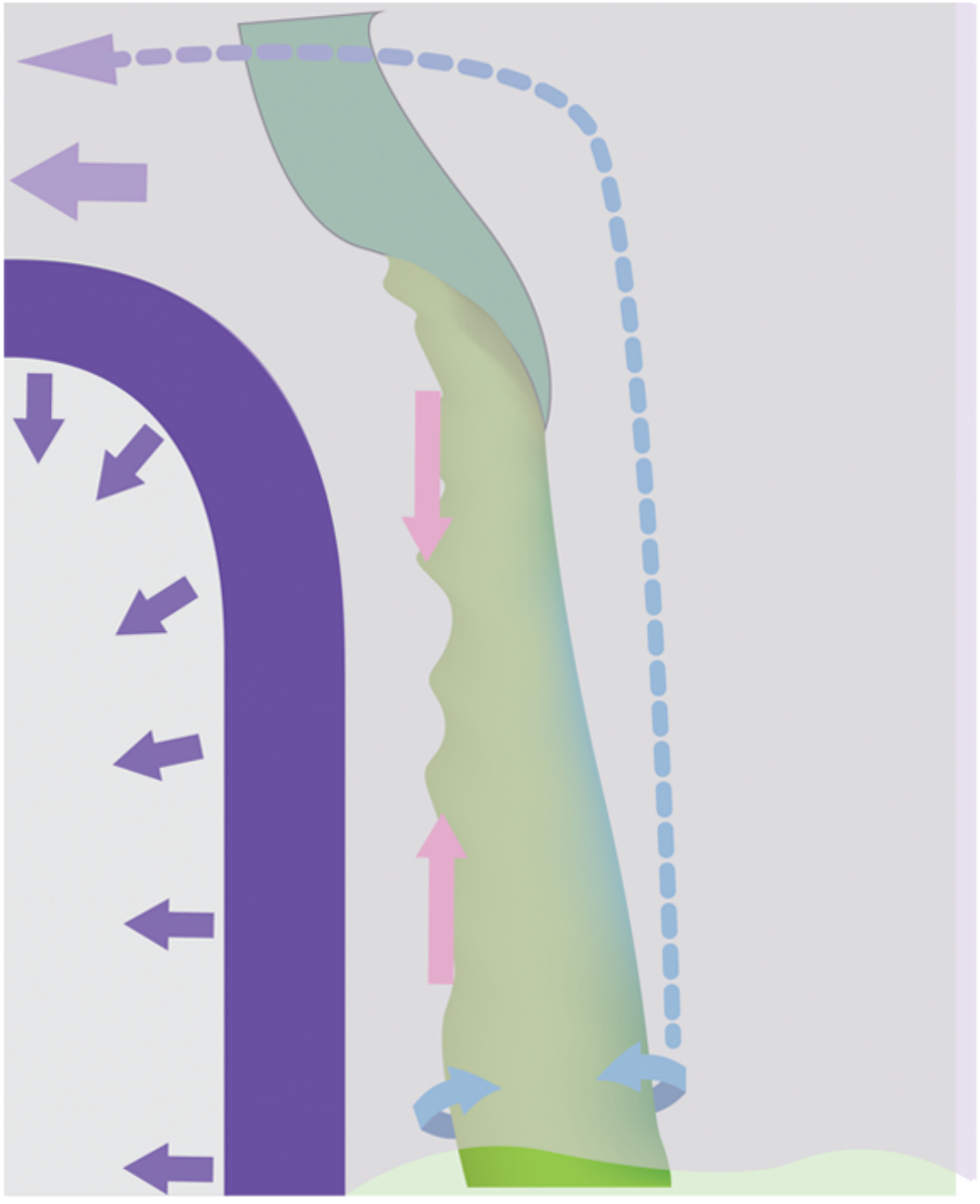

Comparison of the effects of known regulators of tissue contractility and cell movement on endodermal and myocardial tissue deformations

To determine whether AIP regression and autonomous myocardial field deformations are driven by similar cellular mechanisms, we subjected unperturbed and incised (as in Fig. 3.6E) HH8 embryos to treatments with various concentrations of the following: cell proliferation inhibitor Mitomycin C (Sigma), actin depolymerizing agent Cytochalasin D (Sigma), Rho kinase (p160ROCK) inhibitor Y27632, and focal adhesion kinase (FAK) inhibitor (Tocris Biosciences). The reagents we chose for analysis have been used in studies of cardiac morphogenesis, inducing measurable effects (Latacha et al., 2005; Wei et al., 2001; Doherty et al., 2010). The analyses described below were on applied to 3-6 time lapse sequences for each reagent and concentration, listed in Figs. 3.11B and D.

We used the speed of AIP regression as a way to assess the effect of each of the above reagents on foregut elongation, a process that relies predominantly on the endoderm contractility. The distance was measured between the center of the AIP arch and the anterior borders of the first visible pair of somites, at each time point of the image sequence, as schematically shown in Fig. 3.11A. Positions of the above anatomical landmarks were traced manually through the image sequences. From tracking data, the speed of AIP movement was calculated. Averaged values for AIP regression speed in the presence of the above reagents, or solvent controls, are listed in Fig. 3.11B. Out of all applied treatments, the following caused a statistically significant

decrease in the AIP regression speed: 250 and 500 μM of ROCK inhibitor Y27632, 750 μM of FAK inhibitor PF573228, and both 10 and 50 μM of Cytochalasin D.

To assess the effects of each reagent on myocardial deformation, movements of individual CMLC2::GFP+ or CMLC2::mitoRFP+ myocardial progenitors in the vicinity of the wound edge were traced manually throughout the image sequences (see Fig. 3.11C for illustration). The position of the ECM-rich incision edge was assessed at each time point using a version of the PIV algorithm as described in Experimental Procedures. Effects of the above reagents on the speed of the myocardial progenitor movement relative to the incision edge are shown in Fig. 3.11D. The observed decreases in the myocardial progenitor displacement speeds were only statistically significant in embryos treated with 500 μM of Y27632 and those subjected to 750 μM of PF573228, suggesting a significantly lower sensitivity of the myocardial deformations to actin depolymerization and ROCK inhibition compared to the endodermal deformations in the contracting AIP.

Further, we used the above experimental strategy to quantify the effects of myocardially-expressed constitutively active isoform of Rho (CMLC2::caRho) on the on the AIP regression speed and on myocardial displacement speed in the incised embryos. CMLC2::GFP-expressing embryos were used as controls for both assays. The results of measurements are shown in Fig. 3.11E for the effect of CMLC2::caRho expression on the AIP regression speed (n=15), and in Fig. 3.11F for its effect on the speed of myocardial displacements relative to the incision edge (n=4). Both AIP and myocardial displacement speeds were slightly decreased in CMLC2::caRho-expressing embryos compared to the controls. Despite is small magnitude, the difference in each

case was proven to be statistically significant with $p<0.05$ based on the results of two-tailed Welch's t-test. In our early experiments we have also attempted to assess the effects of dominant negative isoform of Rho (CMLC2::dnRho), but neither of our measured parameters was affected by the myocardial-specific dnRho expression (data not shown).

Figure 3.11. Analysis of effects of inhibition of cell proliferation, Rho kinase and focal adhesion kinase function, and actin polymerization on the AIP regression (endoderm contraction) speed and myocardial field deformations.

A – a DIC image of an HH8 embryo illustrating the anatomical landmarks traced for the AIP regression speed analysis (the center of the AIP arch and borders of the first somite pair). The linear trajectory of AIP regression is shown, and the extent of its early, intermediate, and late portions according to our convention are defined. Scale bar: 100 μm.

B – a bar chart reflecting the speeds of AIP regression in control- and reagent-treated embryos at the intermediate portion of the regression trajectory (3.11A). Reagents and treatment concentrations are listed. Error bars: SEM.

C – epifluorescence images illustrating the anatomy of a myocardial field progressively undergoing deformations in the embryo perturbed as in Fig. 3.6E, and defining the landmarks used in tracing analysis. Arrowheads indicate the positions of the myocardial cells (additionally marked with numbers 0-2) tracked through the 13.6 h-long time-lapse sequence. Asterisks mark the incision edge positions. Red – fibronectin ECM, green – CMLC2::GFP-transfected myocardial cells. Scale bar: 100 μm.

D - a bar chart reflecting the speeds of myocardial progenitor movements relative to the incision edge in control- and reagent-treated embryos in specimens that were perturbed as in Figs. 3.6E and 3.11C. Reagents and treatment concentrations are listed. Error bars: SEM.

E, F – bar charts representing the effects of the myocardial-specific expression of caRho on the speeds of AIP regression (E) and those of the myocardial progenitor movements relative to the incision edge (F) in CMLC2::caRho-expressing embryos compared to the controls.

Figure 3.11A-D

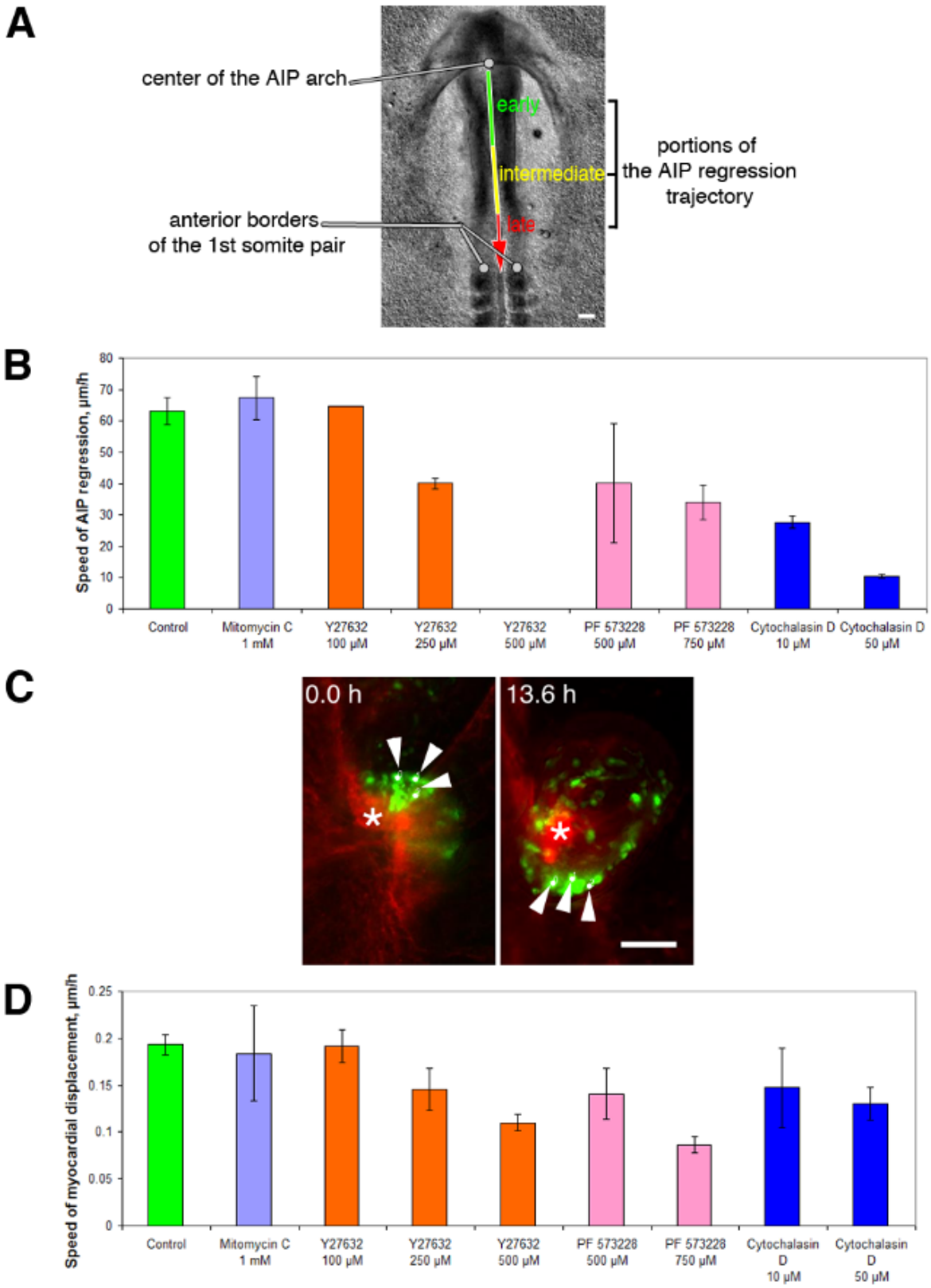

Figure 3.11E,F

E

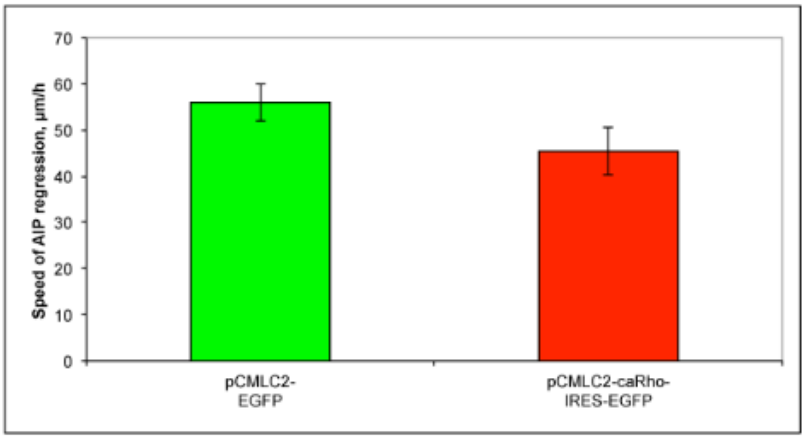

F

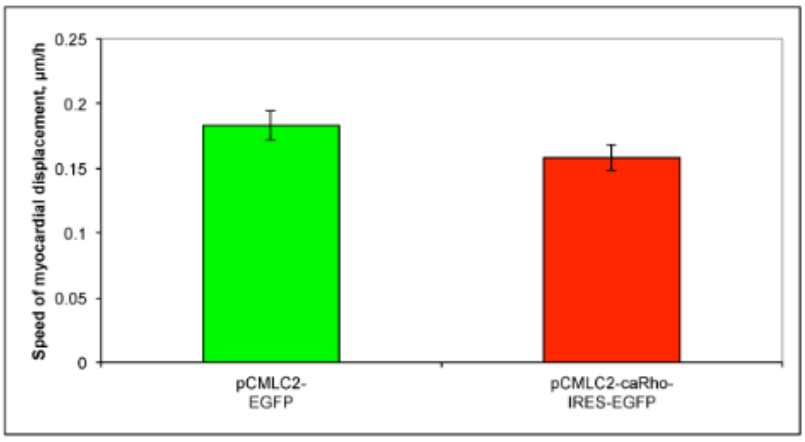

Discussion

The relationship between fibronectin, endoderm, and myocardial progenitor movements

Fibronectin was suggested to be organized in an anterior-to-posterior gradient, and to serve as a substrate for haptotactic movements of cardiac progenitors in a series of publications by Linask and Lash (Linask and Lash, 1986; Linask and Lash, 1988a; Linask and Lash, 1988b). On the contrary, Wiens (1996) proposed that myocardial movement is driven by the contractile activity of the anterior-most cells within a cohesive epithelial sheet. These cells were expected to interact with the anteriorly-positioned "patch" of fibronectin, activate their motility mechanisms, and create the contractile force needed to propel the remainder of the myocardial fields forward. Very recently, Varner et al. (2012) published a study where the endoderm, and not the myocardium, was implicated as the source of a midline-directed contractile force.

In order to determine if myocardial progenitors undergo displacements relative to any (or both) of the suggested substrates, we performed a series of time-lapse microscopy and PIV analysis-based motion analyses.

As seen in Fig. 3.1A, fibronectin is associated with both the myocardium and endoderm. In our *in vivo* fibronectin labeling strategy, both fractions become tagged (data not shown). Hence, we can detect movement relative to both the endoderm- and myocardium-associated fibronectin. As illustrated in Fig. 3.1B, most of the midline-directed myocardial movement is shared with fibronectin displacement. Accordingly,

speeds of apparent myocardial movement (green bars in Fig. 3.1C) are very similar in magnitude to ECM movement speeds (brown bars) at all stages considered.

Interestingly, throughout HH8-11 we observe myocardial progenitor movement speeds relative to fibronectin (active) to exceed those of endocardial progenitors (red versus blue bars in Fig. 3.1C). It is in agreement with the fact that active movements of endocardial progenitors were directed towards the midline (see Fig. 2.7, S2.5), whereas myocardial movements had a pronounced anterior directionality (Fig. 3.2B,C).

Next, we set out to characterize the morphological changes that occur within myocardial progenitor fields during HH8-9 – the period of rapid convergence of cardiac progenitors at the midline, which encompasses a striking transition from completely separated planar “sheets” to a three-dimensional early heart tube at the midline.

Visualization of individual cells within the myocardial progenitor fields allowed us to detect clear differences in behaviors of medially- and laterally-positioned cells (Fig. 3.4). Pronounced cell rearrangement and elongation at the medial edges can be viewed as the source of the force that acts (in parallel with the AIP regression) to mediate the 120º-130º inversion of the cardiac fields, described by Abu-Issa and Kirby, 2008.

Further, fibronectin ECM associated with the AIP at HH8-9 included a lateral domain with mostly medial-directed displacement of included fibrils, and a medial domain, where such displacement had a distinct anterior directionality. Given that this ECM is located at the interface of the endoderm and the myocardial field, coupling the two contractile tissues, dual interpretation of the data is possible. In the first scenario, the endoderm would play a primary role in the contraction, and compress the

mesoderm. In the second, the mesoderm would contract (via elongation of the cells as seen in Fig. 3.4), and contribute to the contraction of the endoderm.

To distinguish between these possibilities, and to assess myocardial movement with reduced influence of the endoderm, we performed a series of microincisions. First, we found evidence for persisting medial aspect contraction and ventral folding (120º-130º inversion) of the myocardial fields in embryos with cardia bifida. Further, we found that if a myocardial field acquires an unconstrained (free) edge, the latter quickly bends inwards without any appreciable influences from surrounding tissues. Most interestingly, if AIP regression is disrupted symmetrically, and the incision crosses the entire 150-200 μm width of the myocardial progenitor field, the latter continues to move cranially and ventrally in the absence of normal, AIP formation-associated endodermal movements.

Further, using computational modeling we were able to reproduce the anterior-directed movements of cardiac progenitor fields by prescribing the uniform contraction within the myocardial sheet to generate a cup-shaped bend – a morphology characteristic to the myocardium at HH8-9 (Fig. 3.3; Abu-Issa and Kirby, 2008; van den Berg et al., 2009). This change alone was not only able to "propel" the myocardial fields forward, but also move the rest of the splanchnic mesoderm medially, which could aid the AIP regression. At the current stage, our model does not account for the influence of the endoderm or that of medial heart field aspect contraction. So, in an interesting way Fig. 3.9 corresponds to the distribution of forces in the embryo with midline incision-induced cardia bifida (Fig. 3.6B). Namely, in the absence of the endoderm driving the convergence of the fields at the midline, they move in an antero-lateral direction, an

event that results in the formation of two independent “half-hearts” in live embryos (Glanzer and Peasley, 1970; Rosenquist, 1970; Satin et al., 1988).

In the final set of experiments (Fig. 3.11), we address the roles of actin cytoskeleton, Rho kinase, FAK, cell proliferation and myocardial-specific expression of a constitutively active Rho isoform on endodermal contraction (with the AIP regression speed as a read-out) and autonomous myocardial deformations, driving the displacements of heart fields past the incision edge in perturbed embryos (Fig. 3.6E). We found, that inhibition of cell proliferation by Mitomycin C had virtually no effect on either dynamic process. The treatment was effective in reducing cell proliferation, typically resulting in over 3-fold decrease in the mitotic index (measured by automated counting of phosphorylated H3-positive nuclei in control and Mitomycin C-treated specimens; data not shown). Both AIP regression and myocardial deformation were sensitive to perturbation on ROCK and FAK function, although endoderm deformation was disrupted by lower concentrations on perturbing reagents. Myocardial deformations appear to be relatively resistant to actin depolymerization. Strikingly, myocardial expression of caRho had mild, yet significant effect on both processes. This last result may have interesting implications (discussed in detail in Chapter 5) as to the possible mechanisms that couple myocardial and endodermal tissue contractilities.

In conclusion, we argue that the observed bending of the myocardial sheet, which progressively develops in a posterior-to-anterior direction (concomitantly with the onset of expression of myocardial differentiation markers within the progenitor fields), and cell-shape change-mediated medial heart field aspect contraction represent the

forces responsible for the displacement of the myocardial field in the anterior direction. Endodermal contraction is responsible for bringing the myocardial fields to the midline and juxtaposing them for effective fusion.

Applicability of the proposed mechanism to other model systems of heart development

In zebrafish and *Xenopus* endoderm and cardiogenic mesoderm are involved in signaling interactions. For instance, when *Xenopus* deep endoderm was co-cultured with the heart primordia, cardiogenesis was enhanced (Nascone and Mercola, 1995). In zebrafish both myocardial and endoderm development are dependent on GATA5 function, aberrant in *faust* mutants (Reiter et al., 1999). Zebrafish *casanova* (Alexander et al., 1999) and *one-eyed-pinhead* (Schier et al., 1997) mutants both lack the endoderm and demonstrate cardia bifida phenotypes. In contrast to endoderm folding-based foregut morphogenesis of avians and mammals, in zebrafish and *Xenopus* the gut develops from a rod of cells, that undergoes luminization. In zebrafish, such a rod forms as a result of midline-directed movements of bilateral endoderm progenitor populations. These movements resemble those of the cardiac progenitors (Sakaguchi et al., 2006; Arrington and Yost, 2009), and can similarly be disrupted by knockdown of syndecan 2 (a transmembrane heparan sulfate proteoglycan that initiates fibronectin and laminin assembly). However, in *natter* mutants (fibronectin; Trinh and Stainier, 2004) cardia bifida is observed, yet foregut morphogenesis is not affected, suggesting that endodermal and cardiac progenitors rely on distinct mechanisms for arrival at the

midline. Holtzman et al., 2007, established the requirement for the endocardium for successful completion of myocardial progenitor movements during zebrafish heart tube assembly.

Altogether, it is unlikely that zebrafish cardiac progenitors rely on the endoderm to physically drive their convergence at the midline. However, it would be interesting to investigate if myocardial progenitor populations in zebrafish undergo tissue deformations similar to those we describe for avian embryos, during their midline-directed movement. The need to maintain the ability to undergo deformations in a coordinated fashion could explain the strict requirement for epithelial organization (maintained by interactions with fibronectin), a condition that Trinh and Stainier (2004) demonstrated to be critical for myocardial convergence at the midline in zebrafish.

What is a possible cellular mechanism underlying bending of the myocardial sheet?

To begin to understand whether myocardial progenitors utilize any of the well-studied mechanisms of epithelial sheet bending, such as apical constriction (Sawyer et al., 2010) we looked at cell shapes of MF20+ labeled myocardial progenitors in transverse sections through the heart fields in embryos perturbed as in Fig. 3.6E (n=3). Classic examples of apical constriction-driven processes are usually exerted by elongated or wedge-shaped cells, such as, for instance, bottle cells in *Xenopus* (Hardin and Keller, 1988) or ventral furrow cells in *Drosophila*. Perturbed embryos were chosen as they demonstrate more robust bending of the myocardial sheet than unperturbed embryos at HH8-9. Figure 3.12 contains a representative example, allowing the

illustration of the typical cell shapes at several locations throughout the c-shaped myocardial field. As presented in Fig. 3.12B, a group of cells at the medial edge of the group of myocardial cells have elongated shapes. The border between these cells and their less elongated neighbors is rather sharp (indicated by arrows in Fig. 3.12B; the border between the MF20+ myocardial cells and the adjacent splanchnic mesoderm is shown with arrowheads in Figs. 3.12B and D). It is likely that these cells are involved in the contraction of the medial aspects of myocardial fields (Fig. 3.4). At the same time, the cells at the central and lateral aspects of the c-shaped myocardial field demonstrate a variety of spindle, rounded, and cuboidal cell shapes. Given these cell morphologies, it is very difficult to imagine that myocardial sheet bending would be brought about by uniform apical constriction.

We made another interesting observation regarding myocardial sheet bending in normal HH8-9 quail embryos (n=4). Namely, when the myocardial field transitions from flat to convex, the number of cell layers in its wall increases from one to two or three. Fig. 3.13 shows two sections (same embryo as Fig. 3.3) taken at different levels along the anterior-posterior embryonic axis (A is more cranial than B). Insets include higher magnification images through a single cell-thickness of the myocardial field in Fig. 3.12B', and a thicker wall of the myocardial field in Fig. 3.12A'. We think that bending is unlikely to be the direct result of a local cell proliferation increase, as high concentrations of Mitomycin C had no effect on the myocardial movement (which we believe to be an outcome of tissue deformation/bending; Fig. 3.11D). Also, several in-depth studies of cell proliferation within the developing heart concluded that the early

myocardium at stages HH8-9 showed low proliferation rates with cell cycle lengths exceeding 32 hours (van den Berg et al., 2009; de Boer, 2012). At the same time, cells in the adjacent non-myocardial mesoderm divided rapidly. In the model of heart growth proposed by van den Berg et al. ventral bending of the myocardial sheet (referred to as "luminization" by the authors) coincided with halting of active proliferation.

A theoretically possible mechanism that could result in the bending of a 2-3 layered sheet of cells would be if a number of cells from the bottom sheet repositioned into the top one(s). In this way, the bottom-most layer of cells would eventually acquire flattened, squamous morphology and develop tension sufficient to account for the ventral-ward bending of a myocardial sheet. We currently test this possibility with computational modeling. However, more experimental evidence is needed to definitively understand the mechanisms driving myocardial tissue deformations.

Figure 3.12: Characteristic cell shapes at medial, lateral, and central aspects of the deformed myocardial field.

A – transverse section (10 μm thick) through the embryonic left side of a quail embryo that underwent the incision across the AIP arch at HH8 as in Fig. 3.6E, and developed for 16 h post-perturbation. Red labeling corresponds to myocardial cells (MF20), green – to fibronectin (B3D6), and blue – to cell nuclei (DAPI). Some red labeling of fibronectin is due to the interaction between the goat anti-mouse secondary antibodies (used to visualize MF20 binding), with B3D6 antibody (mouse), delivered to the tissues by microinjection prior to the incision. Nt – neural tube, nc – notochord, s – somite, sm – splanchnic mesoderm, mc – myocardium, e – endoderm. Scale bar: 100 μm.

B-D – higher magnification confocal (left panels) and DIC (right panels) images of regions delineated by accordingly marked rectangles in A. Arrows in B indicate the transition from columnar to rounded cells, and arrowheads in B and D show transition from the MF20+ myocardium to the non-myocardial mesoderm. Scale bars: 10 μm.

Figure 3.12

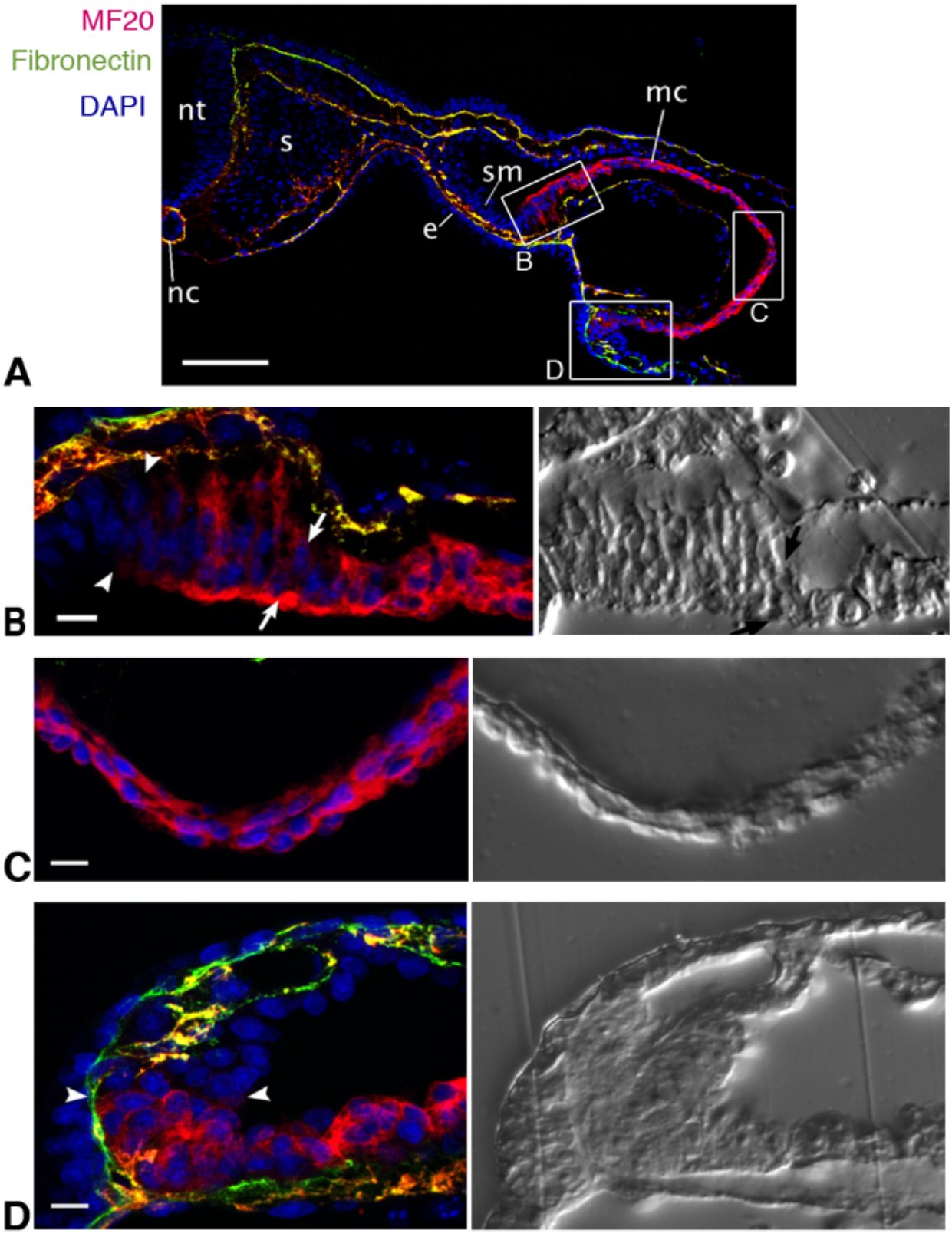

Figure 3.13: Transition from flat (posteriorly) to bent (anteriorly) organization of the heart field occurs concomitantly with an apparent increase in the number of cell layers comprising the MF20+ myocardium.

A and B – transverse sections through the HH8 embryo (also shown in Fig. 3-3). Embryonic region shown in A is approximately 200 μm anterior to B.

A' – a higher magnification image of the region outlined with the rectangle in A.

B' – a higher magnification image of the area corresponding to the region outlined in B, acquired from the next (10 μm posterior) serial section. A: anterior, P: posterior; e: endoderm, mc: myocardium.

Note that myocardium appears to include several cell layers in A (compare arrangements of nuclei marked by asterisks in A' and B').

Scale bars: 50 μm

Figure 3.13

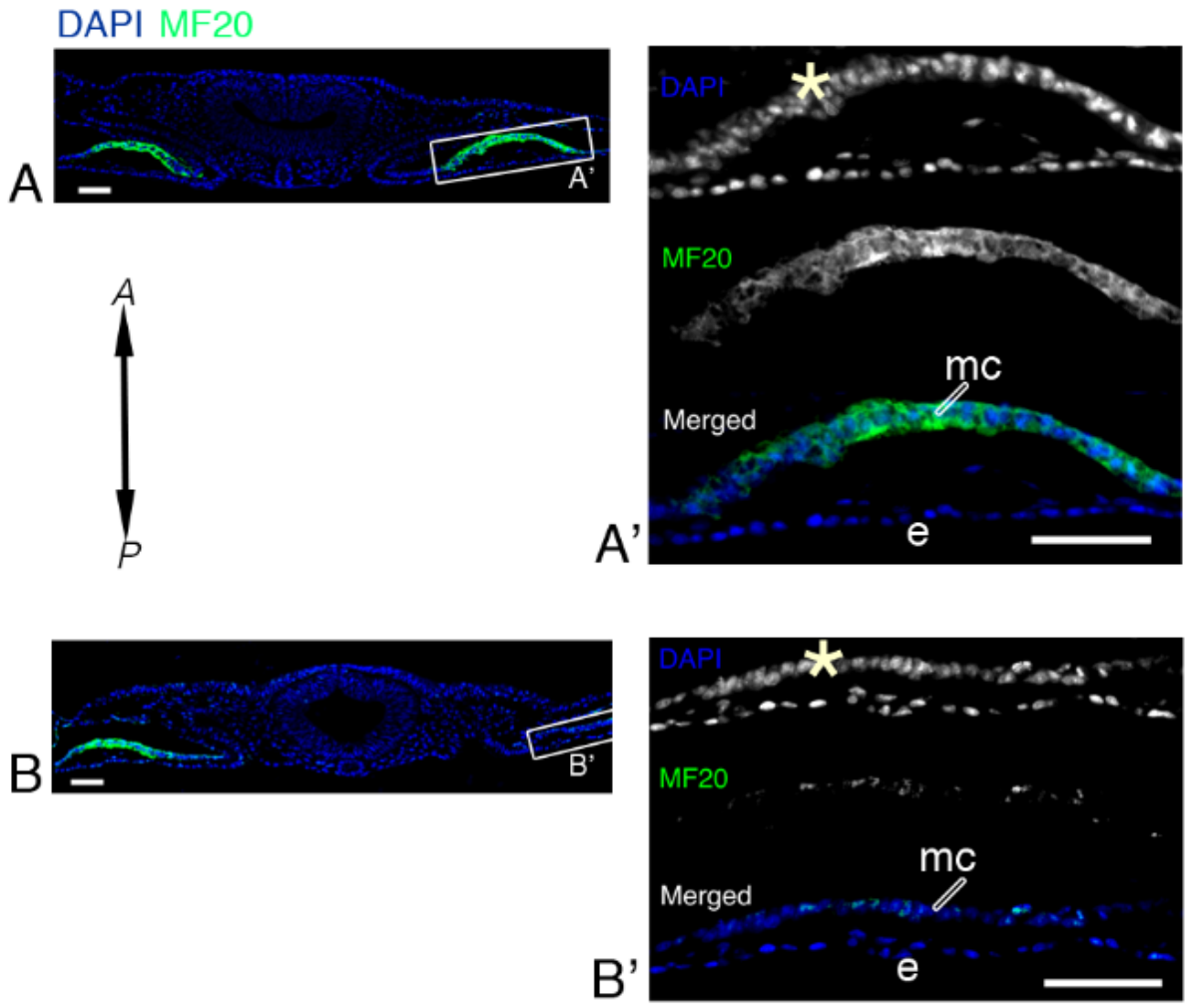
DAPI MF20
A
A'
A
P
DAPI
MF20
mc
Merged
e
A'
B
B'
DAPI
MF20
mc
Merged
e
B'

CHAPTER FOUR:

VEGF signaling over-activation affects cardiac progenitor movements and results in defects in cardiac tube elongation

Abstract

Signaling by vascular endothelial growth factor (VEGF) plays an integral part in cardiovascular development, yet little is known of its role during early heart development. We introduce exogenous rhVEGF165 into quail embryos at the stage preceding heart tube formation (HH8) and use time-lapse microscopy to visualize the effects of the treatment on heart tube assembly and early elongation. Surprisingly, the treatment resulted in significant reduction of the heart tube size in VEGF165-injected embryos compared to controls. At the same time, perturbed embryos included dramatically enlarged areas of differentiated (MF20+) myocardium positioned caudal to the tubular heart and dorsal to the abnormally expanded inflow region. Results of cell tracing-based measurements indicate that the speed of myocardial progenitor movements towards the midline is significantly reduced by VEGF165 treatment. Furthermore, the rate of incorporation of newly differentiated myocardium into the cardiac posterior pole is also reduced, and coordinated myocardial deformations are affected by VEGF over-activation. Inhibition of VEGF signaling by VEGF-R2 blocker SU5416 did not affect the timing of heart tube assembly. Interestingly, neither excessive activation, nor inhibition of VEGF signaling affected the rate of foregut elongation – a process responsible for the bulk of midline-directed cardiac progenitor movements. From the data available to us, we propose that gross enlargement of the cardiac inflow/omphalomesenteric vein region, induced by exogenous VEGF exposure, creates a barrier that mechanically prevents the myocardial progenitor fields from undergoing a coordinated deformation that enables their fusion at the midline. Together, these

processes lead to a pathological reduction of heart tube size in VEGF165-treated embryos compared to the controls. Our results emphasize that a proper balance of cell type constituents, which can be easily shifted by inappropriate levels of VEGF signaling, is critically important for cardiac organogenesis.

Introduction

Vascular endothelial growth factor (VEGF) signaling through receptor tyrosine kinases FLK1 (VEGF-R2, KDR) and FLT1 (VEGF-R1), and neuropilins, plays a central role in development of the cardiovascular system. VEGF is a glycoprotein produced in multiple alternative splicing isoforms, which differ in their receptor binding characteristics and ability to interact with extracellular matrix constituents. VEGF165 isoform is often used in gain-of-function studies due to its high potency and bioavailability (Drake and Little, 1995; Feucht et al., 1997; Grunstein et al., 2000; Drake et al., 2006). Multiple studies have established roles for VEGF as a potent inducer of endothelial cell proliferation (Ferrara and Henzel, 1989; Keck et al., 1989), survival (Benjamin et al., 1999; Gerber et al., 1999), differentiation (Risau and Flamme, 1995), and migration (Senger et al., 1996). It can also act as a mitogen and migration stimulant for other cell types, such as leucocytes or Schwann cells (Clauss et al., 1990; Sondell et al., 1999).

The tremendous importance of VEGF signaling in embryogenesis is illustrated by the outcomes of gene knock-out studies in mice. If a single VEGF allele is deleted, embryos die at E11-12 due to massive vascular abnormalities (Carmeliet et al., 1996; Ferrara et al., 1996). Further, if both VEGF alleles, or any of the VEGF receptor alleles are removed, the onset of embryonic lethality occurs at E8.5-9.5 (Shalaby et al., 1995; Fong et al., 1999; Nagy and Rossant, 1999). The upper threshold of VEGF signaling, permissive for normal development, is also defined within narrow margins. The study by Miquerol et al. (2000) showed that a 2-3 fold increase of VEGF production causes

pronounced cardiac and vascular abnormalities, resulting in midgestational lethality. The mutant embryos developed multiple myocardial defects, outflow track abnormalities, aberrant ventricular septation and altered coronary artery development. In avian models, exogenous VEGF was shown to induce abnormal hypervascularization, dilation and fusion of embryonic vessels if delivered at HH8-9 (Drake and Little, 1995), and to increase vascular permeability when overexpressed in the limb bud of a day 10 embryo (Flamme et al., 1995). When delivered at embryonic day 4.5 in quail, VEGF caused multiple cardiac and venous abnormalities (Feucht et al., 1997). More recently, Drake et al. (2006) showed that exposure to exogenous VEGF165 caused defects in cardiac looping. The studies mentioned above provided important knowledge about abnormal cardiovascular phenotypes resulting from VEGF over-activation. However, the information is scarce regarding the dynamic aspects of response to VEGF overexposure, and its effects on early heart tube assembly.

In the current study, we deliver recombinant human VEGF165 to quail embryos just prior to initiation of heart field fusion and record the induced changes in fluorescently labeled cardiac progenitor motility by means of time-lapse imaging. In agreement with known roles of VEGF in vascular development, we observe massive expansion of the endothelial/endocardial component of the cardiac inflow region and adjacent omphalomesenteric veins. Surprisingly, VEGF overexposure leads to development of shorter heart tubes, and more caudally - enlarged areas of differentiated (MF20+) myocardium, in treated embryos compared with controls. Results from analyses of myocardial progenitor movement speeds, dynamics of cell addition to the

cardiac posterior pole, and the rate of foregut elongation measurements suggest a connection between VEGF-induced changes in the size of the cardiac inflow and ensuing defects in the heart tube elongation process, observed in response to excessive VEGF signaling in embryonic quail.

Experimental Procedures

Quail embryo isolation

Fertile eggs of wild type or Tie1::H2B-YFP transgenic quail (*Coturnix coturnix japonica*; Ozark Egg Co., Stover, MO) were incubated at 37°C to reach stages HH6 to HH11 (Hamburger and Hamilton, 1951). Embryos were then isolated, placed on paper rings, and cultured as in Cui et al., 2009 (modified EC culture; Chapman et al., 2001).

Myocardial progenitor labeling

pCMLC2::mitoRFP plasmid DNA in complex with Lipofectamine 2000 (Invitrogen) was delivered into the subendodermal spaces of wild type and Tie1::H2B-YFP embryos at HH5-6 by microinjection using a PLI-100 (Harvard Instruments) apparatus. Embryos were incubated at 37°C for 4-5 h until the fluorescent signal from reporter expression became detectable.

Wide-field time-lapse imaging

Automated microscopy of immunolabeled quail embryos was performed as described elsewhere (Czirok et al., 2002; Zamir et al., 2008). Briefly, this imaging system is based on a computer-controlled widefield epifluorescent microscope (Leica

DMR series) workstation, equipped with a motorized stage and connected to a cooled digital CCD camera (QImaging Retiga-SRV). Most experiments utilized a 10X objective (.25 NA). The images are acquired using both epifluorescence and differential interference contrast (DIC) optics. Acquired images have 12-bit grayscale intensity and a resolution of 1.33 μm/pixel. One time point ("frame") of the time lapse sequence typically consists of 4-8 images taken at slightly overlapping xy locations of the embryo ("tiles"), with 7-9 focal (z) planes in each tile. The length of the time interval between consecutive frames depends on the number of focal planes, fields and optical modes and is usually within the range of 2-20 minutes. Up to 12 embryos can be imaged per recording. During image acquisition the embryos are kept at 37°C in a thermostatically-controlled chamber. Custom image processing software (TiLa, KUMC), based on code described in Czirok et al., 2002, was used to create high resolution 2D time-lapse sequences for cell/ECM tracking and Particle Image Velocimetry (PIV) analyses. To enhance contrast, selected epifluorescence image stacks were deconvolved by a commercial, blind adaptive deconvolution software (Autoquant X, MediaCybernetics).

Post-fixation immunofluorescence labeling

Embryos were fixed and prepared for immunolabeling according to Little and Drake, 2000. Monoclonal antibodies against avian epitopes (B3D6, QH1; DSHB, Iowa City, IA), directly conjugated to AlexaFluor 488, 555 or 647, were added at 1:1000 dilutions, and mouse monoclonal antibody MF20 (DSHB, Iowa City, IA) – at 1:10 dilution

in 3% BSA for overnight incubation. Goat anti-mouse secondary antibodies, conjugated to AlexaFluor 488, 555 or 647 (Molecular Probes, Eugene, OR), were used to follow the MF20 staining at 1:1000 dilution in 3% BSA.

Confocal imaging

Confocal imaging of whole-mount embryo specimens was performed using a Nikon 90i upright microscope with a Nikon C1 confocal scan head and Nikon Plan Apochromat 10x and 20x objectives.

Preparation of transverse plastic sections

Embryos were dehydrated through a graded ethanol series, placed in JB4 infiltration medium (Electron Microscopy Sciences, Hatfield, PA) at 4ºC overnight, and embedded in JB-4 resin following the manufacturer's protocol. Subsequently, 10µm sections were prepared.

Manual tracing of cells and other image details

Manual tracing of image details was performed using custom software (see, e.g., Czirok et al., 2004). Briefly, this software allows marking points of interest within a

series of image stacks, i.e. tracing movement in three dimensions. In this study, only the markers' projections to a frontal plane were assessed.

rhVEGF165 treatments

Unless otherwise specified, 250-300 ng of rhVEGF165 (R&D Biosciences) in PBS were delivered by a single microinjection to the ventral midline (just anterior to the center of the AIP arch) of quail embryos at HH8-8+. This amount was selected because it consistently causes a rapid onset of inflow region expansion, allowing assessment of induced changes in heart tube assembly in relatively young (HH10-12), and hence more optically transparent, embryos. Control embryos received injections with the same amounts of BSA (Sigma) dissolved in PBS. Embryos were then incubated at 37°C for 12-16 h, or subjected to time-lapse imaging. In general, prior to initiation of the image acquisition, embryos were incubated at 37°C on the microscope stage for 1-1.5 h.

SU5416 treatments

An 80 mM DMSO stock solution of SU5416 (Tocris Biosciences) was prepared according to the manufacturer's instructions. Prior to the treatment, the stock solution was dissolved to the working concentration of 1 or 2 mM in PBS, and 20 μl of the resultant solution were delivered to the ventral surface of the embryos in EC culture. Embryos were then incubated at 37°C for 4-12 h, or subjected to time lapse imaging.

Results

Treatment with rhVEGF165 provokes massive changes in the anatomy of the developing vascular system

To investigate the development of a VEGF overactivation-induced hypervascularization phenotype (Drake and Little, 1995) in time lapse, we subjected eight Tie1::H2B-YFP HH8+ embryos to microinjection with a solution of rhVEGF165 as described in *Experimental Procedures,* in two independent experiments. Seven control embryos received BSA injections. VEGF-treated and control embryos were then subjected to time-lapse image acquisition for approximately 19 hours. Following completion of imaging experiments, embryos were fixed, processed histologically, and 10 μm transverse sections were prepared. Fig. 4.1A includes selected time points of representative image sequences describing the development of BSA- and VEGF-treated embryos. Note the distinct vascular patterning (with dorsal aortae and lateral vascular plexus, separated by avascular areas) in the control embryo (left panels in Fig. 1A). The diameter of the omphalomesenteric veins (OV) was dramatically increased in a VEGF-treated embryo compared to the control. Further, in the control embryo the omphalomesenteric veins were displaced caudally (while maintaining a relatively consistent diameter; Fig. 4.1A) concomitantly with the elongation of the heart tube and regression of the AIP. At the same time, in the VEGF-treated embryo the anterior edge of the OV retained its initial position (arrowheads in Fig. 4.1A), whereas the posterior

OV edge was progressively displaced posteriorly, with concomitant increase in the OV diameter. Notably, the endocardial portion of the heart tube did not appear to increase in length with advancing time in VEGF-treated embryos.

The cross-sectional anatomy of a control and VEGF-treated embryo is illustrated in Fig. 4.1B. The fragmented appearance of the endocardium and decreased volume of cardiac jelly in VEGF-treated embryos are consistent with findings of Drake et al., 2006.

Figure 4.1: Exogenous rhVEGF165 treatment leads to defects in vascular patterning and a dramatic expansion of the omphalomesenteric veins in quail embryos.

A – selected frames from a time lapse image sequence describing development of BSA-treated (left panels) and rhVEGF165-treated (right panels) Tie1::H2B-YFP-transgenic embryos from HH9 to HH13. Elapsed times from the beginning of an acquisition are listed in the top left corners of images. DA – dorsal aortae, HT – heart tube, OV – omphalomesenteric veins. Asterisks indicate an avascular space separating the DA from each lateral vascular plexus in BSA-treated embryos. Arrowheads point to the anterior edge (on the embryonic right side) of the OV, allowing tracing of its posterior-ward displacement in the BSA-treated embryo and maintenance of a stationary position in the VEGF-treated specimen. Scale bars: 200 μm.

B – DIC images of transverse sections through BSA- and VEGF-treated embryos at the level of the heart tube. E – endocardium, M – myocardium, ECM – extracellular matrix of the cardiac jelly. Note the disorganized appearance of the endocardium and the decreased volume of the cardiac jelly in the VEGF-treated embryos compared to the controls.

Figure 4.1

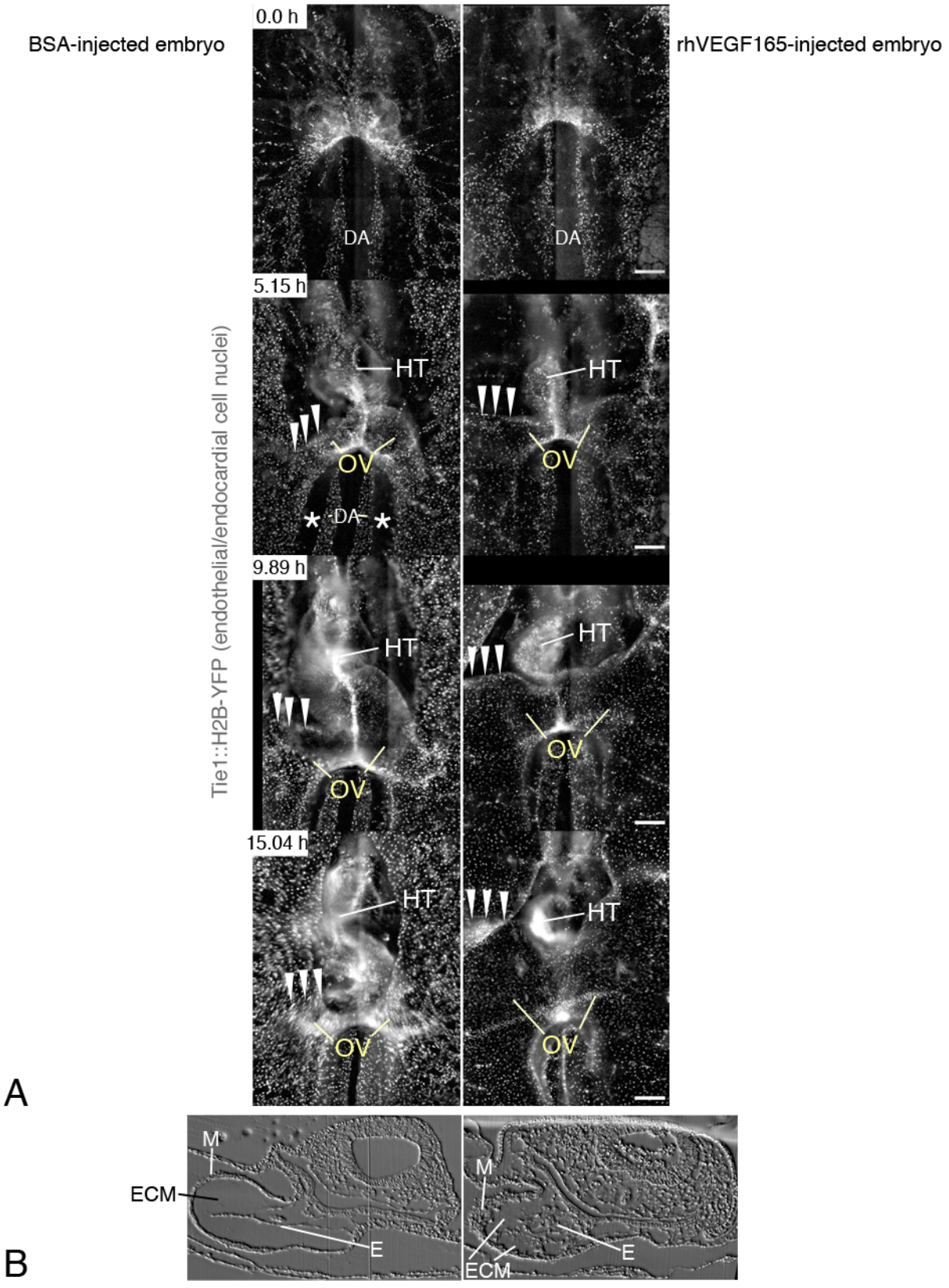
BSA-injected embryo
rhVEGF165-injected embryo
0.0 h
5.15 h
9.89 h
15.04 h
DA
HT
OV
Tie1::H2B-YFP (endothelial/endocardial cell nuclei)
A
M
ECM
E
B

Exogenous VEGF treatment results in a decrease in the heart tube size with concomitant expansion of the MF20+ separated myocardial primordia at the dorsal surface of the cardiac inflow region

To quantitatively measure changes in heart tube size, induced by exogenous VEGF treatment, embryos were microinjected with VEGF (n=19) or BSA solution (n=14) as described above, and incubated at 37ºC for 14 h. After fixation, embryos were labeled with MF20, QH1, and B3D6 antibodies to visualize myocardial cells, endocardium/endothelium, and the fibronectin ECM, respectively. Images of each specimen were then acquired as z-stacks with a Leica DM6000 epifluorescence microscope, at 10x magnification. Some embryos were also subjected to confocal imaging for illustration purposes (see Fig. 4.2A). After image acquisition, transverse sections through VEGF-treated and control specimens (n=4, 2 for each type) were prepared (Fig. 4.2B). Note an increased length of the MF20+ myocardium at the dorsal surface of the inflow region in VEGF-treated embryos compared to the controls (asterisks in Fig. 4.2B).

In order to measure the surface area of the heart tube and separated myocardial primordia, the outlines of the above structures were traced manually in z-projected images, and the surface area of each selection was quantified using the Measure tool in Image J software. In Fig. 4.3A the heart tube (defined here as a continuous structure located anterior to the inflow region/OV) was outlined in each embryo in green, and areas of separated MF20+ myocardia (located posterior to the heart tube and dorsal to

the inflow region/OV) were outlined in red. The bar chart in Fig. 4.3B summarizes measurement results. In VEGF-treated embryos the surface area of the heart tube was decreased by 0.7 fold, but the size of separated myocardial primordia was increased by 2.2 fold compared to the control embryos.

Figure 4.2: Exogenous VEGF treatment results in a decrease in the heart tube size with concomitant expansion of the MF20-positive myocardium included in separated primordia flanking the inflow/OV region.

A – confocal images of control and VEGF-treated embryos with the myocardium (MF20) in red, endocardium/endothelium (QH1) in green, and fibronectin ECM (B3D6) in blue. HT – heart tube, OV – omphalomesenteric veins. Scale bar: 100 μm.

B – transverse sections through the embryos shown in A at the level of the heart tube (top panels) and omphalomesenteric veins (bottom panels). MF20-positive myocardium at the dorsal surfaces of the OV is marked by asterisks. A – anterior, P – posterior.

Figure 4.2

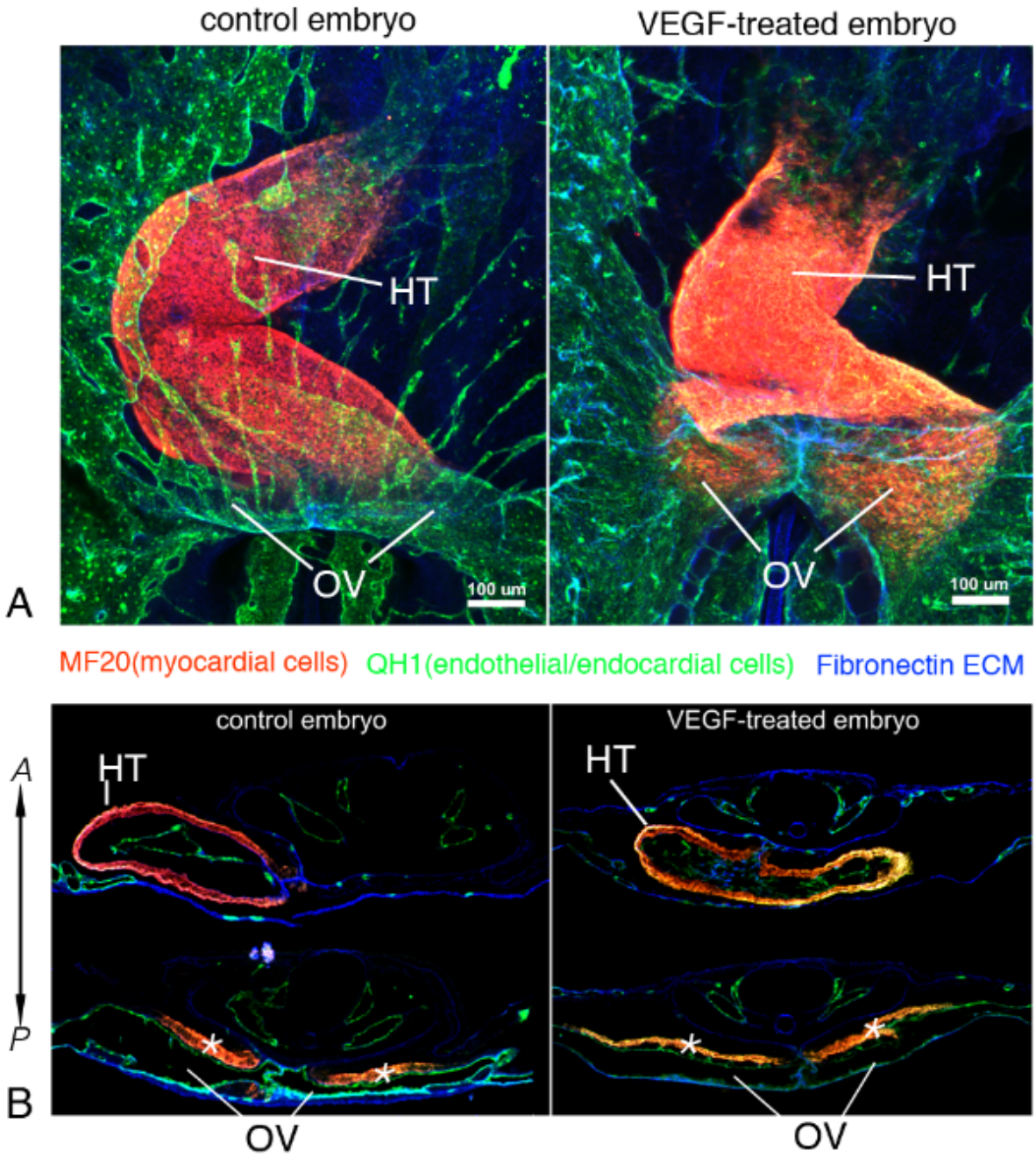
control embryo
VEGF-treated embryo
HT
OV
100 um
A
MF20(myocardial cells)
QH1(endothelial/endocardial cells)
Fibronectin ECM
control embryo
VEGF-treated embryo
A
P
B
HT
OV

Figure 4.3: Quantification of VEGF-induced changes in the sizes of the heart tubes and separated myocardial primordia.

A – confocal images of VEGF-treated and control myocardia (same specimens as Fig. 4.2) with heart tubes outlined in green, and separated MF20+ primordia flanking the OV - in red (see definitions in the text).

B – a bar chart illustrating mean values of surface area measurements for the myocardial regions defined in A. Error bars: SEM.

Figure 4.3

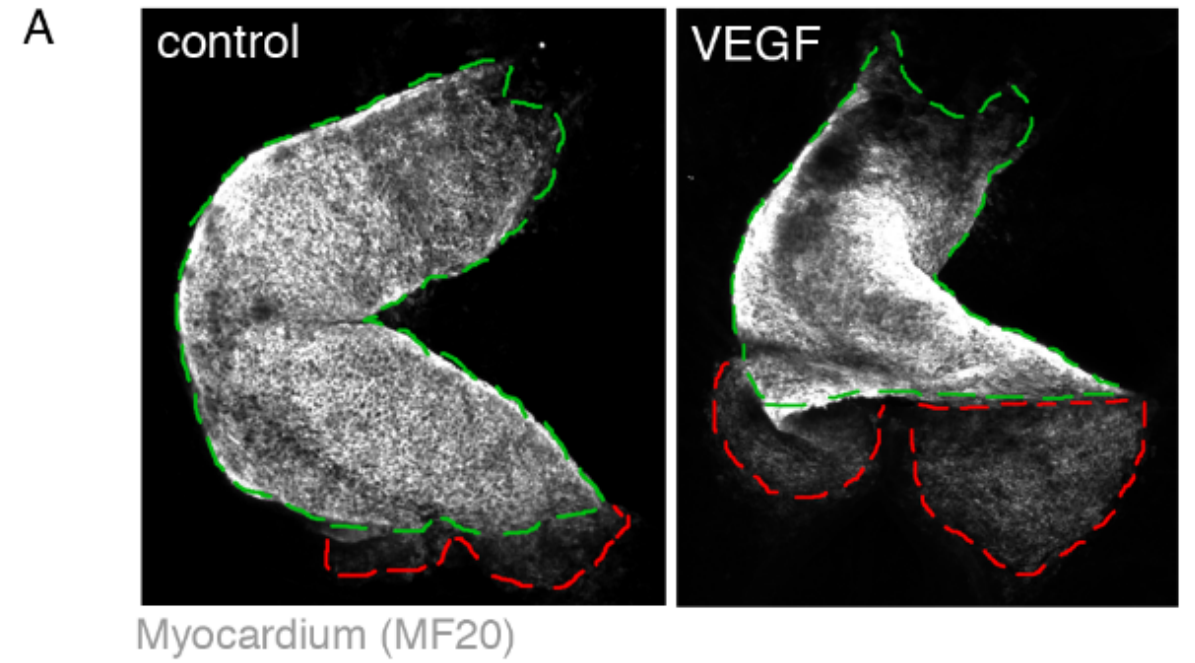
A
control
VEGF
Myocardium (MF20)

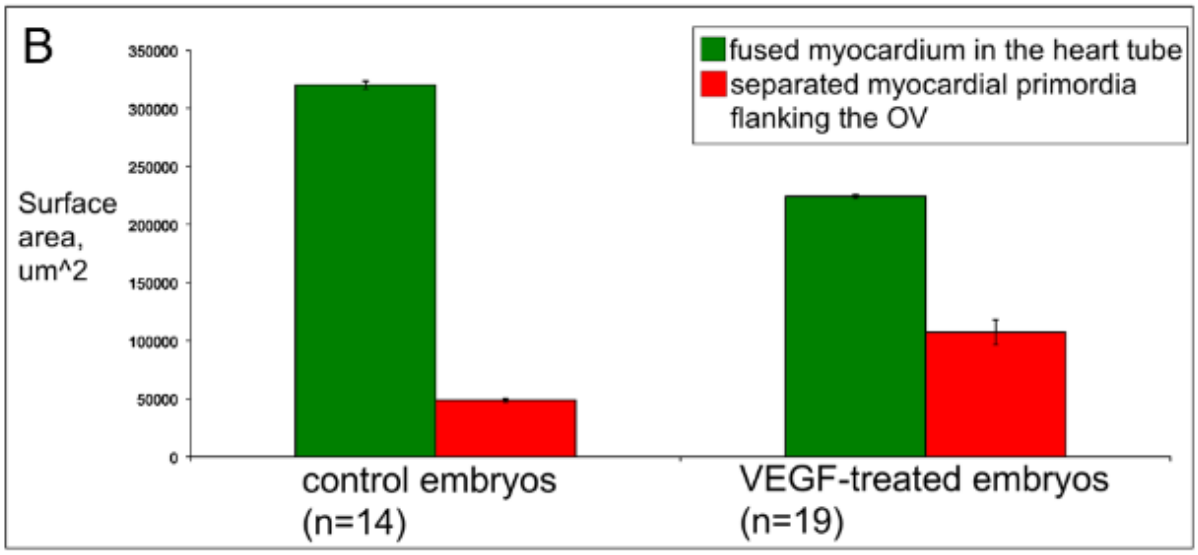
B
fused myocardium in the heart tube
separated myocardial primordia flanking the OV
Surface area, um^2
350000
300000
250000
200000
150000
100000
50000
0
control embryos (n=14)
VEGF-treated embryos (n=19)

Apparent speed of the myocardial progenitor movement towards the midline is decreased by VEGF over-activation

Next, we decided to investigate possible causes leading to the observed decrease in heart tube size in VEGF-treated embryos. In Tie1::H2B-YFP embryos (n=28; four independent experiments) myocardial progenitors were labeled by transfection with the fluorescent reporter plasmid pCMLC2::Mito-RFP as described in *Experimental Procedures.* Fibronectin ECM was labeled in each embryo by microinjection of fluorescently-conjugated antibody B3D6 as in Drake and Little, 2000. Sixteen embryos (16/28) were treated with VEGF, and remaining specimens – with BSA as described above. Post-treatment development was recorded in time lapse for each embryo.

To ask whether VEGF treatment affects myocardial progenitor movements towards the midline during the initial heart tube assembly, we did the following cell tracing experiment. We selected six image sequences out of the twenty-eight described above, three of each of the VEGF-treated and control specimens. In each time-lapse recording, we selected a stationary point, located anterior to the ventral midline (the edge of the buccopharyngeal membrane). Displacements of 10-15 CMLC2::Mito-RFP+ cells in each of the six embryos were traced manually, and the average speed of myocardial progenitor movements during the first five hours post-treatment was calculated separately for control and VEGF-treated specimens (Fig. 4.4.). As seen in

Fig. 4.4, speeds of myocardial progenitor movements decrease over time, but much more rapidly in VEGF-treated embryos.

Figure 4.4: Comparison of myocardial displacement speeds in control and VEGF-treated embryos.

Speeds of myocardial cell displacement during first 5 h following the VEGF or BSA treatment were measured as described in the text and plotted. Error bars: SEM

Figure 4.4

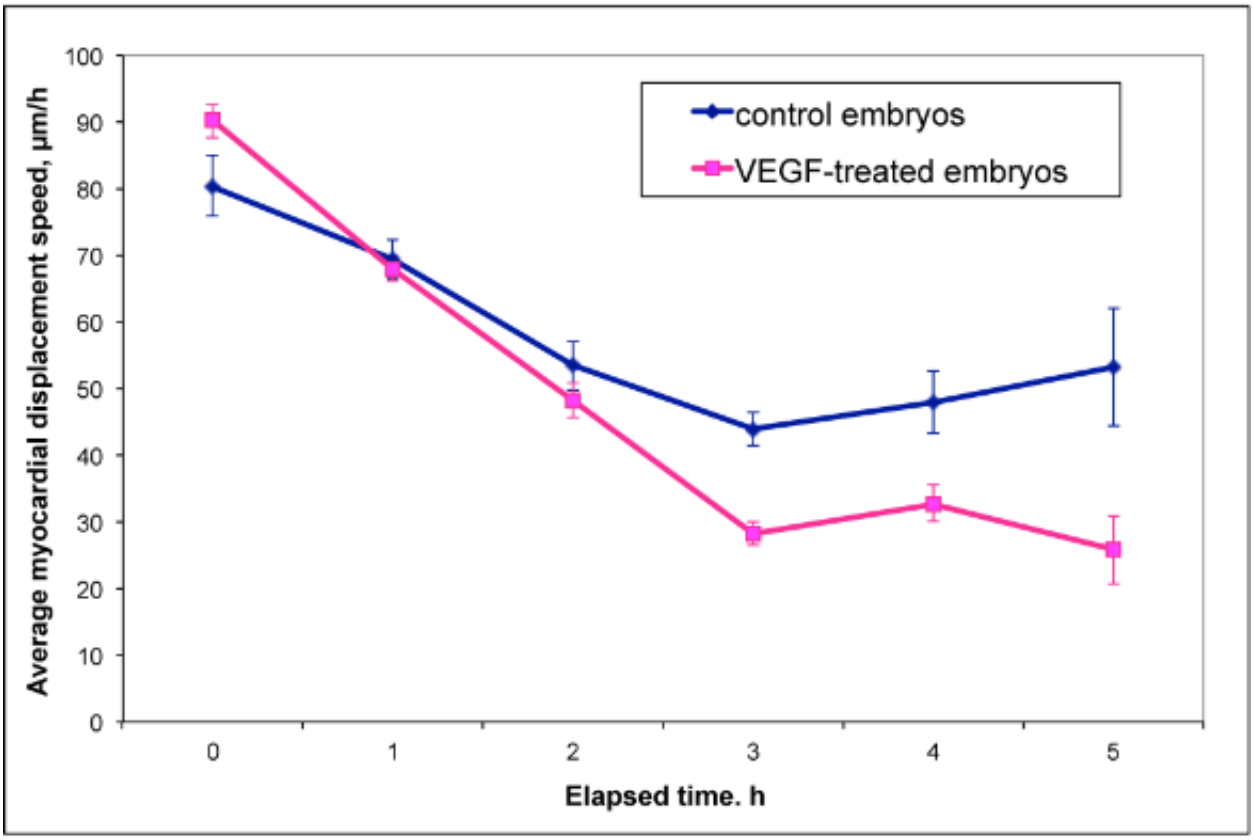
Average myocardial displacement speed, µm/h
100
90
80
70
60
50
40
30
20
10
0
0
1
2
3
4
5
Elapsed time. h
control embryos
VEGF-treated embryos

Myocardial deformations that occur during unperturbed heart tube elongation are impeded in VEGF-treated embryos

As discussed in Chapter 3, prior to their fusion at the midline myocardial progenitor fields change position from ventral to dorso-lateral with respect to the coelomic cavities (see Fig. 3.3B). It is known that cardiac morphogenesis is a sequential process that occurs in an anterior-to-posterior progression (Linask, 2003). I.e., after initial heart tube assembly is complete, the caudal portions of the heart fields undergo the same morphological transitions their anterior counterparts experienced, prior to entering the heart tube. In this way newly differentiated myocardium is added to the heart tube at its posterior aspect, while myocardial progenitors that differentiated earlier already undergo more advanced morphogenesis within the heart tube.

To visualize the deformations within myocardial fields at stages following heart tube assembly, we selected time-lapse sequences that describe the development of control (BSA-treated) specimens between stages HH9-11. Multiple z-plane images for each time point were color-coded to convey the position of cells along the dorso-ventral embryonic axis (with the most ventral plane in red and the most dorsal in blue). In Fig. 4.5A, the positions of three myocardial progenitor cells (marked with arrows of assorted caliber) are traced at advancing time points. Initially located posterior to the heart tube, these cells approached the ventral midline, underwent the change in position with respect to the dorso-ventral embryonic axis, and eventually became incorporated into the heart tube (Fig. 4.5A).

To see if the endothelial/endocardial compartment of the forming heart tube undergoes dorso-ventral displacements similar to those of myocardial primordia, we color-coded the images from time lapse recordings of Tie1::H2B-YFP embryo development at HH10-11. As illustrated in Fig. 4.5B, omphalomesenteric veins are involved in a “rolling forward” movement, with cells at their ventral surfaces being displaced posteriorly, and those at dorsal surfaces – anteriorly in relation to the heart tube position.

In order to investigate if myocardial movements at post-heart tube assembly stages are changed by VEGF treatment, we inspected the time-lapse recordings of control (n=12) versus VEGF-treated (n=16) embryos generated as described at the beginning of the previous section. In most of the control embryos (10/12, 83%), by the end of an approximately 17 h-long imaging experiment, all of the CMLC2::mitoRFP+ cells have entered the heart tube as seen in the left panels of Fig. 4.6. At the same time, in the VEGF- treated group only 6 out of 16 embryos (37.5%) did not have CMLC2::mitoRFP cells outside of the heart tube. The remaining 10/16 VEGF-treated embryos (62.5%) contained reporter-expressing cells in the locations posterior to the heart tube and dorsal to the expanded inflow region (right panels in Fig. 4.6). The location of these cells within separated myocardial primordia (as in Fig. 4.3A) was confirmed by post-fixation MF20 antibody labeling (data not shown).

Figure 4.5. During normal cardiac elongation, myocardial and endocardial compartments of the heart tube progressively undergo ventral displacements ("rotation").

A, B – selected frames from time lapse image sequences describing movements of CMLC2::GFP-expressing myocardial progenitors (A) and Tie1::H2B-YFP-positive endothelial/endocardial progenitors at progressive stages of cardiac tube assembly and elongation. Images were colorcoded to convey the information about the position of displayed objects relative to the dorso-ventral embryonic axis as illustrated by the provided reference bar. Arrows in A point to cells, displacements of which were traced (each type of arrow corresponds to the same cell/group of several cells in every image). Arrows in B illustrate the rotational movement of the omphalomesenteric veins (OV), whereby cells at the dorsal surfaces of the OV are continually displaced anteriorly, and those at the ventral surfaces – posteriorly during HH10 and later stages. Elapsed times from the commencement of image acquisitions are listed in the top left corners of the included images. Scale bars: 100 μm.

Figure 4.5

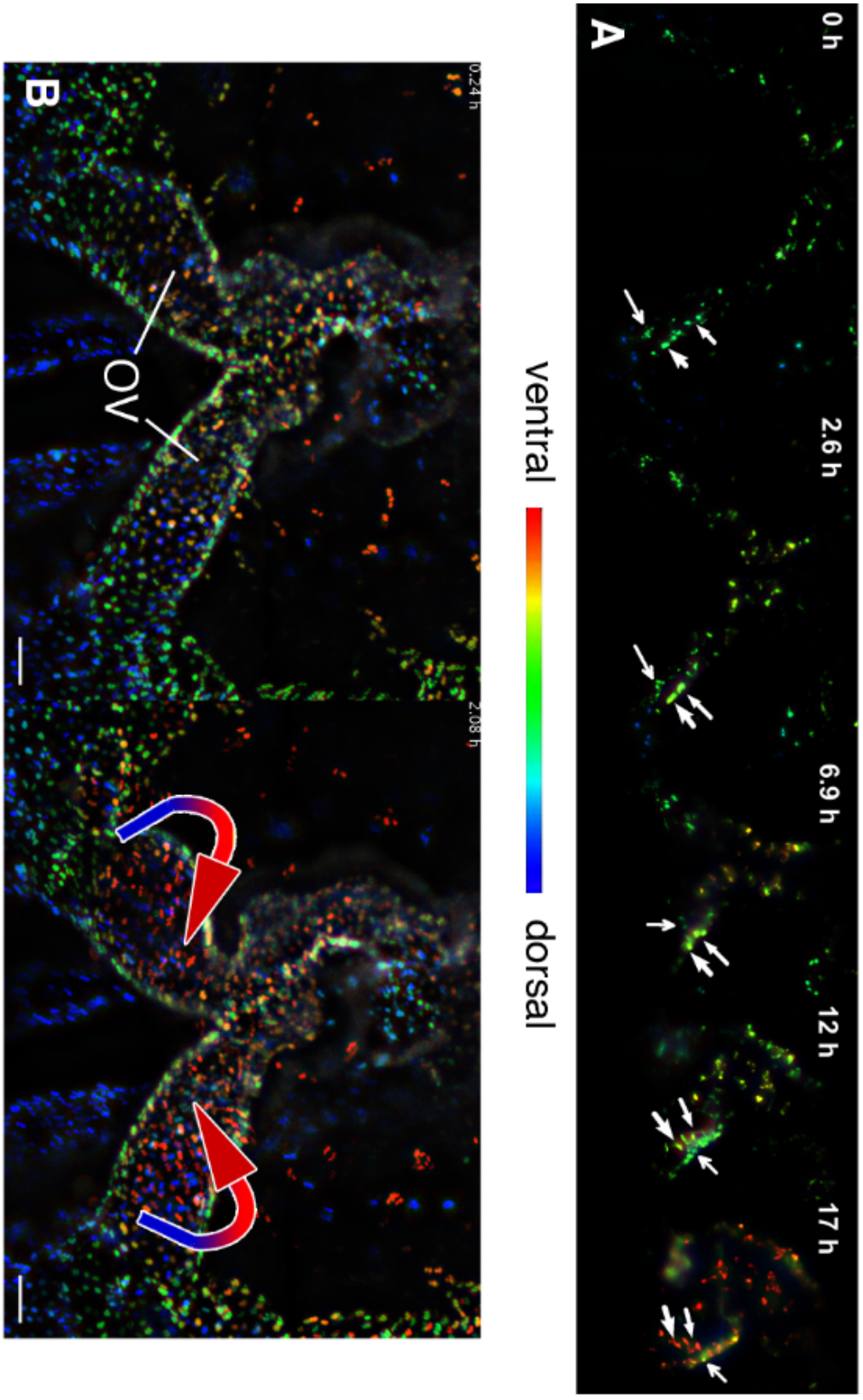

Figure 4.6: Transition of myocardial cells from areas flanking the omphalomesenteric veins into the heart tube proper is delayed in VEGF-treated embryos.

Selected frames from time-lapse image sequences that visualize and compare the development of a control and a VEGF-treated embryo from HH8 to HH12. Both specimens were Tie1::H2B-YFP-transgenic (green labeling), and transfected with CMLC2::MitoRFP reporter (red labeling). CMLC2::MitoRFP-expressing cells were present at the level of the omphalomesenteric veins (OV) in both the control and VEGF-treated embryo at the intermediate stage (8.5 h; groups of cells marked with ellipses). By the end of the imaging experiment, no CMLC2::Mito-RFP+ cells were detected in the OV region of the control embryo (17.1 h; bottom left panel and corresponding inset). At the same time, multiple CMLC2::Mito-RFP+ cells were found in the OV area of the VEGF-treated specimen (bottom right panel and inset). To ensure visualization of cells expressing low levels of CMLC2::Mito-RFP, the contrast of images presented in both insets was enhanced to the same degree by identical methods. Scale bars: 100 μm

Figure 4.6

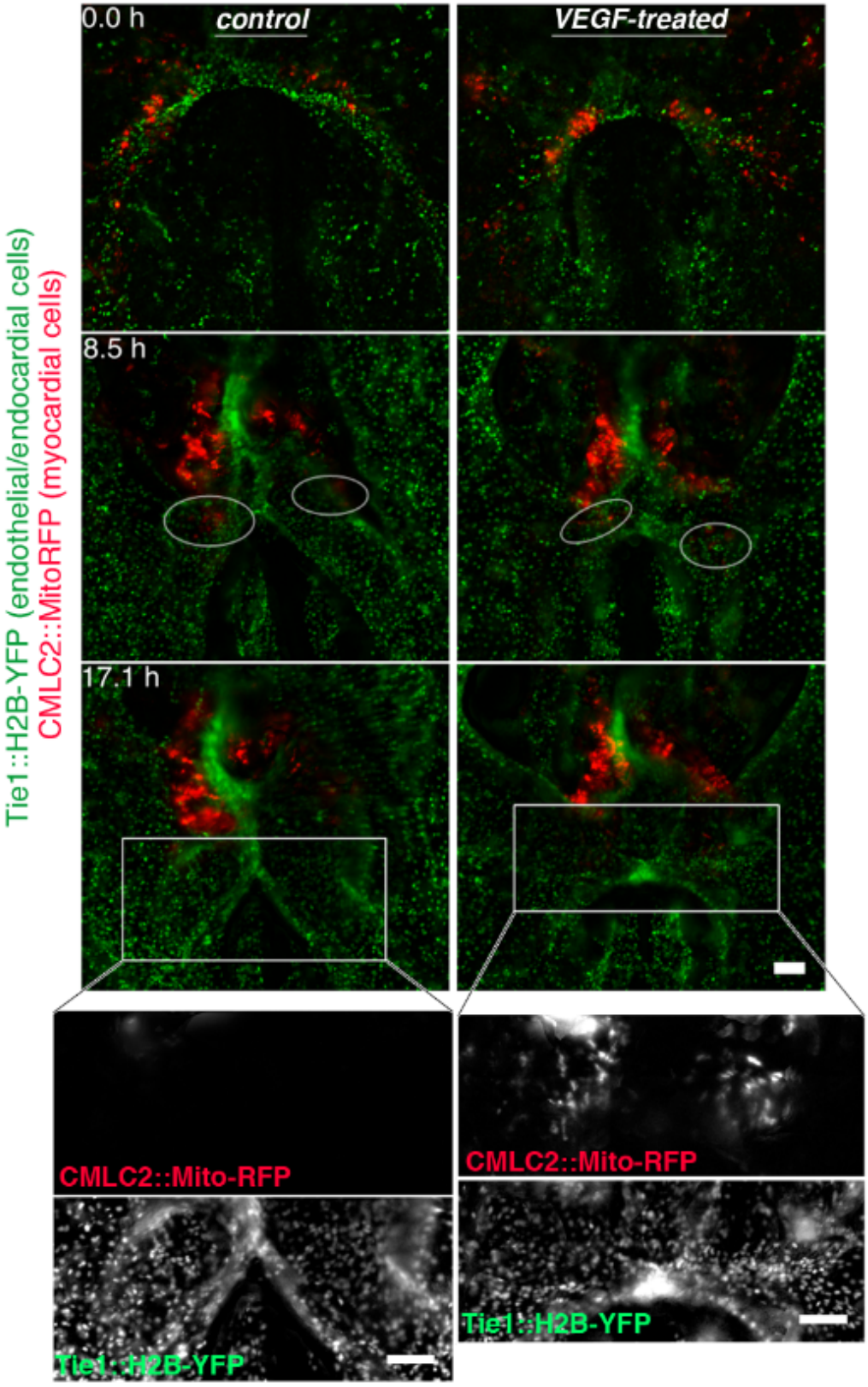
0.0 h
control
VEGF-treated
8.5 h
17.1 h
Tie1::H2B-YFP (endothelial/endocardial cells)
CMLC2::MitoRFP (myocardial cells)
CMLC2::Mito-RFP
Tie1::H2B-YFP
CMLC2::Mito-RFP
Tie1::H2B-YFP

Inhibition of VEGF signaling by the VEGF-R2 inhibitor SU5416 does not affect the initial stages of heart tube assembly and elongation

Twenty-two wild type quail embryos at HH8 were isolated. Twelve of them were treated with SU5416 (Tocris Biosciences) at 1 and 2 mM concentrations (6 embryos each) as described in *Experimental Procedures.* The remaining 10 specimens were treated with the same volume of DMSO in PBS. Groups of embryos were fixed after 4, 7, and 12 h of post-treatment incubation. Endothelial and myocardial cells, as well as fibronectin ECM, were labeled with antibodies as described above. As seen in Fig. 4.7A, myocardial positions and morphology remained relatively unaffected by SU5416 treatment at all the time-points examined. At the same time, SU5416 effectively reduced endothelial/endocardial cell numbers in treated specimens compared to the controls (note the virtual absence of the endocardium in the SU5416-treated embryo shown in transverse section in Fig. 4.7B).

Figure 4.7: Analysis of effects of SU5416-mediated VEGF signaling inhibition on heart tube assembly and early elongation.

A – confocal images representing embryos fixed after 4, 7, and 12 h of incubation with 1 mM SU5416 (right panels) or DMSO (control; left panels). Embryos were stained with MF20 to label myocardium (red staining), QH1 to visualize endothelium/endocardium (green), and B3D6 to label fibronectin ECM (blue). Note decreased numbers of endothelial/endocardial cells in SU5416-treated embryos. Myocardial morphology is similar in both groups at all three time points included in the analysis. Scale bars: 100 μm.

B – transverse sections through the control and SU5416-treated embryo (both HH12) at the level of the heart tube. The endocardium is represented by a continuous epithelial layer in a control embryo (left panel), but is reduced to small cell aggregates in the SU5416-treated embryo (right panel). E – endocardium, M - myocardium.

Figure 4.7

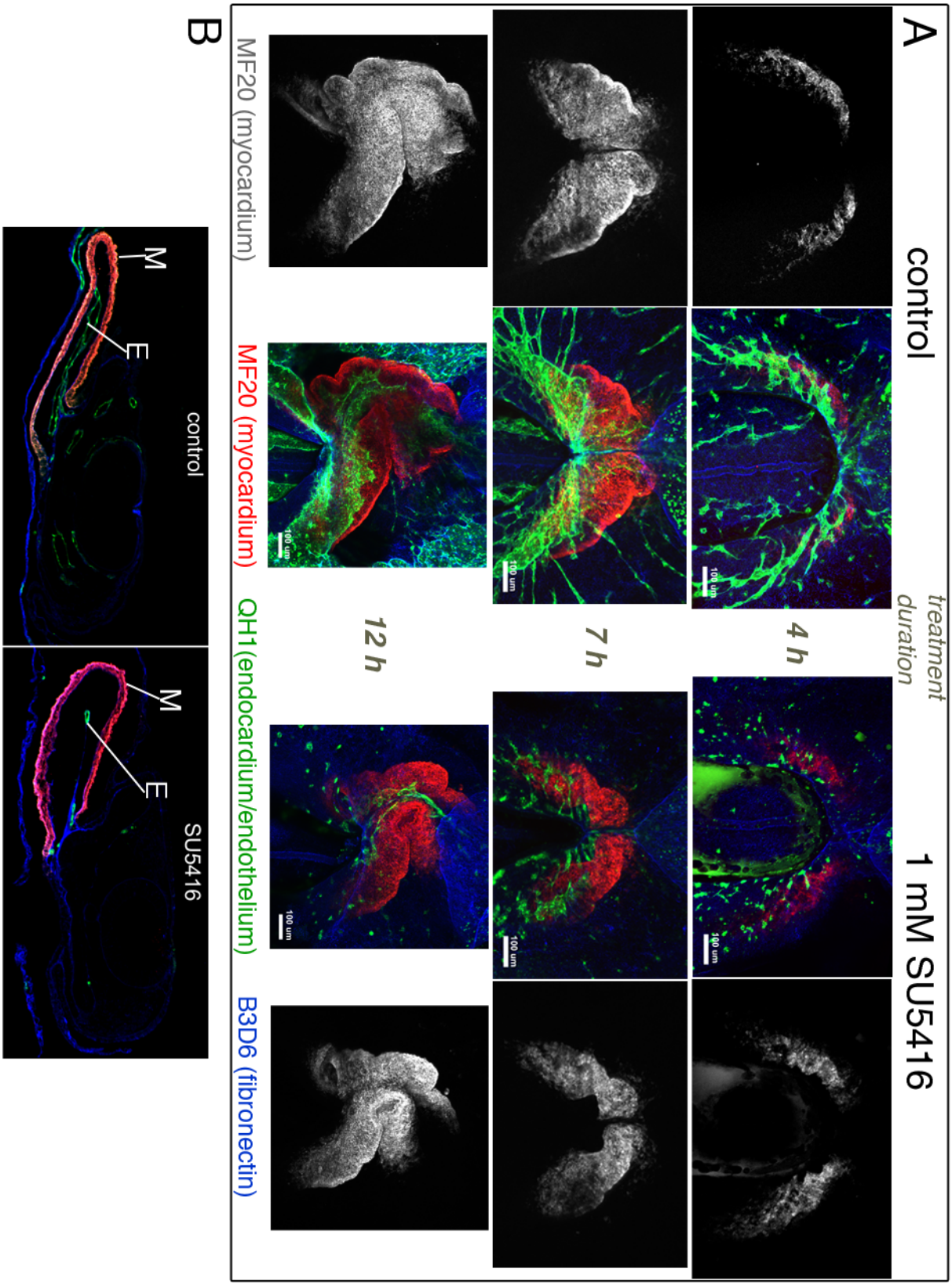
A
control
1 mM SU5416
treatment duration
4 h
7 h
12 h
MF20 (myocardium)
MF20 (myocardium)
QH1 (endocardium/endothelium)
B3D6 (fibronectin)
100 um
B
control
SU5416
M
E
M
E

Perturbations of endogenous VEGF signaling levels do not affect the speed of AIP regression

AIP regression is one of the major forces driving the cardiac progenitor movements during tubular heart assembly (see Chapters 2 and 3, Varner et al., 2012). Therefore, we decided to examine if AIP regression speed in HH8-11 quail embryos is affected by exposure to rhVEGF165 or SU5416 treatment. The position of the center of the AIP arch and the first somite borders (see Fig. 3.11A for illustration) were traced manually in DIC time-lapse recordings of control embryos (n=6) or embryos developing in the presence of rhVEGF165 (n=5) and SU5416 (n=3). All treatments were set up as described above. Tracing data were then used to calculate the speeds of foregut elongation at three arbitrarily selected regions (time intervals) within the linear AIP regression trajectory (illustrated in Fig. 3.11A). The results summarized in Fig 4.8 demonstrate that neither rhVEGF165 nor SU5416 treatment affected the AIP regression speed at any of the time periods examined.

Figure 4.8: Analysis of the effects of VEGF and SU5416 treatments on the speed of AIP regression.

The bar chart illustrates mean speeds of AIP regression at the early, intermediate, and late portions of the trajectory (see Fig. 3.11A for explanation), measured in control (green bars), VEGF- (red bars), and SU5416-treated (blue bars) embryos. Error bars: SEM.

Figure 4.8

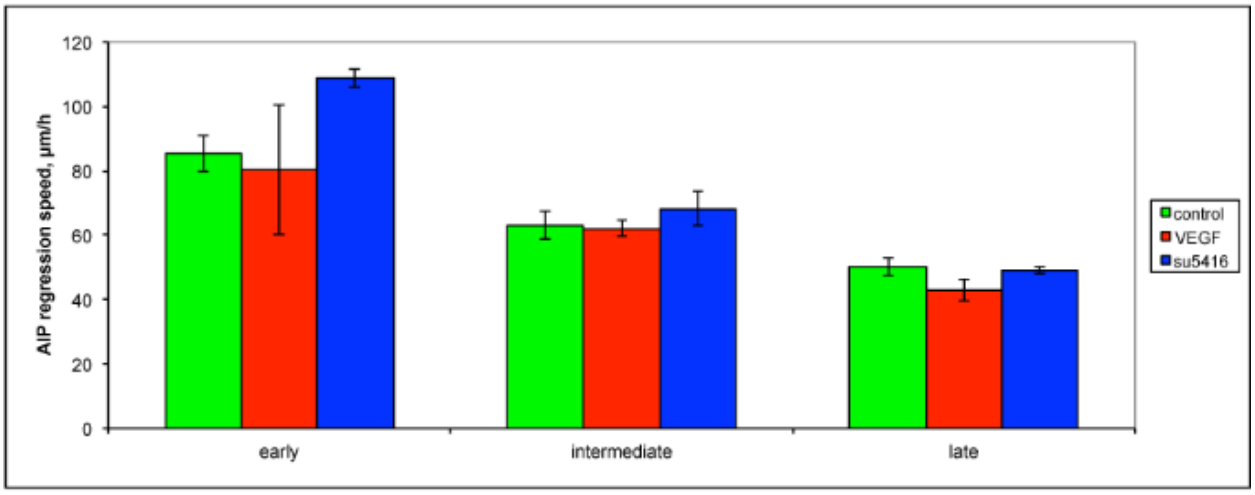
AIP regression speed, µm/h
120
100
80
60
40
20
0
early
intermediate
late
control
VEGF
su5416

Discussion

VEGF is a well-known regulator of angiogenesis and vasculogenesis, endocardial cushion formation, and other aspects of cardiovascular development (Achen and Stacker, 1998; Ferrara, 2000) and participates in the growing list of processes and developmental events that involve non-endothelial cell lineages (reviewed in Haigh, 2008). In our study we focused on effects of VEGF overexposure on dynamic events that underlie heart tube assembly and early elongation in avian embryos.

Recombinant human VEGF165 was used by several groups to upregulate VEGF signaling and assess induced effects on vascular and cardiac development (Drake and Little, 1995; Feucht et al., 1997; Drake et al., 2006). In a study directly relevant to ours, Drake et al. (2006) demonstrated that injection of 25-50 ng of rhVEGF165 into quail hearts resulted in abnormal endocardial development, leading to the formation of separated folds and cords within this cell layer. Also, the authors reported that if VEGF overexposure was induced in HH9 (8-9 somites) quail embryos, defects in cardiac tube bending ensued, a phenotype not developed if younger (6-7 somites) embryos were treated. In comparison to the above study, our experiments were performed using higher (5-10 fold) concentrations of rhVEGF, and were targeted towards younger embryos (HH8, 4-7 somites). We were able to reproduce the endocardial phenotype reported by Drake at all. (Figs. 4.1B, 4.2B), and similarly, did not detect defects in heart tube bending in embryos treated prior to HH9.

Interestingly, we found that VEGF overexposure led to a 30% reduction in the heart tube size in treated embryos compared to the controls (Fig. 4.3). Since this occurred in parallel with the increased extracardiac presence of MF20+ myocardial cells (Fig. 4.2 and 4.3), which are delayed from entering the heart tube after their arrival at the midline (Fig. 4.6), we favor a model where the effect of VEGF on myocardial movements is secondary to its effect on the inflow region and omphalomesenteric vein diameter.

Alternatively, one could propose a direct negative role for VEGF in regulating myocardial movements, whereby the signal would be received and processed by receptors on progenitor cell membranes. Albeit a logical possibility to consider, this mechanism would require the expression of FLK1 receptor by myocardial progenitors. Published evidence suggests that myocardial cells express only very low levels of FLK1 in chick (Sugishita et al., 2000). Instead, myocardiocytes express and secrete VEGF ligand isoforms in the developing heart (Miquerol et al., 1999; Dor et al., 2001).

Another potential mechanism that could account for the reduction in the heart tube length in response to VEGF could involve a VEGF-dependent depletion of the mesodermal progenitor pool (from which myocardial progenitors arise) to favor the differentiation of endothelial/endocardial cells. This scenario is unlikely, because it has been shown that in avian models myocardial and endocardial lineages segregate and become committed to a particular fate very early in development, namely within the early (HH3) primitive streak (Mikawa and Gourdie, 1996; Wei and Mikawa, 2000), at least 10-12 h prior to our chosen time of VEGF treatment administration.

One intriguing aspect of the phenotype we observe in response to VEGF overexposure is that despite induced hyperfusion of embryonic vessels (Drake and Little, 1995), the two omphalomesenteric veins remain separated in treated embryo as seen, for instance, in Fig. 4.2B. In transverse sections through the VEGF-treated specimens one can see the omphalomesenteric veins juxtaposed 300-900 μm distances, yet not connected (data not shown). Voronov et al (2004) measured stresses in the vicinity of the forming heart tube during normal development, and found that fusing OV experience compression prior to fusing and thus contributing to the inflow region in HH10 embryos. Taking into account our observations and the above published evidence it seems possible that the myocardial deformations in the vicinity of the inflow would serve to facilitate omphalomesenteric vein remodeling into a single endocardial tube by physically "pushing them together". This process is clearly disrupted in VEGF-treated embryos, making such remodeling impossible despite an over-abundance of the vascular fusion-promoting signal.

Without a doubt, additional studies are required to achieve a more comprehensive understanding of the cellular and tissue events that underlie the dramatic changes in cardiovascular development induced by VEGF overexposure. In our ongoing and future studies, we are planning to use our existing imaging data to evaluate ECM fibril displacements, and speeds of endocardial and myocardial progenitors movement relative to the ECM, as we did for unperturbed embryos in Chapters 2 and 3. Quite unexpectedly, in our current study we found that VEGF treatment does not affect the regression of the AIP (Fig. 4.8). Given the primary

importance of this massive tissue folding event in driving the movements of ECM, endocardial and myocardial progenitors to the embryonic midline (see Chapters 2 and 3), we are intrigued to investigate if the speed of coordinated displacement of the ECM and cardiac progenitors (tissue movement) is affected by VEGF, independently of the AIP regression.

Additionally, we are planning to assess the effects of VEGF signaling inhibition (using several chemical blockers of VEGF-R2 tyrosine kinase function) on myocardial progenitor and ECM displacements during early heart tube assembly and elongation in time lapse, to complement our existing data, obtained in static culture time-course experiments (Fig. 4.7). We expect the speeds of myocardial progenitor displacements towards the midline to be comparable with those measured in unperturbed embryos. As far as similar situations in other model systems are concerned, it is known that in the zebrafish endocardium-less mutant *cloche*, myocardial progenitors are able to reach the ventral midline (Stainier et al., 1995).

CHAPTER FIVE:

Conclusions and future directions

Formation of the cardiac tube is the first organogenesis step in development, as the heart is the first organ to assemble and become functional in a vertebrate embryo. Despite being an extremely complex process, cardiac tube morphogenesis can be viewed from a standpoint of interaction between four participating tissue elements – the endocardium and myocardium, contributing two principal cellular layers of the early heart, and the endoderm and extracellular matrix, that were for a long time considered to provide an environment (substrate) for cardiac progenitor movements. Until recently, the endoderm was prescribed a predominantly signaling role in cardiogenesis (Lough and Sugi, 2000; Alsan and Schultheiss, 2002; Warkman et al., 2008). The extracellular matrix of the developing heart has many known functions and is represented by a variety of molecules (Bowers and Boudino, 2010). Among those, fibronectin clearly plays one of the central roles during heart tube assembly (Linask and Lash, 1986; Linask and Lash, 1988a; Linask and Lash, 1988b; Wiens et al., 1996; George et al., 1997; Trinh and Stainier, 2004; Arrington and Yost, 2009).

From studies on multiple vertebrate and invertebrate model organisms, a large amount of information is available about molecular signaling that acts during early heart morphogenesis (van Wijk et al., 2007; Wagner and Siddiqui, 2007; Gessert and Kuhl, 2010); transcriptional and epigenetic regulation programs, activated in differentiating endocardial and myocardial progenitors (Cripps and Olson, 2002; van Weerd et al., 2011; Lopez-Sanchez and Garcia-Martinez, 2011; Ohtani and Dimmeler, 2011); and single gene mutations that lead to defects in early heart tube formation in vertebrates (Kawahara et al., 2009; Matsui et al., 2007; Sakaguchi et al., 2006; Li et al., 2004). At

the same time, the question remains how cardiac progenitors facilitate large-scale tissue rearrangements during their morphogenetic movements.

As shown in a number of recent studies by our group and others (Sepich et al., 2005; Zamir et al., 2006; Zamir et al., 2008; Szabo et al., 2011; Aleksandrova et al., 2012), movements of embryonic cell populations at different stages of embryonic development result from a combination of displacements in a manner correlated with the surrounding tissue environment ("tissue motion"), and those relative to it ("active movement"). The question is often asked as to the driving forces of tissue motion (Chuai and Weijer, 2009). Our results (Chapters 2 and 3) point to the regression of the AIP in combination with the coordinated deformation of myocardial progenitor fields as the most likely drivers of tissue movement in the vicinity of the developing heart tube.

In Chapter 2, we present evidence for transfer of preassembled ECM fibrils from their initial locations within the precardiac mesoderm to the target positions within the heart tube, by tissue motion. Given the ability of ECM to specifically interact with morphogenetic factors (Hynes, Science 2009), this finding could have implications for our understanding of how morphogen signaling gradients are set and maintained within the precardiac mesoderm and, subsequently, the heart tube. Recently, Milgrom-Hoffman et al. (2011) provided evidence that endocardial cells derive from vascular endothelium in the mouse embryo. Similarly, in quail, we see that the proximity to the AIP defines the fate of a given cell as endocardial or endothelial. Further, passive objects (latex beads), positioned in locations subject to the midline-directed tissue movement, are similarly able to enter the heart tube.

Despite all the literature postulating that cardiac progenitor movements to the midline occur relative to the fibronectin ECM and/or the endoderm, our study is unique in our attempt to visualize the said movements *in vivo* using specific ECM and cardiac progenitor labeling strategies, and to quantitatively assess the relative motion speed and directions. In 1963, deHaan used iron particles to mark the endoderm in chick and subjected the embryos to “time-lapse cinematography”. Of interest, the conclusions of the study (although concerning earlier, HH5-7, stages of development) stated that the myocardium moves anteriorly (“cephalically”) relative to the endoderm.

The data presented in Chapter 3 was used to develop a subcellular element-based model that, even at this early stage, is able to describe myocardial movements rather faithfully (Figs. 3.7-9). The model will be further refined to account for the observed contraction (shortening) of the medial myocardial field aspects, deforming influence of the AIP regression, etc. The modeling approach illustrated here is significantly different from that used by Varner et al. (2012), and potentially can be used for a wider range of applications. Instead of being based on a single bended contractile beam, our model represents both the anatomy of the myocardium and the surrounding mesoderm, as well as the specific mechanical activity (bending and spatially restricted contraction) we suggest for the myocardium. Model simulations then allow us to explore the tissue scale consequences of the assumed myocardial behavior. Thus, our mechanical model also allows us to establish a connection between the tissue and cell-level behaviors.

The model of myocardial field movements that implies coordinated deformation of progenitor fields would allow the explanation of multiple observations by our group and others. Further, we believe that the “active” (deformation-driven) myocardial movements might contribute to the convective tissue motion that is, in turn, responsible for the bulk of the endocardial progenitor movements (discussed in Chapter 2). However, the degree of this contribution is likely to be secondary to that of the AIP regression/foregut elongation. It is logical because endocardial progenitors are embedded within the ECM (Fig. 2.1; Linask and Lash, 1993) that separates the myocardium and the endoderm – an ECM layer myocardial cells move relative to.

The mechanisms responsible for myocardial sheet folding (bending) need to be investigated as an intriguing continuation of this study. Cellular morphologies within the cup-shaped bend do not suggest a possibility for “classic” wedge-shaped cell-driven bending to occur in this situation (Sawyer et al., 2010). However, myocardial cells may present a case whereby very subtle change of cell shape in each individual cell (like that observed for endodermal cells in *C. elegans,* which undergo internalization as a result of very mild apical constriction; Lee et al., 2006) may lead cumulatively to a pronounced bending of a sheet.

Coordinated cell shape changes, exhibited by myocardial cells, have been described in cardiac morphogenesis in zebrafish. The study by Auman et al. (2007) demonstrated that regionally confined cell shape changes underlie the emergence of ventricular chamber curvatures in the developing heart. In chick, early work by Manasek

et al. (1972) proposes myocardial cell shape change as a potential mechanism for cardiac looping.

A potential mechanism that could contribute to the observed dorsal bending of the myocardial progenitor fields may involve gradual accumulation of the glycosaminoglycan molecules between myocardium and the underlying endoderm, able to attract water and create an internal pressure within the tissue. De Jong et al. (1990) stated that precardiac mesoderm secretes ECM components that “inflate” the myocardial epithelium. Nakamura and Manasek (1981) demonstrated that treatment of early heart tubes with hyaluronidase causes them to deflate due to the loss of the cardiac jelly volume. Glycosaminoglycan hyaluronan is a major constituent of the ECM in the developing heart (Orkin and Toole, 1978), important for various aspects of morphogenesis such as early heart valve development (Markwald et al., 1975, 1977; Lagendijk et al., 2011). It is produced by both endocardium and myocardium beginning at the stages immediately preceding heart tube formation (Orkin and Toole, 1978). Hyaluronan accumulation was shown to propel epithelial displacement during inner ear formation in *Xenopus* (Haddon and Lewis, 1991). Furthermore, in gastrulating sea urchin embryos localized deposition of ECM with its subsequent hydration (expansion) was proposed to drive epithelial sheet bending and invagination underlying archenteron formation (Lane et al., 1993).

Given the above examples of ECM-driven tissue deformations it would be both interesting and necessary to investigate the effects of the loss of hyaluronan (via hyaluronidase treatment) on myocardial curling and convective tissue movements.

However, treatment of developing embryos with hyaluronidase failed to inhibit cardiac looping - another tissue deformation-driven event in cardiac morphogenesis (Baldwin and Solursh, 1989; Linask et al., 2003). Further, mouse deficient for hyaluronan synthase Has-2 were able to develop heart tubes, but exhibited multiple cardiac defects, including abnormally thin myocardium, at the time of their death at E10.5 (Camenisch et al., 2000). In our experiments to date, we found a wide variety of cardiac jelly volumes associated with very similarly deformed myocardial primordia in transverse sections of embryos subjected to lateral incisions (as Fig. 3.6E).

Our results on directionality and magnitudes of the convective tissue movements, presented in Chapters 2 and 3, lend support to the conclusions of Varner et al. (2012) on the primary role of the endoderm in bringing the heart fields to the midline. Quantitative data obtained in this study confirm that speeds of the midline-directed movement of both types of cardiac progenitors, as well as of the two prominent ECM constituents (fibronectin and fibrillin-2; summarized in Fig. 3.1C) is coordinated with the AIP regression speed in unperturbed embryos (Figs. 3.11B and 4.8). Consequently, in order to understand the driving force of early cardiogenesis, the field needs to decipher molecular, cellular, and tissue mechanisms responsible for AIP regression. So far, available information is rather scarce. It is known that a KRAB zinc finger transcription factor Chato, a known regulator of convergence-extension movements in all three germ layers, plays roles in the endoderm elongation and gut closure in mice (Garcia-Garcia et al., 2008). Recently, an important part in controlling early foregut morphogenesis had been assigned to the atypical Rho GTPase Rhou, implicated in regulating epithelial

architecture within the developing endoderm (Loebel et al., 2011).

Our results in Chapter 3 suggest an attractive possibility that endoderm contractility at the AIP can be influenced by the adjacent mesoderm. As seen in Fig. 3.11E, a myocardial-specific expression of the constitutively active form of Rho produces a small but statistically significant decrease in the AIP regression speed compared to GFP-transfected controls in quail embryos. The endoderm and mesoderm are coupled through the pronounced ECM layer (Figs. 3.1A, 3.5), and tissue deformations indicative of contraction are evident within the mesodermal layer (Figs. 3.3 and 3.4). At the same time, careful inspection of our imaging records of MitoTracker-labeled embryo (such as those presented in Fig. 3.2) failed to reveal evidence of similar cell shape changes within the endoderm. It is possible that such a small effect of Rho disruption is due to the low transfection efficiency in our experiments, which we estimate to rarely exceed 10% of the total myocardial population. To further dissect the roles of myocardial contraction in AIP regression, one could attempt myocardial-specific expression of dominant negative and constitutively active isoforms of other known regulators of actin-based motility and cell shape regulation, such as the GTPases Rac and Cdc42, Rho kinase (ROCK) and others. Another way to introduce mechanical discontinuity into the cohesive myocardial sheet would be to induce controlled cell death within a subset of cells using any of the conventional strategies, such as tissue-specific expression of a herpes virus thymidine kinase (Su et al., 1997; Vile and Hart, 1993), diphtheria toxin (Harrison et al., 1991; Saita et al., 2001) or constitutively active caspase 3 (Condorelli et al., 2001).

Gene expression studies indicate that the AIP has a unique gene expression signature compared to the adjacent endodermal tissue. For instance Fgf8 is expressed by the endoderm in the narrow stripe that corresponds to the position of the AIP (Streit and Stern, 1999; Bailey et al., 2006; Lopez-Sanchez et al., 2009). Stalsberg and DeHaan (1968) demonstrated that endoderm is "rolling over" the AIP into the developing gut. This makes this endodermal structure functionally similar to the primitive streak – a site where cells become transiently, "in passing", exposed to a variety of molecular signals (Mikawa et al., 2004).

Without a doubt, live imaging studies can contribute a great deal of valuable information to the understanding of cell rearrangements at the AIP. In our preliminary experiments we were able to detect some differential movements within the MitoTracker-labeled endoderm (Aleksandrova et al., unpublished). However, the light-sensitive nature of MitoTracker and some other similar dyes we tested does not allow imaging with sufficient frame rate for a long enough time period to provide all the needed information on cellular repositioning at the AIP. Hopefully in the near future new transgenic strains of chick or quail with endoderm-specific reporter expression will be created, providing as valuable a tool for understanding endoderm morphogenesis, as the Tie1::H2B-YFP quail strain (Sato et al., 2010) has been for vascular endothelial/endocardial biology.

Another open question of tremendous importance is that of the molecular signaling regulators of the tissue deformation processes responsible for heart morphogenesis. Developing myocardial progenitors are exposed to signaling by Fgf

and Bmp family members (Lough and Sugi, 1995). Both pathways have known roles in cell shape regulation in other developmental processes. Fgf signaling was implicated in regulating apical constriction in zebrafish (Harding and Nechiporuk, 2012). Bmp/SMAD signaling was shown to be involved in cell shape transition from columnar to squamous during inner ear development (Ohta et al., 2010).

Thus, it would be interesting to determine if known morphogen regulators of cardiac differentiation may also play previously unappreciated roles in tissue deformations/convective tissue movements in the anterior embryo. In Chapter 4 we create a situation where VEGF (a specific “endothelial” mitogen and morphogenetic factor; Leung et al., 1989) is used to drive a dramatic increase of the inflow region/omphalomesenteric vein diameter. This change does not affect the speed of AIP regression, but decreases myocardial progenitor movement speeds and abrogates myocardial deformations at the stages following initial heart tube assembly, collectively resulting in a pronounced reduction of the heart tube size. This combination of effects creates a valuable system to investigate the impacts of each of the driving forces of tissue movement acting in the vicinity of cardiogenic fields. Also, by altering the quantity of VEGF delivered to the developing embryo, the severity of inflow dilation can be modulated and the invoked effects on tissue movement similarly dissected. Thus, continued analyses of VEGF-treated embryos will provide new insights as to the effects of VEGF over-activation on tissue motion. We expect to be able to prescribe the mechanical barrier supplied by the enlarged inflow region in our computational model, and investigate the outcomes of such perturbation on model behavior. Similar

experimental and modeling approaches can be applied to studying the effects of other known regulators of cardiogenesis on endocardial and myocardial progenitor cell motility and tissue deformations within the anterior embryo.

Coordinated deformations continue to occur after initial heart tube formation in differentiating myocardial primordial, which progressively incorporate into the growing organ (Fig. 4.5). This may have interesting implications with regards to another critical step of cardiogenesis, namely cardiac looping. Cardiac looping initiates as soon as the early heart tube is established at the midline (HH10; Manner et al., 2000) and involves the transformation of a straight linear organ, attached to the foregut throughout its length, into a C-shaped structure, which is bent towards the right side of the embryo during normal development. This early event is followed by further bending deformations of the developing heart, and in combination with later-occurring septation processes is involved in advanced chamber morphogenesis. A large body of work defines two steps within the C-looping process, whereby it results from a combination of ventral bending and rightward rotation (Manner et al., 2000; Voronov et al., 2004; Taber et al., 2010). Interestingly, out of these two events ventral bending appears to be driven by the processes intrinsic to the heart tube, as suggested by Manning and McLahlan (1990) and confirmed by more recent studies (Latacha et al., 2005; see Taber, 2006 for review). It would be extremely interesting to investigate if, and how, the forces contributed by uniform contraction and dorsal bending of the myocardial field contribute to the heart tube bending and/or rotation.

Collectively, the results presented in this dissertation revealed some previously unappreciated aspects of endocardial and cardiac jelly morphogenesis, offered new information on tissue mechanisms of myocardial progenitor displacements, and established a link between the balanced presence of all early heart constituents, appropriate tissue deformations in the anterior embryo, and success of early heart formation and elongation. We are certain that exploration of new avenues based on and emerging from our research will provide further insights into the biomechanical mechanisms of cardiac morphogenesis.

CHAPTER SIX:

References

Abu-Issa R, Kirby ML. (2007). Heart field: from mesoderm to heart tube. *Annu Rev Cell Dev Biol*. **23**, 45-68.

Abu-Issa R, Kirby ML. (2008). Patterning of the heart field in the chick. *Dev Biol.* **319**, 223-33.

Achen MG, Stacker SA. (1998). The vascular endothelial growth factor family; proteins which guide the development of the vasculature. *Int J Exp Pathol*. **79**, 255-65.

Aleksandrova A, Czirók A, Szabó A, Filla MB, Hossain MJ, Whelan PF, Lansford R, Rongish B. (2012). Convective tissue movements play a major role in avian endocardial morphogenesis. *Dev Biol*. **363**, 348-61.

Alexander J, Stainier DYR. (1999). Mutations affecting cardiac development in zebrafish. In *Heart Development* (ed. R. P. Harvey and N. Rosenthal), pp. 91-110. San Diego, London, Boston, New York, Sydney, Tokyo, Toronto: Academic Press.

Alsan BH, Schultheiss TM. (2002). Regulation of avian cardiogenesis by Fgf8 signaling. *Development*. **129**, 1935-43.

Argraves WS. (2001). Fibulin-1 suppression of fibronectin-regulated cell adhesion and motility. *J Cell Sci.* **114**, 4587-98.

Argüello C, de la Cruz MV, Gómez CS. (1975). Experimental study of the formation of the heart tube in the chick embryo. *J Embryol Exp Morphol.* **33**(1):1-11.

Armstrong EJ, Bischoff J. (2004). Heart valve development: endothelial cell signaling and differentiation. *Circ Res.* **95**, 459-70.

Arrington CB, Yost HJ. (2009). Extra-embryonic syndecan 2 regulates organ primordia migration and fibrillogenesis throughout the zebrafish embryo. *Development*. **136**, 3143-52.

Ashikari-Hada S, Habuchi H, Sugaya N, Kobayashi T, Kimata K. (2009). Specific inhibition of FGF-2 signaling with 2-O-sulfated octasaccharides of heparan sulfate. *Glycobiology.* **19**, 644-54.

Auman HJ, Coleman H, Riley HE, Olale F, Tsai HJ, Yelon D. (2007). Functional modulation of cardiac form through regionally confined cell shape changes. *PLoS Biol.* **5**(3):e53.

Bader D, Masaki T, Fischman DA. (1982). Immunochemical analysis of myosin heavy chain during avian myogenesis in vivo and in vitro. *J Cell Biol*. **95**, 763-70.

Bailey AP, Bhattacharyya S, Bronner-Fraser M, Streit A. (2006). Lens specification is the ground state of all sensory placodes, from which FGF promotes olfactory identity. *Dev Cell*. **11**, 505-17.

Baldwin HS, Solursh M. (1989). Degradation of hyaluronic acid does not prevent looping of the mammalian heart in situ. *Dev Biol*. **136**, 555-9.

Bellairs R, Osmond M. Atlas of Chick Development. 2nd ed. Academic Press, 2005.

Bénazéraf B, Francois P, Baker RE, Denans N, Little CD, Pourquié O. (2010). A random cell motility gradient downstream of FGF controls elongation of an amniote embryo. *Nature*. **466**(7303):248-52.

Benjamin LE, Golijanin D, Itin A, Pode D, Keshet E. (1999). Selective ablation of immature blood vessels in established human tumors follows vascular endothelial growth factor withdrawal. *J Clin Invest*. **103**, 159-65.

Bowers SL, Baudino TA. (2010). Laying the groundwork for growth: Cell-cell and cell-ECM interactions in cardiovascular development. *Birth Defects Res C Embryo Today*. **90**(1):1-7.

Brutsaert DL, Andries LJ. (1992). The endocardial endothelium. *Am J Physiol.* **263**, H985-1002.

Bussmann J, Bakkers J, Schulte-Merker S. (2007). Early endocardial morphogenesis requires Scl/Tal1. *PloS Genet*. **3**, e140.

Camenisch TD, Spicer AP, Brehm-Gibson T, Biesterfeldt J, Augustine ML, Calabro A Jr, Kubalak S, Klewer SE, McDonald JA. (2000). Disruption of hyaluronan synthase-2 abrogates normal cardiac morphogenesis and hyaluronan-mediated transformation of epithelium to mesenchyme. *J Clin Invest*. **106**, 349-60.

Carmeliet P, Ferreira V, Breier G, Pollefeyt S, Kieckens L, Gertsenstein M, Fahrig M, Vandenhoeck A, Harpal K, Eberhardt C, Declercq C, Pawling J, Moons L, Collen D, Risau W, Nagy A. (1996). Abnormal blood vessel development and lethality in embryos lacking a single VEGF allele. *Nature*. **380**, 435-9.

Chapman SC, Collignon J, Schoenwolf GC, Lumsden A. (2001). Improved method for chick whole-embryo culture using a filter paper carrier. *Dev Dyn*. **220**, 284-9.

Charbonneau NL, Ono RN, Corson GM, Keene DR, Sakai LY. (2004). Fine tuning of growth factor signals depends on fibrillin microfibril networks. *Birth Defects Res C Embryo Today.* **72**, 37-50.

Christ B, Grim M, Wilting J, von Kirschhofer K, Wachtler F. (1991). Differentiation of endothelial cells in avian embryos does not depend on gastrulation. *Acta Histochem.* **91**, 193-9.

Chuai M, Weijer CJ. (2009). Who moves whom during primitive streak formation in the chick embryo. *HFSP J*. **3**, 71-6.

Clauss M, Gerlach M, Gerlach H, Brett J, Wang F, Familletti PC, Pan YC, Olander JV, Connolly DT, Stern D. (1990). Vascular permeability factor: a tumor-derived polypeptide that induces endothelial cell and monocyte procoagulant activity, and promotes monocyte migration. *J Exp Med*. **172**, 1535-45.

Cohen-Gould L, Mikawa T. (1996). The fate diversity of mesodermal cells within the heart field during chicken early embryogenesis. *Dev Biol.* **177**, 265-73.

Collignon J, Schoenwolf GC, Lumsden A. (2001). Improved method for chick whole-embryo culture using a filter paper carrier. *Dev Dyn.* **220**, 284-9.

Compernolle V, Brusselmans K, Franco D, Moorman A, Dewerchin M, Collen D, Carmeliet P. (2003). Cardia bifida, defective heart development and abnormal neural crest migration in embryos lacking hypoxia-inducible factor-1alpha. *Cardiovasc Res*. **60**, 569-79.

Condorelli G, Roncarati R, Ross J Jr, Pisani A, Stassi G, Todaro M, Trocha S, Drusco A, Gu Y, Russo MA, Frati G, Jones SP, Lefer DJ, Napoli C, Croce

CM. (2001). Heart-targeted overexpression of caspase3 in mice increases infarct size and depresses cardiac function. *Proc Natl Acad Sci USA.* **98**, 9977-82.

Cripps RM, Olson EN. (2002). Control of cardiac development by an evolutionarily conserved transcriptional network. *Dev Biol*. **246**, 14-28.

Cui C, Cheuvront TJ, Lansford RD, Moreno-Rodriguez RA, Schultheiss TM, Rongish BJ. (2009). Dynamic positional fate map of the primary heart-forming region. *Dev Biol.* **332**, 212-22.

Cui C, Lansford R, Filla MB, Little CD, Cheuvront TJ, Rongish BJ. (2006). Electroporation and EGFP labeling of gastrulating quail embryos. *Dev Dyn.* **235**, 2802-10.

Cui C, Little CD, Rongish BJ. (2009). Rotation of organizer tissue contributes to left-right asymmetry. *Anat Rec (Hoboken).* **292**, 557-61.

Czirók A, Rongish BJ, Little CD. (2004). Extracellular matrix dynamics during vertebrate axis formation. *Dev Biol.* **268**, 111-22.

Czirók A, Rupp PA, Rongish BJ, Little CD. (2002). Multi-field 3D scanning light microscopy of early embryogenesis. *J Microsc.* **206**, 209-17.

Czirok A, Zamir EA, Filla MB, Little CD, Rongish BJ. (2006). Extracellular matrix macro-assembly dynamics in early vertebrate embryos. *Cur Topic Dev Biol.* **73**, 237-58.

Davies, CL. (1924). The cardiac jelly of the chick embryo. *Anat Rec.* **27**, 201-202.

de Boer BA, van den Berg G, Soufan AT, de Boer PA, Hagoort J, van den Hoff MJ, Moorman AF, Ruijter JM. (2012). Measurement and 3D-Visualization of Cell-

Cycle Length Using Double Labelling with Two Thymidine Analogues Applied in Early Heart Development. *PLoS One*. **7**, e47719.

de Jong F, Geerts WJ, Lamers WH, Los JA, Moorman AF. (1990). Isomyosin expression pattern during formation of the tubular chicken heart: a three-dimensional immunohistochemical analysis. *Anat Rec*. **226**, 213-27.

de Vries C, Escobedo JA, Ueno H, Houck K, Ferrara N, Williams LT. (1992). The fms-like tyrosine kinase, a receptor for vascular endothelial growth factor. *Science*. **255**, 989-91.

DeHaan RL. (1963). Migration patterns of the precardiac mesoderm in the early chick embrvo. *Exp Cell Res.* **29**, 544-60.

DeRuiter MC, Poelmann RE, Mentink MM, Vaniperen L, Gittenberger-De Groot AC. (1993) Early formation of the vascular system in quail embryos. *Anat Rec.* **235**(2):261-74.

Dibbens JA, Miller DL, Damert A, Risau W, Vadas MA, Goodall GJ. (1999). Hypoxic regulation of vascular endothelial growth factor mRNA stability requires the cooperation of multiple RNA elements. *Mol Biol Cell*. **10**, 907-19.

Doherty JT, Conlon FL, Mack CP, Taylor JM. (2010). Focal adhesion kinase is essential for cardiac looping and multichamber heart formation. *Genesis*. **48**, 492-504.

Dor Y, Camenisch TD, Itin A, Fishman GI, McDonald JA, Carmeliet P, Keshet E. (2001). A novel role for VEGF in endocardial cushion formation and its potential contribution to congenital heart defects. *Development*. **128**, 1531-8

Drake CJ, Davis LA, Walters L, Little CD. (1990). Avian vasculogenesis and the distribution of collagens I, IV, laminin, and fibronectin in the heart primordia. *J Exp Zool.* **255**(3):309-22.

Drake CJ, Little CD. (1995). Exogenous vascular endothelial growth factor induces malformed and hyperfused vessels during embryonic neovascularization. *Proc Natl Acad Sci U S A.* **92**(17):7657-61.

Drake CJ, Wessels A, Trusk T, Little CD. (2006). Elevated vascular endothelial cell growth factor affects mesocardial morphogenesis and inhibits normal heart bending. *Dev Dyn.* **235**(1):10-8.

Drocco JA, Grimm O, Tank DW, Wieschaus E. (2011). Measurement and perturbation of morphogen lifetime: effects on gradient shape. *Biophys J.* **101**(8):1807-1815.

Ehrman LA, Yutzey KE. (1999). Lack of regulation in the heart forming region of avian embryos. *Dev Biol.* **207**, 163-75.

Eisenberg CA, Bader D. (1995). QCE-6: a clonal cell line with cardiac myogenic and endothelial cell potentials. *Dev Biol.* **167**, 469-81.

Eisenberg LM, Markwald RR. (1995). Molecular regulation of atrioventricular valvuloseptal morphogenesis. *Circ Res.* **77**, 1-6.

Evans SM, Yelon D, Conlon FL, Kirby ML. (2010). Myocardial lineage development. *Circ Res*. **107**, 1428-44.

Ferrara N, Carver-Moore K, Chen H, Dowd M, Lu L, O'Shea KS, Powell-Braxton L, Hillan KJ, Moore MW. (1996). Heterozygous embryonic lethality induced by targeted inactivation of the VEGF gene. *Nature*. **380**, 439-42.

Ferrara N. (2000). Vascular endothelial growth factor and the regulation of angiogenesis. *Recent Prog Horm Res*. **55**, 15-35; discussion 35-6.

Ferrara N. (2001). Role of vascular endothelial growth factor in regulation of physiological angiogenesis. *Am J Physiol Cell Physiol*. **280**, C1358-66.

Ferrara N, Henzel WJ. (1989). Pituitary follicular cells secrete a novel heparin-binding growth factor specific for vascular endothelial cells. *Biochem Biophys Res Commun*. **161**, 851-8.

Feucht M, Christ B, Wilting J. (1997). VEGF induces cardiovascular malformation and embryonic lethality. *Am J Pathol.* **151**(5):1407-16.

Finkelstein EB, Poole TJ. (2003). Expression of vascular endothelial growth factor isoforms in the Japanese quail embryo. *Growth Factors*. **21**, 41-9.

Fish JE, Wythe JD, Xiao T, Bruneau BG, Stainier DY, Srivastava D, Woo S. (2011). A Slit/miR-218/Robo regulatory loop is required during heart tube formation in zebrafish. *Development.* **138(7)**:1409-19.

Fishman MC, Chien KR. (1997). Fashioning the vertebrate heart: earliest embryonic decisions. *Development.* **124**, 2099-117.

Flamme I, von Reutern M, Drexler HC, Syed-Ali S, Risau W. (1995). Overexpression of vascular endothelial growth factor in the avian embryo induces

hypervascularization and increased vascular permeability without alterations of embryonic pattern formation. *Dev Biol.* **171**(2):399-414.

Fleischer S, Dvir T. (2012). Tissue engineering on the nanoscale: lessons from the heart. *Curr Opin Biotechnol*. pii: S0958-1669 (12) 00171-1.

Fong GH, Zhang L, Bryce DM, Peng J. (1999). Increased hemangioblast commitment, not vascular disorganization, is the primary defect in flt-1 knock-out mice. *Development*. **126**, 3015-25.

Fontana L, Chen Y, Prijatelj P, Sakai T, Fassler R, Sakai LY, Rifkin DB. (2005) Fibronectin is required for integrin alphavbeta6-mediated activation of latent TGF-beta complexes containing LTBP-1. *FASEB J.* **19**, 1798-1808.

Forsythe JA, Jiang BH, Iyer NV, Agani F, Leung SW, Koos RD, Semenza GL. (1996). Activation of vascular endothelial growth factor gene transcription by hypoxia-inducible factor 1. *Mol Cell Biol*. **16**, 4604-13.

Gallagher BC, Sakai LY, Little CD. (1993). Fibrillin delineates the primary axis of the early avian embryo. *Dev Dyn.* **196**, 70-8.

Garavito-Aguilar ZV, Riley HE, Yelon D. (2010). Hand2 ensures an appropriate environment for cardiac fusion by limiting Fibronectin function. *Development*. **137**, 3215-20.

García-García MJ, Shibata M, Anderson KV. (2008). Chato, a KRAB zinc-finger protein, regulates convergent extension in the mouse embryo. *Development*. **135**, 3053-62.

Garcia-Martinez V, Schoenwolf GC. (1993). Primitive-streak origin of the cardiovascular system in avian embryos. *Dev Biol.* **159**, 706-19.

George EL, Baldwin HS, Hynes RO. (1997). Fibronectins are essential for heart and blood vessel morphogenesis but are dispensable for initial specification of precursor cells. *Blood*. **90**, 3073-81.

George EL, Georges-Labouesse EN, Patel-King RS, Rayburn H, Hynes RO. (1993). Defects in mesoderm, neural tube and vascular development in mouse embryos lacking fibronectin. *Development.* **119**, 1079-91.

Gessert S, Kühl M. (2010). The multiple phases and faces of wnt signaling during cardiac differentiation and development. *Circ Res*. **107**, 186-99.

Gerber HP, Hillan KJ, Ryan AM, Kowalski J, Keller GA, Rangell L, Wright BD, Radtke F, Aguet M, Ferrara N. (1999). VEGF is required for growth and survival in neonatal mice. *Development*. **126**, 1149-59.

Gingras D, Lamy S, Béliveau R. (2000). Tyrosine phosphorylation of the vascular endothelial-growth-factor receptor-2 (VEGFR-2) is modulated by Rho proteins. *Biochem J.* **348**, 273-80.

Glanzer ML, Peaslee MH. (1970). Inhibition of heart beat development by chloramphenicol in intact and Cardia bifida explanted chick embryos. *Experientia*. **26**, 370-1.

Gluzman-Poltorak Z, Cohen T, Shibuya M, Neufeld G. (2001). Vascular endothelial growth factor receptor-1 and neuropilin-2 form complexes. *J Biol Chem*. **276**, 18688–18694.

Goswami S, Qasba P, Ghatpande S, Carleton S, Deshpande AK, Baig M, Siddiqui MA. (1994). Differential expression of the myocyte enhancer factor 2 family of transcription factors in development: the cardiac factor BBF-1 is an early marker for cardiogenesis. *Mol Cell Biol*. **14**, 5130-8.

Gregg CL, Butcher JT. (2012). Quantitative in vivo imaging of embryonic development: opportunities and challenges. *Differentiation*. **84**, 149-62.

Gruber PJ, Epstein JA. (2004). Development gone awry: congenital heart disease. *Circ Res*. **94**, 273-83.

Grunstein J, Masbad JJ, Hickey R, Giordano F, Johnson RS. (2000). Isoforms of vascular endothelial growth factor act in a coordinate fashion To recruit and expand tumor vasculature. *Mol Cell Biol*. **20**, 7282-91.

Haddon CM, Lewis JH. (1991). Hyaluronan as a propellant for epithelial movement: the development of semicircular canals in the inner ear of Xenopus. *Development*. **112**, 541-50.

Haigh JJ. (2008). Role of VEGF in organogenesis. *Organogenesis*. **4**(4):247-56.

Hamburger V, Hamilton HL. (1951). A series of normal stages in the development of the chick embryo. *J Morphol.* **88**, 49-92.

Han Y, Dennis JE, Cohen-Gould L, Bader DM, Fischman DA. (1992). Expression of sarcomeric myosin in the presumptive myocardium of chicken embryos occurs within six hours of myocyte commitment. *Dev Dyn*. **193**, 257-65.

Hardin J, Keller R. (1988). The behaviour and function of bottle cells during gastrulation of Xenopus laevis. *Development*. **103**, 211-30.

Harding MJ, Nechiporuk AV. (2012). Fgfr-Ras-MAPK signaling is required for apical constriction via apical positioning of Rho-associated kinase during mechanosensory organ formation. *Development*. **139**, 3130-5.

Harris IS, Black BL. (2010). Development of the endocardium. *Pediatr Cardiol*. **31**(3):391-9.

Harrison GS, Maxwell F, Long CJ, Rosen CA, Glode LM, Maxwell IH. (1991). Activation of a diphtheria toxin A gene by expression of human immunodeficiency virus-1 Tat and Rev proteins in transfected cells. *Hum Gene Ther*. **2**, 53-60.

Hegedus B, Zách J, Czirók A, Lövey J, Vicsek T. (2004). Irradiation and Taxol treatment result in non-monotonous, dose-dependent changes in the motility of glioblastoma cells. *J Neurooncol.* **67**, 147-57.

Hegedus B, Czirók A, Fazekas I, B'abel T, Madar'asz E, Vicsek T. (2000). Locomotion and proliferation of glioblastoma cells in vitro: statistical evaluation of videomicroscopic observations*. J Neurosurg.* **92**, 428-34.

Hiratsuka S, Kataoka Y, Nakao K, Nakamura K, Morikawa S, Tanaka S, Katsuki M, Maru Y, Shibuya M. (2005). Vascular endothelial growth factor A (VEGF-A) is involved in guidance of VEGF receptor-positive cells to the anterior portion of early embryos. *Mol Cell Biol.* **25**, 355-63.

Hiratsuka S, Nakao K, Nakamura K, Katsuki M, Maru Y, Shibuya M. (2005). Membrane fixation of vascular endothelial growth factor receptor 1 ligand-binding domain is important for vasculogenesis and angiogenesis in mice. *Mol Cell Biol*. **25**, 346-54.

Hochgreb T, Linhares VL, Menezes DC, Sampaio AC, Yan CY, Cardoso WV, Rosenthal N, Xavier-Neto J. (2003). A caudorostral wave of RALDH2 conveys anteroposterior information to the cardiac field. *Development.* **130**, 5363-74.

Hoffman JI, Kaplan S. (2002). The incidence of congenital heart disease. *J Am Coll Cardiol*. **39**, 1890-900.

Holtzman NG, Schoenebeck JJ, Tsai HJ, Yelon D. (2007). Endocardium is necessary for cardiomyocyte movement during heart tube assembly. *Development.* **134**, 2379-86.

Hossain MJ, Whelan PF, Czirok A, Ghita O. (2011). An active particle-based tracking framework for 2D and 3D time-lapse microscopy images. *Proc. of IEEE EMBC*, in press.

Houck KA, Leung DW, Rowland AM, Winer J, Ferrara N. (1992). Dual regulation of vascular endothelial growth factor bioavailability by genetic and proteolytic mechanisms. *J Biol Chem*. **267**, 26031-7.

Huang CJ, Tu CT, Hsiao CD, Hsieh FJ, Tsai HJ. (2003). Germ-line transmission of a myocardium-specific GFP transgene reveals critical regulatory elements in the cardiac myosin light chain 2 promoter of zebrafish. *Dev Dyn*. **228**, 30-40.

Hubmacher D, Tiedemann K, Reinhardt DP. (2006). Fibrillins: from biogenesis of microfibrils to signaling functions. *Curr Top Dev Biol.* **75**, 93-123.

Hurle JM, Kitten GT, Sakai LY, Volpin D, Solursh M. (1994). Elastic extracellular matrix of the embryonic chick heart: an immunohistological study using laser confocal microscopy. *Dev Dyn.* **200**, 321-32.

Hynes RO. (2009). The extracellular matrix: not just pretty fibrils. *Science*. **326**, 1216-9.

Icardo JM, Manasek FJ. (1983). Fibronectin distribution during early chick embryo heart development. *Dev Biol.* **95**, 19-30.

Ishii Y, Langberg J, Rosborough K, Mikawa T. (2009). Endothelial cell lineages of the heart. *Cell Tissue Res.* **335**: 67-73.

Kaarbø M, Crane DI, Murrell WG. (2003). RhoA is highly up-regulated in the process of early heart development of the chick and important for normal embryogenesis. *Dev Dyn.* **227**, 35-47.

Kawahara A, Nishi T, Hisano Y, Fukui H, Yamaguchi A, Mochizuki N. (2009). The sphingolipid transporter spns2 functions in migration of zebrafish myocardial precursors. *Science*. **323**, 524-7.

Kazemi S, Wenzel D, Kolossov E, Lenka N, Raible A, Sasse P, Hescheler J, Addicks K, Fleischmann BK, Bloch W. (2002). Differential role of bFGF and VEGF for vasculogenesis. *Cell Physiol Biochem.* **12**, 55-62.

Keck PJ, Hauser SD, Krivi G, Sanzo K, Warren T, Feder J, Connolly DT. (1989). Vascular permeability factor, an endothelial cell mitogen related to PDGF. *Science*. **246**, 1309-12.

Kielty CM, Wess TJ, Haston L, Ashworth JL, Sherratt MJ, Shuttleworth CA. (2002). Fibrillin-rich microfibrils: elastic biopolymers of the extracellular matrix. J Muscle Res *Cell Motil.* **23**, 581-96.

Kikuchi Y, Agathon A, Alexander J, Thisse C, Waldron S, Yelon D, Thisse B, Stainier DY. (2001). casanova encodes a novel Sox-related protein necessary

and sufficient for early endoderm formation in zebrafish. *Genes Dev*. **15**, 1493-505.

Kirby ML. (2007). Cardiac Development. Oxford University Press, Oxford, UK.

Kitten GT, Markwald RR, Bolender DL. (1987). Distribution of basement membrane antigens in cryopreserved early embryonic hearts. *Anat Rec.* **217**(4):379-90.

Koch S, Claesson-Welsh L. (2012). Signal transduction by vascular endothelial growth factor receptors. *Cold Spring Harb Perspect Med*. **2**(7):a006502.

Kolega J. (2006). The role of myosin II motor activity in distributing myosin asymmetrically and coupling protrusive activity to cell translocation. *Mol Biol Cell.* **17**, 4435-45.

Kouvroukoglou S, Dee KC, Bizios R, McIntire LV, Zygourakis K. (2000). Endothelial cell migration on surfaces modified with immobilized adhesive peptides. *Biomaterials*. **21**(17):1725-33.

Krug EL, Runyan RB, Markwald RR. (1985). Protein extracts from early embryonic hearts initiate cardiac endothelial cytodifferentiation. *Dev Biol.* **112**(2):414-26.

Kuo CT, Morrisey EE, Anandappa R, Sigrist K, Lu MM, Parmacek MS, Soudais C, Leiden JM. (1997). GATA4 transcription factor is required for ventral morphogenesis and heart tube formation. *Genes Dev.* **11**:1048-1060.

Kupperman E, An S, Osborne N, Waldron S, Stainier DY. (2000). A sphingosine-1-phosphate receptor regulates cell migration during vertebrate heart development. *Nature.* **406**, 192-5.

Lagendijk AK, Goumans MJ, Burkhard SB, Bakkers J. (2011). MicroRNA-23 restricts cardiac valve formation by inhibiting Has2 and extracellular hyaluronic acid production. *Circ Res*. **109**, 649-57.

Lamalice L, Le Boeuf F, Huot J. (2007). Endothelial cell migration during angiogenesis. *Circ Res.* **100**, 782-94.

Lane MC, Koehl MA, Wilt F, Keller R. (1993). A role for regulated secretion of apical extracellular matrix during epithelial invagination in the sea urchin. *Development*. **117**, 1049-60.

Latacha KS, Rémond MC, Ramasubramanian A, Chen AY, Elson EL, Taber LA. (2005). Role of actin polymerization in bending of the early heart tube. *Dev Dyn*. **233**, 1272-86.

Lee JY, Marston DJ, Walston T, Hardin J, Halberstadt A, Goldstein B. (2006). Wnt/Frizzled signaling controls C. elegans gastrulation by activating actomyosin contractility. *Curr Biol*. **16**, 1986-97.

Leiss M, Beckmann K, Giros A, Costell M, Fassler R. (2008). The role of integrin binding sites in fibronectin matrix assembly in vivo. *Curr Opin Cell Biol*. **20**:502-507.

Leung DW, Cachianes G, Kuang WJ, Goeddel DV, Ferrara N. (1989). Vascular endothelial growth factor is a secreted angiogenic mitogen. *Science*. **246**, 1306-9.

Li S, Zhou D, Lu MM, Morrisey EE. (2004). Advanced cardiac morphogenesis does not require heart tube fusion. *Science*. **305**, 1619-22.

Little CD, Drake CJ. (2000). Whole-mount immunolabeling of embryos by microinjection. Increased detection levels of extracellular and cell surface epitopes. *Methods Mol Biol.* **135**, 183-9.

Lillie, Frank R. The Development of the Chick. 2nd ed. New York: Henry Holt and Co, 1930.

Linask KK. (2003). Regulation of heart morphology: current molecular and cellular perspectives on the coordinated emergence of cardiac form and function. *Birth Defects Res C Embryo Today.* **69**(1):14-24.

Linask KK, Lash JW. (1986). Precardiac cell migration: fibronectin localization at mesoderm-endoderm interface during directional movement. *Dev Biol.* **114**, 87-101.

Linask KK, Lash JW. (1988). A role for fibronectin in the migration of avian precardiac cells. I. Dose-dependent effects of fibronectin antibody. *Dev Biol.* **129**, 315-23.

Linask KK, Lash JW. (1988). A role for fibronectin in the migration of avian precardiac cells. II. Rotation of the heart-forming region during different stages and its effects. *Dev Biol.* **129**, 324-9.

Linask KK, Lash JW. (1993). Early heart development: dynamics of endocardial cell sorting suggests a common origin with cardiomyocytes. *Dev Dyn.* **196**, 62-9.

Little CD, Drake CJ. (2000). Whole-mount immunolabeling of embryos by microinjection. Increased detection levels of extracellular and cell surface epitopes. *Methods Mol Biol* **135**, 183-9.

Little CD, Piquet DM, Davis LA, Walters L, Drake CJ. (1989). Distribution of laminin, collagen type IV, collagen type I, and fibronectin in chicken cardiac jelly/basement membrane. *Anat Rec*. **224**, 417-25.

Little CD, Rongish BJ. (1995). The extracellular matrix during heart development. *Experientia* **51**, 873-82.

Loebel DA, Studdert JB, Power M, Radziewic T, Jones V, Coultas L, Jackson Y, Rao RS, Steiner K, Fossat N, Robb L, Tam PP. (2011). Rhou maintains the epithelial architecture and facilitates differentiation of the foregut endoderm. *Development*. **138**, 4511-22.

López-Sánchez C, García-Martínez V. (2011). Molecular determinants of cardiac specification. *Cardiovasc Res*. **91**, 185-95.

Lopez-Sanchez C, Garcia-Masa N, Gañan CM, Garcia-Martinez V. (2009). Movement and commitment of primitive streak precardiac cells during cardiogenesis. *Int J Dev Biol*. **53**, 1445-55.

Sugi Y, Lough J. (1995). Activin-A and FGF-2 mimic the inductive effects of anterior endoderm on terminal cardiac myogenesis in vitro. *Dev Biol*. **168**, 567-74.

Lough J, Sugi Y. (2000). Endoderm and heart development. *Dev Dyn.* **217**(4):327-42.

Maitra M, Schluterman MK, Nichols HA, Richardson JA, Lo CW, Srivastava D, Garg V. (2009). Interaction of Gata4 and Gata6 with Tbx5 is critical for normal cardiac development. *Dev Biol.* **326**, 368-77.

Manasek FJ. (1977). Structural glycoproteins of the embryonic cardiac extracellular matrix. *J Mol Cell Cardiol.* **9**, 425-39.

Manasek FJ, Burnside MB, Waterman RE. (1972). Myocardial cell shape change as a mechanism of embryonic heart looping. *Dev Biol*. **29**, 349-71.

Männer J. (2000). Cardiac looping in the chick embryo: a morphological review with special reference to terminological and biomechanical aspects of the looping process. *Anat Rec*. **259**, 248-62.

Manning A, McLachlan JC. (1990). Looping of chick embryo hearts in vitro. *J Anat.* **168**, 257-63.

Markwald RR, Fitzharris TP, Manasek FJ. (1977). Structural development of endocardial cushions. *Am J Anat.* **148**, 85-119.

Markwald RR, Fitzharris TP, Smith WN. (1975). Sturctural analysis of endocardial cytodifferentiation. *Dev Biol*. **42**, 160-80.

Martinsen BJ. (2005). Reference guide to the stages of chick heart embryology. *Dev Dyn.* **233**, 1217-37.

Matsui T, Raya A, Callol-Massot C, Kawakami Y, Oishi I, Rodriguez-Esteban C, Izpisúa Belmonte JC. (2007). miles-apart-Mediated regulation of cell-fibronectin interaction and myocardial migration in zebrafish. *Nat Clin Pract Cardiovasc Med.* **Suppl 1**, S77-82.

Mikawa T. (1999). Cardiac Lineages. In: Harvey RP, Rosenthal N, editors. Heart development. New York: Academic Press. p 19–33.

Mikawa T, Gourdie RG. (1996). Pericardial mesoderm generates a population of coronary smooth muscle cells migrating into the heart along with ingrowth of the epicardial organ. *Dev Biol*. **174**, 221-32.

Mikawa T, Poh AM, Kelly KA, Ishii Y, Reese DE. (2004). Induction and patterning of the primitive streak, an organizing center of gastrulation in the amniote. *Dev Dyn*. **229**, 422-32.

Milgrom-Hoffman M, Harrelson Z, Ferrara N, Zelzer E, Evans SM, Tzahor E. (2011). The heart endocardium is derived from vascular endothelial progenitors. *Development.* **138**(21):4777-4787.

Miquerol L, Langille BL, Nagy A. (2000). Embryonic development is disrupted by modest increases in vascular endothelial growth factor gene expression. *Development*. **127**, 3941-6.

Misfeldt AM, Boyle SC, Tompkins KL, Bautch VL, Labosky PA, Baldwin HS. (2009). Endocardial cells are a distinct endothelial lineage derived from Flk1+ multipotent cardiovascular progenitors. *Dev Biol.* **333**, 78-89.

Molkentin JD, Lin Q, Duncan SA, Olson EN. (1997). Requirement of the transcription factor GATA4 for heart tube formation and ventral morphogenesis. *Genes Dev.* **11**:1061-1072.

Nakamura A, Manasek FJ. (1978). Experimental studies of the shape and structure of isolated cardiac jelly. *J Embryol Exp Morphol.* **43**, 167-83.

Nakamura A, Manasek FJ. (1981). An experimental study of the relation of cardiac jelly to the shape of the early chick embryonic heart. *J Embryol Exp Morphol*. **65**, 235-56.

Narita N, Bielinska M, Wilson DB. (1997). Wild-type endoderm abrogates the ventral developmental defects associated with GATA-4 deficiency in the mouse. *Dev Biol.* **189**(2):270-4.

Nascone N, Mercola M. (1995). An inductive role for the endoderm in Xenopus cardiogenesis. *Development*. **121**, 515-23.

Nemer G, Nemer M. (2002). Cooperative interaction between GATA5 and NF-ATc regulates endothelial-endocardial differentiation of cardiogenic cells. *Development.* **129**, 4045-55.

Newman TJ. (2005). Modeling multicellular systems using subcellular elements. *Math Biosci Eng.* **2**, 613-24.

Ohta S, Mansour SL, Schoenwolf GC. (2010). BMP/SMAD signaling regulates the cell behaviors that drive the initial dorsal-specific regional morphogenesis of the otocyst. *Dev Biol*. **347**, 369-81.

Ohtani K, Dimmeler S. (2011). Epigenetic regulation of cardiovascular differentiation. *Cardiovasc Res*. **90**, 404-12.

Opitz JM, Clark EB. (2000). Heart development: an introduction. *Am J Med Genet.* **97**, 238-47.

Orkin RW, Toole BP. (1978). Hyaluronidase activity and hyaluronate content of the developing chick embryo heart. *Dev Biol*. **66**, 308-20.

Pages G, Pouyssegur J. (2005). Transcriptional regulation of the Vascular Endothelial Growth Factor gene—a concert of activating factors. *Cardiovasc Res*. **65**, 564-73.

Pardanaud L, Altmann C, Kitos P, Dieterlen-Lievre F, Buck CA. (1987). Vasculogenesis in the early quail blastodisc as studied with a monoclonal antibody recognizing endothelial cells. *Development.* **100**, 339-49.

Perryn ED Czirok A, Little CD: (2008). Vascular sprout formation entails tissue deformations and VE-cadherin-dependent cell-autonomous motility. *Dev Biol.* **313**:545-55.

Pihlajaniemi T, Kitten GT. (2006). Collagen XVIII/endostatin is associated with the epithelial-mesenchymal transformation in the atrioventricular valves during cardiac development. *Dev Dyn.* **235**, 132-42.

Puri MC, Partanen J, Rossant J, Bernstein A. (1999). Interaction of the TEK and TIE receptor tyrosine kinases during cardiovascular development. *Development*. **126**, 4569-80.

Qi JH, Claesson-Welsh L. (2001). VEGF-induced activation of phosphoinositide 3-kinase is dependent on focal adhesion kinase. *Exp Cell Res.* **263**, 173-82.

Rawles ME. (1943). The heart-forming areas of the early chick blastoderm. *Physiol Zool.* **16**, 49–92.

Redkar A, Montgomery M, Litvin J. (2001). Fate map of early avian cardiac progenitor cells. *Development*. **128**, 2269-79.

Reed RA, Womble MA, Dush MK, Tull RR, Bloom SK, Morckel AR, Devlin EW, Nascone-Yoder NM. (2009). Morphogenesis of the primitive gut tube is generated by Rho/ROCK/myosin II-mediated endoderm rearrangements. *Dev Dyn*. **12**, 3111-25.

Reiter JF, Alexander J, Rodaway A, Yelon D, Patient R, Holder N, Stainier DY. (1999). Gata5 is required for the development of the heart and endoderm in zebrafish. *Genes Dev.* **13**, 2983-95.

Risau W, Flamme I. (1995). Vasculogenesis. *Annu Rev Cell Dev Biol*. **11**, 73-91.

Roeder AH, Cunha A, Burl MC, Meyerowitz EM. (2012). A computational image analysis glossary for biologists. *Development*. **139**, 3071-80.

Rojas A, Schachterle W, Xu S-M, Martin F, Black BL. (2010). Direct transcriptional regulation of Gata4 during early endoderm specification is controlled by FoxA2 binding to an intronic enhancer. *Dev Biol.* **346**:356-355.

Rongish BJ, Drake CJ, Argraves WS, Little CD. (1998). Identification of the developmental marker, JB3-antigen, as fibrillin-2 and its de novo organization into embryonic microfibrous arrays. *Dev Dyn*. **212**, 461-71.

Rosenquist GC. (1970). Cardia bifida in chick embryos: anterior and posterior defects produced by transplanting tritiated thymidine-labeled grafts medial to the heart-forming regions. *Teratology.* **3**, 135-42.

Rosenquist GC. (1970). Location and movements of cardiogenic cells in the chick embryo: the heart-forming portion of the primitive streak. *Dev Biol.* **22**, 461-75.

Rosenquist GC, DeHaan RL. (1966). *Contr Embryol.* Vol. **38**, pp. 111-121.

Rosenthal J, Mangal V, Walker D, Bennett M, Mohun TJ, Lo CW. (2004). Rapid high resolution three dimensional reconstruction of embryos with episcopic fluorescence image capture. *Birth Defects Res C Embryo Today.* **72**, 213-23.

Rossant J, Nagy A. (1999). In search of the tabula rasa of human cells. *Nat Biotechnol*. **17**, 23-4.

Rupp PA, Czirók A, Little CD. (2004). alphavbeta3 integrin-dependent endothelial cell dynamics in vivo. *Development.* **131**, 2887-97.

Rupp PA, Kulesa PM. (2007). A role for RhoA in the two-phase migratory pattern of post-otic neural crest cells. *Dev Biol*. **311**, 159-71.

Rupp PA, Rongish BJ, Czirok A, Little CD. (2003). Culturing of avian embryos for time-lapse imaging. *Biotechniques*. **34**, 274-8.

Ruhrberg C. (2003). Growing and shaping the vascular tree: multiple roles for VEGF. *Bioessays*. **25**, 1052-60.

Sabin FR. (1920). Studies on the origin of blood-vessels and of red corpuscles as seen in the living blastoderm of chicks during the second day of incubation. *Contr Embryol.* **9**, 215-262.

Sakaguchi T, Kikuchi Y, Kuroiwa A, Takeda H, Stainier DY. (2006). The yolk syncytial layer regulates myocardial migration by influencing extracellular matrix assembly in zebrafish. *Development*. **133**, 4063-72.

Saito M, Iwawaki T, Taya C, Yonekawa H, Noda M, Inui Y, Mekada E, Kimata Y, Tsuru A, Kohno K. (2001). Diphtheria toxin receptor-mediated conditional and targeted cell ablation in transgenic mice. *Nat Biotechnol*. **19**, 746-50.

Sakabe M, Ikeda K, Nakatani K, Kawada N, Imanaka-Yoshida K, Yoshida T, Yamagishi T, Nakajima Y. (2006). Rho kinases regulate endothelial invasion

and migration during valvuloseptal endocardial cushion tissue formation. *Dev Dyn.* **235**, 94-104.

Sakai LY, Keene DR, Engvall E. (1986). Fibrillin, a new 350-kD glycoprotein, is a component of extracellular microfibrils. *J Cell Biol.* **103**, 2499-509.

Salic A, Mitchison TJ. (2008). A chemical method for fast and sensitive detection of DNA synthesis in vivo. *Proc Natl Acad Sci USA.* **105**, 2415–2420.

Sanders EJ, Varedi M, French AS. (1993). Cell proliferation in the gastrulating chick embryo: a study using BrdU incorporation and PCNA localization. *Development.* **118**, 389-99.

Satin J, Fujii S, DeHaan RL. (1988). Development of cardiac beat rate in early chick embryos is regulated by regional cues. *Dev Biol*. **129**, 103-13.

Sato Y, Poynter G, Huss D, Filla MB, Czirok A, Rongish BJ, Little CD, Fraser SE, Lansford R. (2010) Dynamic Analysis of Vascular Morphogenesis Using Transgenic Quail Embryos. *PLoS One*, **5**:e12674*,* 2010.

Sawyer JM, Harrell JR, Shemer G, Sullivan-Brown J, Roh-Johnson M, Goldstein B. (2010). Apical constriction: a cell shape change that can drive morphogenesis. *Dev Biol*. **341**, 5-19.

Schier AF, Neuhauss SC, Helde KA, Talbot WS, Driever W. (1997). The one-eyed pinhead gene functions in mesoderm and endoderm formation in zebrafish and interacts with no tail. *Development*. **124**, :327-42.

Schmidt A, Brixius K, Bloch W. (2007). Endothelial precursor cell migration during vasculogenesis. *Circ Res.* **101**, 125-36.

Schoenebeck JJ, Keegan BR, Yelon D (2007). Vessel and blood specification override cardiac potential in anterior mesoderm. *Dev Cell*, **13**(2):254-67.

Schultheiss TM, Xydas S, Lassar AB. (1995). Induction of avian cardiac myogenesis by anterior endoderm. *Development*. **121**, 4203-14.

Senger DR, Ledbetter SR, Claffey KP, Papadopoulos-Sergiou A, Peruzzi CA, Detmar M. (1996). Stimulation of endothelial cell migration by vascular permeability factor/vascular endothelial growth factor through cooperative mechanisms involving the alphavbeta3 integrin, osteopontin, and thrombin. *Am J Pathol*. **149**, 293-305.

Sepich DS, Solnica-Krezel L. (2005). Analysis of cell movements in zebrafish embryos: morphometrics and measuring movement of labeled cell populations in vivo. *Methods Mol Biol*. **294**, 211-33.

Shalaby F, Rossant J, Yamaguchi TP, Gertsenstein M, Wu XF, Breitman ML, Schuh AC. (1995). Failure of blood-island formation and vasculogenesis in Flk-1-deficient mice. *Nature*. **376**, 62-6.

Sissman NJ. (1966). Cell multiplication rates during development of the primitive cardiac tube in the chick embryo. *Nature*. **210**, 504-7.

Sondell M, Lundborg G, Kanje M. (1999). Vascular endothelial growth factor has neurotrophic activity and stimulates axonal outgrowth, enhancing cell survival and Schwann cell proliferation in the peripheral nervous system. *J Neurosci*. **19**, 5731-40.

Spence SG, Argraves WS, Walters L, Hungerford JE, Little CD. (1992). Fibulin is localized at sites of epithelial-mesenchymal transitions in the early avian embryo. *Dev Biol*. **151**, 473-84.

Spence, JR, Lauf, R Shroyer, NF: (2011). Vertebrate intestinal endoderm development. *Dev Dyn.* **240**:501-520.

Stainier DY, Weinstein BM, Detrich HW 3rd, Zon LI, Fishman MC. (1995). Cloche, an early acting zebrafish gene, is required by both the endothelial and hematopoietic lineages. *Development.* **121**, 3141-50.

Stalmans I, Lambrechts D, De Smet F, Jansen S, Wang J, Maity S, Kneer P, von der Ohe M, Swillen A, Maes C, Gewillig M et al. (2003). VEGF: a modifier of the del22q11 (DiGeorge) syndrome? *Nat Med*. **9**, 173-82.

Stalsberg H. (1969). Regional mitotic activity in the precardiac mesoderm and differentiating heart tube in the chick embryo. *Dev Biol.* **20**, 18-45.

Stalsberg H, DeHaan RL. (1968). Endodermal movements during foregut formation in the chick embryo. *Dev Biol.* **18**(2):198-215.

Stalsberg H, DeHaan RL. (1969). The precardiac areas and formation of the tubular heart in the chick embryo. *Dev Biol.* **19**,128-59.

Stenzel D, Lundkvist A, Sauvaget D, Busse M, Graupera M, van der Flier A, Wijelath ES, Murray J, Sobel M, Costell M, Takahashi S, Fassler R, Yamaguchi Y, Gutmann DH, Hynes RO, Gerhardt H. (2011). Integrin-dependent and –independent functions of astrocytic fibronectin in retinal angiogenesis. *Development* **138**:4451-4463.

Streit A, Stern CD. (1999). Establishment and maintenance of the border of the neural plate in the chick: involvement of FGF and BMP activity. *Mech Dev.* **82**, 51-66.

Su H, Lu R, Chang JC, Kan YW. (1997). Tissue-specific expression of herpes simplex virus thymidine kinase gene delivered by adeno-associated virus inhibits the growth of human hepatocellular carcinoma in athymic mice. *Proc Natl Acad Sci USA*. **94**, 13891-6.

Sugi Y, Markwald RR. (1996). Formation and early morphogenesis of endocardial endothelial precursor cells and the role of endoderm. *Dev Biol.* **175**, 66-83.

Sugi Y, Markwald RR. (2003). Endodermal growth factors promote endocardial precursor cell formation from precardiac mesoderm. *Dev Biol.* **263**, 35-49.

Sugishita Y, Takahashi T, Shimizu T, Yao A, Kinugawa K, Sugishita K, Harada K, Matsui H, Nagai R. (2000). Expression of genes encoding vascular endothelial growth factor and its Flk-1 receptor in the chick embryonic heart. *J Mol Cell Cardiol.* **32**(6):1039-51.

Suzuki HR, Solursh M, Baldwin HS. (1995). Relationship between fibronectin expression during gastrulation and heart formation in the rat embryo. *Dev Dyn.* **204**(3):259-77.

Szabo A, Rupp PA, Rongish BJ, Little CD, Czirok A. (2011) Extracellular matrix fluctuations during early embryogenesis. Invited MS submitted to *Phys. Biol.*

Szabó A, Unnep R, Méhes E, Twal WO, Argraves WS, Cao Y, Czirók A. (2010). Collective cell motion in endothelial monolayers. *Phys Biol*. **7**(4):046007.

Taber LA. (2006). Biophysical mechanisms of cardiac looping. *Int J Dev Biol*. **50**, 323-32.

Taber LA, Voronov DA, Ramasubramanian A. (2010). The role of mechanical forces in the torsional component of cardiac looping. *Ann N Y Acad Sci.* **1188**, 103-10.

Takashima S, Kitakaze M, Asakura M, Asanuma H, Sanada S, Tashiro F, Niwa H, Miyazaki Ji J, Hirota S, Kitamura Y, Kitsukawa T, Fujisawa H, Klagsbrun M, Hori M. (2002). Targeting of both mouse neuropilin-1 and neuropilin-2 genes severely impairs developmental yolk sac and embryonic angiogenesis. *Proc Natl Acad Sci USA*. **99**, 3657-62.

Terman BI, Dougher-Vermazen M, Carrion ME, Dimitrov D, Armellino DC, Gospodarowicz D, Böhlen P. (1992). Identification of the KDR tyrosine kinase as a receptor for vascular endothelial cell growth factor. *Biochem Biophys Res Commun*. **187**, 1579-86.

Tischer E, Mitchell R, Hartman T, Silva M, Gospodarowicz D, Fiddes JC, Abraham JA. (1991). The human gene for vascular endothelial growth factor. Multiple protein forms are encoded through alternative exon splicing. *J Biol Chem*. **266**, 11947-54.

Trinh LA, Stainier DY. (2004). Fibronectin regulates epithelial organization during myocardial migration in zebrafish. *Dev Cell.* **6**, 371-82.

Twal WO, Czirok A, Hegedus B, Knaak C, Chintalapudi MR, Okagawa H, Sugi Y, van den Berg G, Abu-Issa R, de Boer BA, Hutson MR, de Boer PA, Soufan AT, Ruijter JM, Kirby ML, van den Hoff MJ, Moorman AF. (2009). A caudal

proliferating growth center contributes to both poles of the forming heart tube. *Circ Res.* **104**, 179-88.

van Weerd JH, Koshiba-Takeuchi K, Kwon C, Takeuchi JK. (2011). Epigenetic factors and cardiac development. *Cardiovasc Res*. **91**, 203-11.

van Wijk B, Moorman AF, van den Hoff MJ. (2007). Role of bone morphogenetic proteins in cardiac differentiation. *Cardiovasc Res*. **74**, 244-55.

Varner VD, Taber LA. (2012). Not just inductive: a crucial mechanical role for the endoderm during heart tube assembly. *Development*. **139**(9):1680-90.

Varner VD, Voronov DA, Taber LA. (2010). Mechanics of head fold formation: investigating tissue-level forces during early development. *Development.* **137**(22):3801-11. Epub 2010 Oct 7.

Vile RG, Hart IR. (1993). Use of tissue-specific expression of the herpes simplex virus thymidine kinase gene to inhibit growth of established murine melanomas following direct intratumoral injection of DNA. *Cancer Res*. **53**, 3860-4.

von Kirschhofer K, Grim M, Christ B, Wachtler F. (1994). Emergence of myogenic and endothelial cell lineages in avian embryos. *Dev Biol.* **163**, 270-8.

Voronov DA, Alford PW, Xu G, Taber LA. (2004). The role of mechanical forces in dextral rotation during cardiac looping in the chick embryo. *Dev Biol*. **272**, 339-50.

Wagner M, Siddiqui MA. (2007). Signal transduction in early heart development (I): cardiogenic induction and heart tube formation. *Exp Biol Med (Maywood).* **232**, 852-65.

Wallace KN, Pack M. (2003). Unique and conserved aspects of gut development in zebrafish. *Dev Biol.* **255**, 12-29.

Warkman AS, Yatskievych TA, Hardy KM, Krieg PA, Antin PB. (2008). Myocardin expression during avian embryonic heart development requires the endoderm but is independent of BMP signaling. *Dev Dyn*. **237**, 216-21.

Warren M, Puskarczyk K, Chapman SC. (2009). Chick embryo proliferation studies using EdU labeling. *Dev Dyn.* **238**, 944-9.

Wei Y, Mikawa T. (2000). Fate diversity of primitive streak cells during heart field formation in ovo. *Dev Dyn*. **219**, 505-13.

Wei L, Wang L, Carson JA, Agan JE, Imanaka-Yoshida K, Schwartz RJ. (2001). beta1 integrin and organized actin filaments facilitate cardiomyocyte-specific RhoA-dependent activation of the skeletal alpha-actin promoter. *FASEB J*. **15**, 785-96.

Wiens DJ. (1996). An alternative model for cell sheet migration on fibronectin during heart formation. *J Theor Biol.* **179**, 33-9.

Wijelath ES, Murray J, Rahman S, Patel Y, Ishida A, Strand K, Aziz S, Cardona C, Hammond WP, Savidge GF, Rafii S, Sobel M. (2002). Novel vascular endothelial growth factor binding domains of fibronectin enhance vascular endothelial growth factor biological activity. *Circ Res* **91**, 25-31.

Wunsch AM, Little CD, Markwald RR. (1994). Cardiac endothelial heterogeneity defines valvular development as demonstrated by the diverse expression of JB3, an antigen of the endocardial cushion tissue. *Dev Biol.* **165**, 585-601.

Xie K, Wei D, Shi Q, Huang S. (2004). Constitutive and inducible expression and regulation of vascular endothelial growth factor. *Cytokine Growth Factor Rev*. **15**, 297-324.

Yu SR, Burkhardt M, Nowak M, Ries J, Petrasek Z, Scholpp S, Schwille P, Brand M. (2009). Fgf8 morphogen gradient forms by a source-sink mechanism with freely diffusing molecules. *Nature.* **461**: 533-536.

Yue X, Tomanek RJ. (2001). Effects of VEGF(165) and VEGF(121) on vasculogenesis and angiogenesis in cultured embryonic quail hearts. *Am J Physiol Heart Circ Physiol*. **280**, H2240-7.

Yue Q, Wagstaff L, Yang X, Weijer C, Münsterberg A. (2008). Wnt3a-mediated chemorepulsion controls movement patterns of cardiac progenitors and requires RhoA function. *Development*. **135**, 1029-37.

Yutzey KE, Kirby ML. (2002). Wherefore heart thou? Embryonic origins of cardiogenic mesoderm. *Dev Dyn.* **223**, 307-20.

Zamir EA, Czirók A, Cui C, Little CD, Rongish BJ. (2006). Mesodermal cell displacements during avian gastrulation are due to both individual cell-autonomous and convective tissue movements. *Proc Natl Acad Sci U S A.* **103**, 19806-11.

Zamir EA, Czirók A, Rongish BJ, Little CD. (2005). A digital image-based method for computational tissue fate mapping during early avian morphogenesis. *Ann Biomed Eng* **33**, 854-65.

Zamir EA, Rongish BJ, Little CD. (2008). The ECM moves during primitive streak formation—computation of ECM versus cellular motion. *PLoS Biol* **6**, e247.

Zhao Z, Rivkees SA. (2004). Rho-associated kinases play a role in endocardial cell differentiation and migration. *Dev Biol.* **275**, 183-91.

Zoeller JJ, Whitelock JM, Iozzo RV. (2009). Perlecan regulates developmental angiogenesis by modulating the VEGF-VEGFR2 axis. *Matrix Biol.* **28**, 284-91.